

# The Applications of Metamaterials

Guest Editors: Hui Feng Ma, Sanming Hu, Yun Gui Ma, Yun Lai,  
and Karu Esselle





---

# **The Applications of Metamaterials**

International Journal of Antennas and Propagation

---

## **The Applications of Metamaterials**

Guest Editors: Hui Feng Ma, Sanming Hu, Yun Gui Ma,  
Yun Lai, and Karu Esselle



---

Copyright © 2015 Hindawi Publishing Corporation. All rights reserved.

This is a special issue published in “International Journal of Antennas and Propagation.” All articles are open access articles distributed under the Creative Commons Attribution License, which permits unrestricted use, distribution, and reproduction in any medium, provided the original work is properly cited.

## Editorial Board

Ana Alejos, Spain  
Mohammad Ali, USA  
Jaume Anguera, Spain  
Ercument Arvas, USA  
Alexei Ashikhmin, USA  
Herve Aubert, France  
Paolo Baccarelli, Italy  
Xiulong Bao, Ireland  
Toni Björninen, Finland  
Djuradj S. Budimir, UK  
Paolo Burghignoli, Italy  
Shah N. Burokur, France  
Giuseppe Castaldi, Italy  
Felipe Cátedra, Spain  
Chih-Hua Chang, Taiwan  
Deb Chatterjee, USA  
Shih Yuan Chen, Taiwan  
Yu Jian Cheng, China  
Renato Cicchetti, Italy  
Lorenzo Crocco, Italy  
Claudio Curcio, Italy  
Francesco D'Agostino, Italy  
Maria E. De Cos, Spain  
Tayeb A. Denidni, Canada  
Giuseppe Di Massa, Italy  
Michele D'Urso, Italy  
Francisco Falcone, Spain  
Quanyuan Feng, China  
Miguel Ferrando Bataller, Spain  
Flaminio Ferrara, Italy  
Vincenzo Galdi, Italy

Feifei Gao, China  
Junping Geng, China  
Claudio Gennarelli, Italy  
Rocco Guerriero, Italy  
Kerim Guney, Turkey  
Song Guo, Japan  
Qian He, China  
Mohamed Himdi, France  
Heng-Tung Hsu, Taiwan  
Jun Hu, China  
Tamer S. Ibrahim, USA  
Mohammad T. Islam, Malaysia  
Weixiang Jiang, China  
M. R. Kamarudin, Malaysia  
Kyeong Jin Kim, USA  
Ahmed A. Kishk, Canada  
Slawomir Koziel, Iceland  
Luis Landesa, Spain  
Ding-Bing Lin, Taiwan  
Angelo Liseno, Italy  
Giampiero Lovat, Italy  
Lorenzo Luini, Italy  
Atsushi Mase, Japan  
Diego Masotti, Italy  
Giuseppe Mazzeola, Italy  
C. F. Mecklenbräuker, Austria  
Massimo Migliozi, Italy  
Mark Mirotznik, USA  
Ahmed T. Mobashsher, Australia  
Ananda S. Mohan, Australia  
Jose-Maria Molina-Garcia-Pardo, Spain

Marco Mussetta, Italy  
N. Nasimuddin, Singapore  
Miguel Navarro-Cia, UK  
Mourad Nedil, Canada  
Symeon Nikolaou, Cyprus  
Giacomo Oliveri, Italy  
Athanasios D. Panagopoulos, Greece  
Ikmo Park, Korea  
Matteo Pastorino, Italy  
Mugen Peng, China  
Massimiliano Pieraccini, Italy  
Xianming Qing, Singapore  
Ahmad Safaai-Jazi, USA  
Safieddin Safavi-Naeini, Canada  
Magdalena Salazar-Palma, Spain  
Stefano Selleri, Italy  
John J. Shynk, USA  
Prabhakar Singh, India  
Raffaele Solimene, Italy  
Seong-Youp Suh, USA  
Sheng Sun, Hong Kong  
Larbi Talbi, Canada  
Luciano Tarricone, Italy  
Parveen Wahid, USA  
Yuanxun Ethan Wang, USA  
Wen-Qin Wang, China  
Shiwen Yang, China  
Yuan Yao, China  
Jingjing Zhang, Denmark

# Contents

**The Applications of Metamaterials**, Hui Feng Ma, Sanming Hu, Yun Gui Ma, Yun Lai, and Karu Esselle  
Volume 2015, Article ID 729617, 2 pages

**Comparison Analysis of Single Loop Resonator Based Miniaturized Triple-Band Planar Monopole Antennas**, Kaimin Wu, Yongjun Huang, Ruiming Wen, Jian Li, and Guangjun Wen  
Volume 2015, Article ID 495353, 10 pages

**Metamaterial Inspired Microstrip Antenna Investigations Using Metascreens**,  
Muhammad Tauseef Asim and Mushtaq Ahmed  
Volume 2015, Article ID 236136, 9 pages

**Control of the Radiation Patterns Using Homogeneous and Isotropic Impedance Metasurface**, Fan Yang, Zhong Lei Mei, and Tie Jun Cui  
Volume 2015, Article ID 917829, 7 pages

**Suppression of Specular Reflections by Metasurface with Engineered Nonuniform Distribution of Reflection Phase**, Xin Mi Yang, Ge Lan Jiang, Xue Guan Liu, and Cheng Xiang Weng  
Volume 2015, Article ID 560403, 8 pages

**Design of a Compact and High Sensitivity Temperature Sensor Using Metamaterial**, Sabah Zemouli, Abdelhafid Chaabi, and Houcine Sofiane Talbi  
Volume 2015, Article ID 301358, 7 pages

**Modified Luneburg Lens Based on Metamaterials**, Haibing Chen, Qiang Cheng, Aihua Huang, Junyan Dai, Huiying Lu, Jie Zhao, Huifeng Ma, Weixiang Jiang, and Tiejun Cui  
Volume 2015, Article ID 902634, 6 pages

**Compact Two-Section Half-Wave Balun Based on Planar Artificial Transmission Lines**, Changjun Liu, Zhenyu Yin, Yilan Yang, and Wen Huang  
Volume 2015, Article ID 256536, 6 pages

## Editorial

# The Applications of Metamaterials

**Hui Feng Ma,<sup>1</sup> Sanming Hu,<sup>2,3</sup> Yun Gui Ma,<sup>4</sup> Yun Lai,<sup>5</sup> and Karu Esselle<sup>6</sup>**

<sup>1</sup>State Key Laboratory of Millimeter Waves, Southeast University, Nanjing 210096, China

<sup>2</sup>School of Engineering and Physical Sciences, Heriot-Watt University, Edinburgh EH14 4AS, UK

<sup>3</sup>Institute of Microwave Techniques, University of Ulm, 89069 Ulm, Germany

<sup>4</sup>State Key Lab of Modern Optical Instrumentation, Centre for Optical and Electromagnetic Research, Department of Optical Engineering, Zhejiang University, Hangzhou 310058, China

<sup>5</sup>School of Physical Science and Technology, Soochow University, Suzhou 215006, China

<sup>6</sup>Department of Engineering, Macquarie University, Sydney, NSW 2109, Australia

Correspondence should be addressed to Hui Feng Ma; [hfma@seu.edu.cn](mailto:hfma@seu.edu.cn)

Received 2 April 2015; Accepted 2 April 2015

Copyright © 2015 Hui Feng Ma et al. This is an open access article distributed under the Creative Commons Attribution License, which permits unrestricted use, distribution, and reproduction in any medium, provided the original work is properly cited.

Metamaterials are artificial structures composed of periodic or nonperiodic subwavelength macro cells. The advantages of metamaterials are that their effective medium properties can be controlled by designing the macro units to constitute special materials that do not exist in nature. Metamaterial is a research area with importantly theoretical significance and challenges, which has achieved significant breakthroughs in theory. However, the lack of applications is a bottleneck to restrict the further development of metamaterial. Hence it is very important to develop and seek the significant applications in this area. The papers selected for this special issue present some potential applications of metamaterial, and we are pleased to share them with the readers.

The special issue contains seven papers, where two papers are related to control of radiation patterns by using metasurface. One paper presents a modified two-dimensional Luneburg lens based on bulky metamaterials. One paper introduces an improved artificial transmission line with low characteristic impedance to minimize the Balun. One paper provides a method to design the temperature sensor by using metamaterial. The other two papers propose the combination of the metamaterial structures with traditional microstrip antennas to achieve performance improvement.

In a paper entitled “Suppression of Specular Reflections by Metasurface with Engineered Nonuniform Distribution of Reflection Phase,” X. M. Yang et al. study a novel

planar metasurface characterizing nonuniform distribution of reflection phase. A design example of the metasurface is presented. In the example, three-layer stacked square patches with variable sizes are utilized as the reflecting elements of the metasurface. It is verified by both theoretical calculation and numerical simulation that the metasurface is capable of suppressing specular reflections of conducting plates significantly for two orthogonal incident polarizations by scattering most incident energy in off-specular directions. The proposed metasurface is an effective approach of RCS-reduction for conducting objects and has the potential of providing broadband performance.

In the paper entitled “Control of the Radiation Patterns Using Homogeneous and Isotropic Impedance Metasurface,” F. Yang et al. use a cylindrical metasurface to conduct an antenna system. They point out that the radiation patterns of this antenna can be manipulated by altering the surface impedance of this metasurface. Also, they give theoretical derivations, together with some numerical simulation, to demonstrate the validity of this antenna system. The proposed surface has many good properties, like isotropy, homogeneity, low profile, and high selectivity of frequency.

In the paper entitled “Modified Luneburg Lens Based on Metamaterials,” H. Chen et al. present a modified two-dimensional Luneburg lens composed of a number of concentric layers, and the varied I-shaped units are used in the

design. Both simulation and experiment results prove the fact that cylindrical waves can be transformed into plane waves when penetrating through the modified Luneburg lens.

In the paper entitled "Compact Two-Section Half-Wave Balun Based on Planar Artificial Transmission Lines," C. Liu et al. present and analyse an improved artificial transmission line with low characteristic impedance. Then, using seven sections of this transmission line, a compact 900 MHz Balun is designed, fabricated, and experimentally verified to achieve a significant size reduction of around 90%.

In a paper entitled "Design of a Compact and High Sensitivity Temperature Sensor Using Metamaterial," S. Zemouli et al. present a sensor of temperature using the metamaterial which is composed of split resonant rings (SRRs) and a cut wire deposited on the surface of BaTiO<sub>3</sub> substrate. The permittivity of BaTiO<sub>3</sub> has big dependence with the temperature, which can affect the resonant frequency of the SRRs and cut wire; hence the resonant peak of the structures will be sensitive to the temperature.

In the paper entitled "Metamaterial Inspired Microstrip Antenna Investigations Using Metascreens," M. T. Asim and M. Ahmed introduce a metascreen and apply it under the proposed metamaterial antenna and over a simple patch antenna to investigate their performances. The -10 dB bandwidths are 14.56% and 22.86% for the metamaterial antenna with single and double metascreens which are observed from measured results, respectively. Similarly, the -10 dB bandwidth for the simple patch with inverted metascreen is also measured as 9.6% and 16.66% for dual band operation. Hence, the proposed technique has potential applications in UWB wireless.

In a paper entitled "Comparison Analysis of Single Loop Resonator Based Miniaturized Triple-Band Planar Monopole Antennas," K. Wu et al. present four kinds of metamaterial miniaturized triple-band antennas by integrating a single loop resonator (SLR) as part of the radiation patch. Two kinds of SLRs (rectangular and circular shaped radiation patches) are investigated and discussed, which can provide the additional operating frequencies of miniaturized planar monopole antennas. Two feeding techniques including coplanar waveguide and microstrip feeds are also presented, respectively. The numerical and experimental results show good performances of the miniaturized triple-band antennas consisting of a SLR, which have potential applications for wireless communications.

## Acknowledgments

We would like to thank the authors for their excellent contributions and patience in assisting us. Finally, the fundamental work of all the reviewers of these papers is also very warmly acknowledged.

*Hui Feng Ma  
Sanming Hu  
Yun Gui Ma  
Yun Lai  
Karu Esselle*

## Research Article

# Comparison Analysis of Single Loop Resonator Based Miniaturized Triple-Band Planar Monopole Antennas

**Kaimin Wu, Yongjun Huang, Ruiming Wen, Jian Li, and Guangjun Wen**

*Centre for RFIC and System Technology, School of Communication and Information Engineering,  
University of Electronic Science and Technology of China, Chengdu 611731, China*

Correspondence should be addressed to Yongjun Huang; [yongjunh@uestc.edu.cn](mailto:yongjunh@uestc.edu.cn)

Received 16 September 2014; Revised 21 December 2014; Accepted 24 December 2014

Academic Editor: Sanming Hu

Copyright © 2015 Kaimin Wu et al. This is an open access article distributed under the Creative Commons Attribution License, which permits unrestricted use, distribution, and reproduction in any medium, provided the original work is properly cited.

We systemically analyze and discuss a group of miniaturized triple-band planar monopole antennas by integrating with a single loop resonator (SLR) as part of the radiation patch. Two configurations (rectangular and circular shaped radiation patches) are presented and the corresponding SLRs are integrated in the patches to contribute additional operating frequencies. Two feed techniques (coplanar waveguide and microstrip feeds) are performed to couple the electromagnetic waves. The conventional planar monopole antennas without the SLRs are also analyzed comparatively. Numerical and experimental methods are performed to demonstrate and discuss the proposed designs.

## 1. Introduction

In recent years, due to the breakthroughs of modern wireless communications, for example, near field communications (NFC), radio frequency identifications (RFID), and the internet of things (IoT), the developments of miniaturized and multiband/multimode communication components have been the main barriers in such science and engineering areas. The first component, for instance, used to send/receive the electromagnetic wave signals should be the antenna component, and comprehensive researches have focused on the multiband antennas and/or ultrawideband antennas, for the miniaturization and multiband/multimode requirements. In the various kinds of reported multiband antennas, monopole antenna is one of the most attractive configurations in recent years, because of the compact sizes, flexible designs, low fabrication costs, and well radiation characteristics. Some of the monopole antenna configurations are, for example, circular/rectangular/spiral ring patch antenna [1–3], I-shaped/U-shaped slot defected [4] and T-shaped slot defected planar antenna [5], and spirograph planar antenna [6]. These multiband monopole antennas were achieved by properly designing various resonator configurations to reduce operating frequencies, improve radiation pattern, and at the same time

reduce cross-polarization characteristics. However, most of these antennas have complex configurations.

On the other hand, since the realization of the first metamaterial in 2000 [7], it has been proposed that the bulk metamaterials or metamaterial units can be widely used for designing novel antennas to improve most of the characteristics comparing with conventional antennas [8]. For the monopole antenna integrated with metamaterial unit, some novel configurations have been reported elsewhere, for example, the band-notched ultra-wideband (UWB) planar antennas with a modified complementary split-ring resonator [9] and the single metamaterial unit inspired dual-band/multiband monopole antennas [10–12]. Taking into deep consideration the previously mentioned metamaterial-inspired dual/multiband antennas, two or three different resonators were integrated as the radiation part to achieve dual/multiband properties. In this paper, we propose and systematically analyze a group of miniaturized triple-band planar monopole antennas by integrating with a single loop resonator (SLR) as part of the radiation patch. Specifically, two configurations with rectangular and circular shaped radiation patches are presented and the corresponding SLRs are integrated in the patches to contribute additional operation frequencies. Two feed techniques (coplanar waveguide and

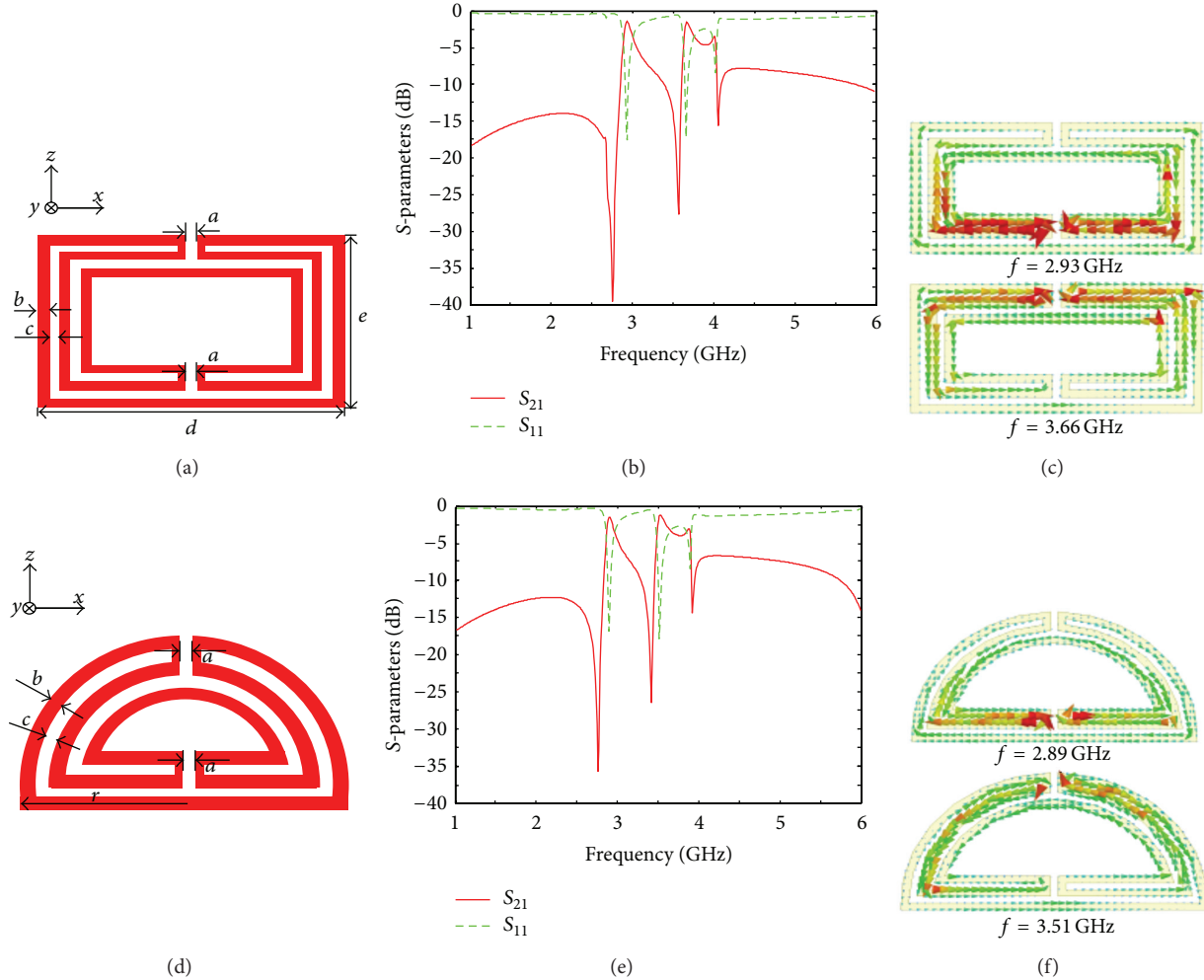


FIGURE 1: (a), (d) Unit cells of the rectangular and circular SLRs, with dimensional parameters in millimeter:  $a = 0.4$ ,  $b = 0.4$ ,  $c = 0.4$ ,  $d = 13.6$ , and  $e = 6.8$ ,  $r = 7.8$ . The period spaces along  $y$ -axis and  $z$ -axis for both cases are 12 mm. (b), (e) Simulated transmission and reflection properties for proposed rectangular and circular SLR unit cells. (c), (f) Surface current distributions at the first two transmission dips of rectangular and circular SLRs.

microstrip feeds) are performed to couple the electromagnetic waves for the rectangular and circular shaped antennas. The conventional planar monopole antennas without the SLRs are also analyzed comparatively to show the advantages of our proposed SLR inspired triple-band antennas. The SLR used in this paper has three or even four distinct resonances states [13–15], which therefore can be easily used to achieve the three operating frequency bands in the ranging of 2.4 to 6 GHz [16], by properly choosing the size. We perform both numerical and experimental methods to discuss such antennas. The proposed triple-band antennas possess compact size and exhibit very well eight-like radiation patterns and low cross-polarizations, which have potential applications for modern wireless communications.

## 2. Design and Fabrications

We first briefly review the electromagnetic characteristics for the rectangular and circular SLRs as shown in Figures 1(a) and

1(d). Both cases are consisting of a single closed loop with three order meandering parts. When the electromagnetic waves act on such inclusions along the  $x$ -axis with the electric field along the  $z$ -axis, they will show two typical magnetic resonance states and a slight electric resonance state, as shown in Figures 1(b) and 1(e), respectively [13, 17]. The surface current distributions at such two magnetic resonance frequencies are shown in Figures 1(c) and 1(f) to indicate resonance characteristics. As analyzed previously [13–15], the two magnetic resonance frequencies can be flexibly adjusted by properly designing the closed loop configurations and the loop size. Therefore, one can easily integrate these SLRs into a conventional antenna. As an example, in this paper, we discuss the planar printed monopole antenna integrated with such rectangular and circular SLR units.

Based on the above introduction, the schematic geometries of the four proposed metamaterial inspired triple-band antennas and the corresponding conventional single-band monopole antennas are shown comparatively in Figure 2,

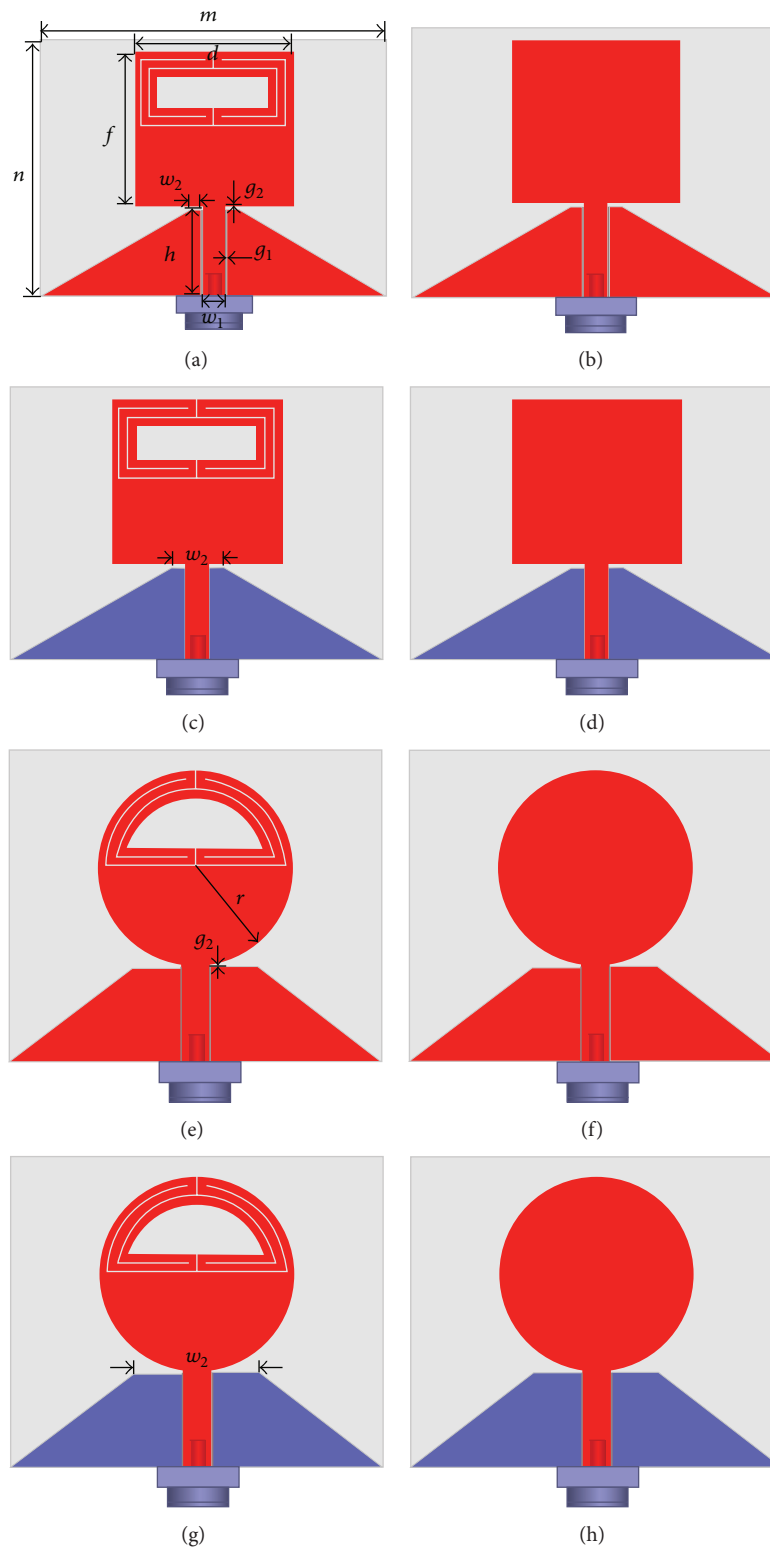


FIGURE 2: The proposed SLR inspired planar monopole antennas and corresponding conventional single band antennas. (a)-(b) CWP fed rectangular patch antennas, (c)-(d) microstrip fed rectangular patch antennas, (e)-(f) CWP fed circular patch antennas, and (g)-(h) microstrip fed circular patch antennas.

TABLE 1: Dimensional parameters for the proposed antennas shown in Figure 2.

Antenna	$a$	$b$	$c$	$d$	$e$	$f$	$g_1$	$g_2$	$h$	$m$	$n$	$r$	$w_1$	$w_2$
(a)	0.4	0.4	0.4	13.6	6.8	13.1	0.2	0.3	7.5	30	22	Non	1.9	0.85
(b)	Non	Non	Non	13.6	Non	13.1	0.2	0.3	7.5	30	22	Non	1.9	0.85
(c)	0.4	0.4	0.4	13.6	6.8	13.1	Non	0.3	7.5	30	22	Non	1.8	4
(d)	Non	Non	Non	13.6	Non	13.1	Non	0.3	7.5	30	22	Non	1.8	4
(e)	0.4	0.4	0.4	Non	Non	Non	0.2	0.3	7.5	30	25	7.8	2.2	3.7
(f)	Non	Non	Non	Non	Non	Non	0.2	0.3	7.5	30	25	7.8	2.2	3.7
(g)	0.4	0.4	0.4	Non	Non	Non	Non	0.3	7.5	30	25	7.8	1.8	10
(h)	Non	Non	Non	Non	Non	Non	Non	0.3	7.5	30	25	7.8	1.8	10

Unit: mm.

respectively. The SLR considered as the half part of the radiation patch is placed on the upper side of the whole patch. After initial numerical analysis, there is a huge impedance mismatch between the SLR and the conventional 50- $\Omega$  CPW/microstrip feed line. Therefore, the bottom part of the patch is used to match the impedance between the SLR and feed line. The whole radiation patch is printed on a 0.8 mm thick Rogers Ro4003 substrate (dielectric constant  $\epsilon_r = 3.55$  and loss tangent  $\tan \delta = 0.0027$ ). For the antennas fed by CPW the ground plane and SLR are printed on the same side of the substrate, while for the antennas fed by microstrip line the ground plane is placed on the opposite side of the substrate. The dimensional parameters for the four kinds of antennas are finally optimized by finite element method based Ansoft HFSS software and concluded in Table 1. At the same time, the corresponding conventional single-band monopole antennas for the two kinds of feed lines are also designed with the same radiation patch size and ground plane size as shown in Figures 2(b), 2(d), 2(f), and 2(h). Finally, through standard printed circuit board fabrication techniques, all antennas are fabricated. In both simulation and measurement procedures, the 50- $\Omega$  microminiature coaxial connectors (operated from DC to 6 GHz) are used to simulate and test the return loss and radiation characteristics for reducing the effects of connectors on the antennas.

### 3. Results

Firstly, the simulated and measured return loss properties of the four proposed SLR inspired antennas and four corresponding conventional antennas are shown in Figure 3. And the key characteristics for the four triple-band antennas are also concluded in Table 2. It can be known that the simulated and measured results shown in Figure 3 and concluded in Table 2 imply a good agreement. For the metamaterial inspired antennas, both the numerical and experimental results show three dips around 2.4, 3.8, and 4.9 GHz. The first operating frequency for these triple band antennas indicates a very narrow bandwidth compared to the following two operating frequencies, as shown in Figure 3 and Table 2. This is mainly due to the strong resonance characteristic of the SLR inspired radiation patches. For practical applications, we can expand the bandwidth by, for example, using low-dielectric-constant substrate with larger dielectric loss or adding wideband impedance matching circuits. In

the higher frequency band (4.5–6 GHz), there is slight frequency shift between numerical and experimental results for each kind of metamaterial inspired antenna. This shift mainly results from the mutual coupling introduced by connector and soldering in the experiment at high frequencies. To confirm this, we performed numerical simulations to show the effect of changing the connector length on the return loss properties. One of the SLR inspired antennas with different connector length as shown in Figure 4(a) is chosen as an example. From Figures 4(b) and 4(c) it can be seen that, with increasing the connect length, the first two operating frequencies keep unchanged while the third one shifts to low frequency with worse return loss property. Therefore, for practical engineering applications, one should consider the connector effect on the performance of such kind of antennas.

On the other hand, the simulated and measured reflection results for the conventional monopole antenna show only one transmission dip located in the range of 3.8–5 GHz. It means that our proposed metamaterial inspired antennas can operate at very lower frequency with the same antenna size for the conventional antenna. Therefore the proposed antennas have a highly compact size property. From the simulated and measured results, we can also know that, for both rectangular and circular shaped radiation patches and both CPW and microstrip feed methods, the triple-band operating properties can be flexibly achieved. It means that we can use any of the four antennas to integrate in the transmit/receive devices depending on the special space and arrangement requirements. Taking deep considerations in Table 2, the SLR inspired rectangular patch antennas have higher operating frequencies for  $f_1$  and  $f_2$  and lower frequency for  $f_3$ , compared with the circular patch antennas. This is because there is different resonance frequencies ratio for the rectangular and circular shaped SLR. So it provides a possible way to control each operating frequency by choosing different shaped resonators.

Figure 5 shows the simulated copolarization and cross-polarization radiation pattern characteristics for the four metamaterial inspired antennas at three corresponding reflection dips. It can be seen that, at the three frequencies, the four antennas exhibit typical eight-like radiation patterns in the copolarization E-plane, whereas in the copolarization H-plane they possess nearly omnidirectional radiation patterns. Moreover, the cross-polarization radiations of the proposed antennas are very low for all the patterns. For examples,

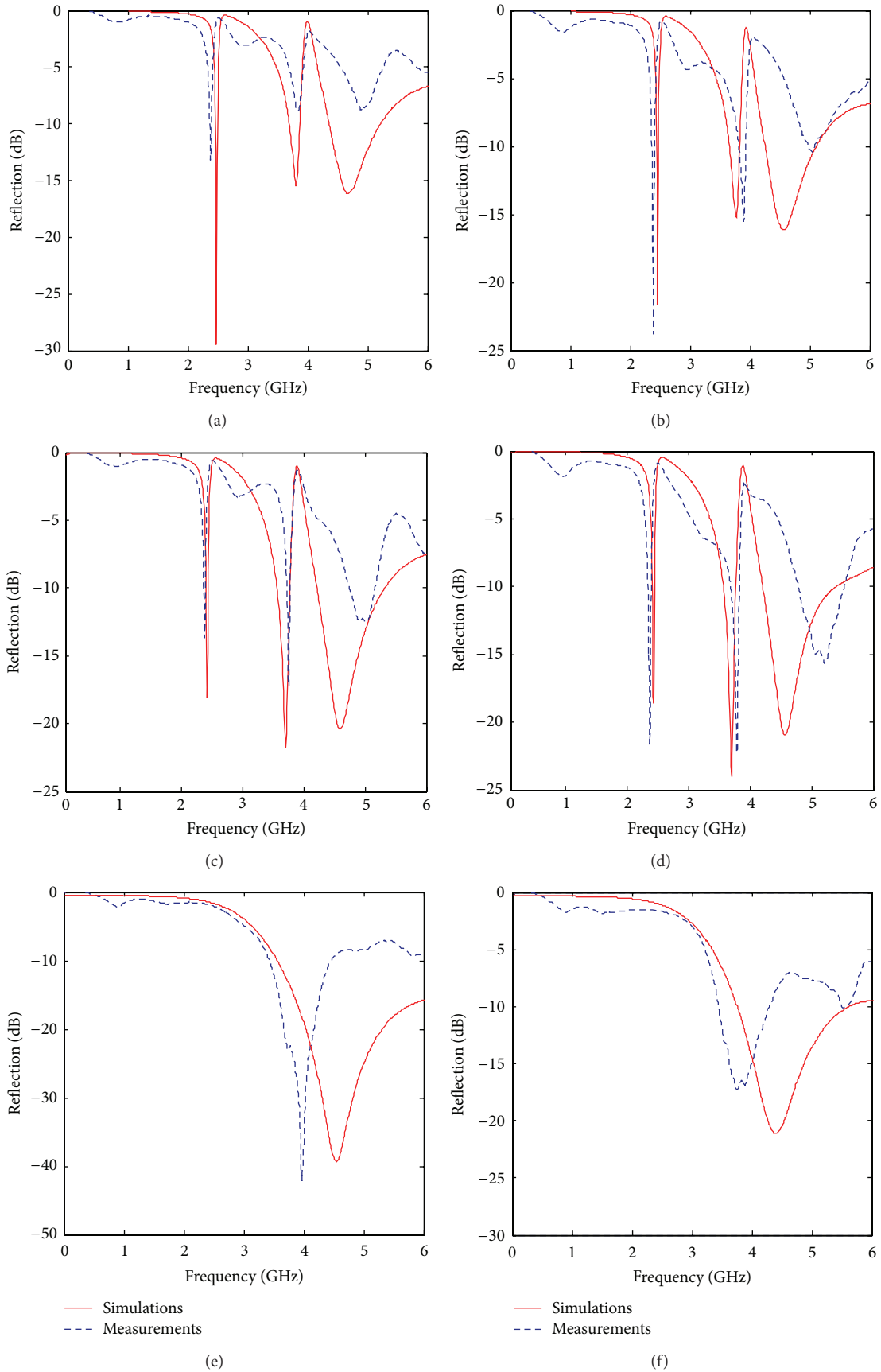


FIGURE 3: Continued.

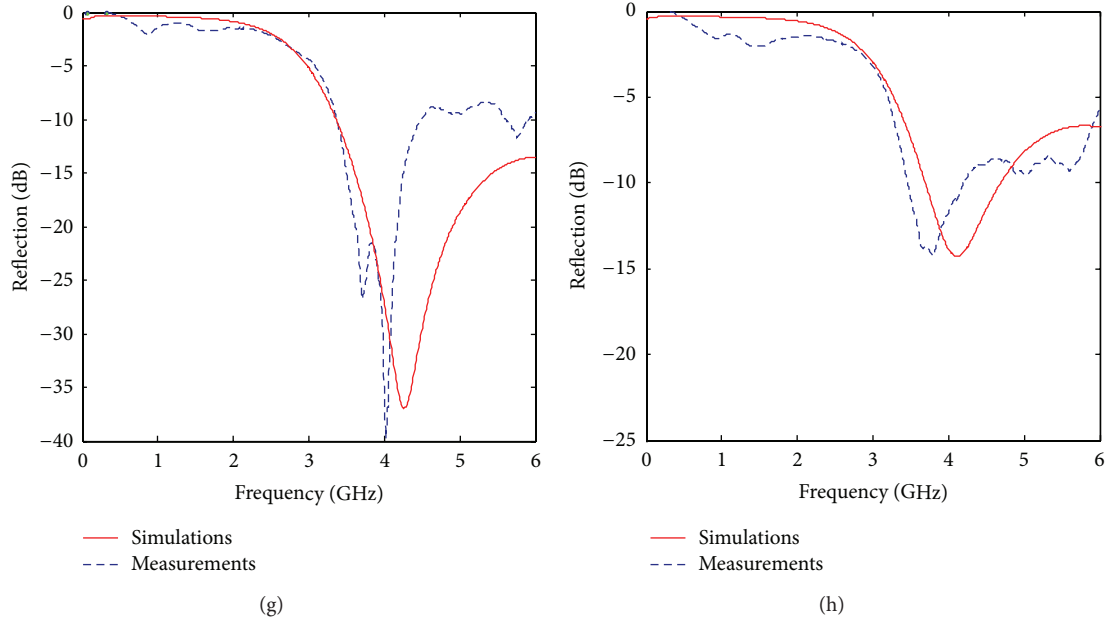


FIGURE 3: (a)–(d) Simulated and measured reflection properties of the four discussed SLR inspired triple-band antennas. (e)–(h) Simulated and measured reflection properties of the corresponding conventional single band antennas.

TABLE 2: Simulated and measured characteristics for the proposed SLR inspired triple-band antennas as shown in Figure 2.

Antenna		$f_1$	$f_2$	$f_3$	Bandwidth for $f_1$	Bandwidth for $f_2$	Bandwidth for $f_3$
(a)	Simulation	2.48	3.8	4.67	0.003	0.1	0.47
	Measurement	2.38	3.83	4.9	0.017	0.14	0.37
(c)	Simulation	2.46	3.76	4.55	0.01	0.1	0.45
	Measurement	2.39	3.9	5.05	0.008	0.05	0.6
(e)	Simulation	2.42	3.7	4.6	0.015	0.05	0.32
	Measurement	2.31	3.71	4.94	0.015	0.015	0.35
(g)	Simulation	2.43	3.7	4.57	0.017	0.04	0.29
	Measurement	2.31	3.75	5.15	0.018	0.03	0.48

Unit: GHz.

there is a 30 dB below the copolarization E-plane over 45° range for the first antenna. And there is a 20 dB below the copolarization H-plane over the omnidirectional angles, at all the three frequencies. These radiation patterns indicate an excellent polarization purity and such patterns are kept very well when integrated with metamaterial unit in the radiation patches. Moreover, it is seen that, for both the CPW and microstrip fed antennas, they have similar radiation pattern at all the three frequencies. Therefore such kind of antenna can be integrated flexibly into other CPW and/or microstrip integrated circuits/devices.

To further characterize the designed antennas, we measured experimentally the radiation pattern, peak gain total, and efficiency in a commercial near field measurement system (Satimo SG 32) as shown in Figure 6, for the four SLR inspired antennas as comparisons. However, for the monopole antenna with such quite small ground plane, the measurement setup will affect mostly on the radiation

pattern, due to the additional coaxial cable. As an example, Figure 7 shows the measured copolarization and cross-polarization radiation patterns for the SLR inspired circular patch triple-band antenna at corresponding frequencies. From Figure 7, it indicates that both E-plane and H-plane copolarization results show moderate distortions and worse cross-polarization characteristics, comparing to the numerical results shown in Figure 5. But we can still see the eight-like radiation patterns in the E-plane copolarization and omnidirectional radiation patterns in the H-plane copolarization. As mentioned above, the difference between measured and simulated results is mainly from the connecting setup of the measurement system as shown in Figure 6. In our near future designs and measurements, such difference can be reduced by using more compact setup and adding some absorbers surrounding the feeding cables.

Table 3 concludes the measured peak gain total and efficiency at the three corresponding reflection dips for all the

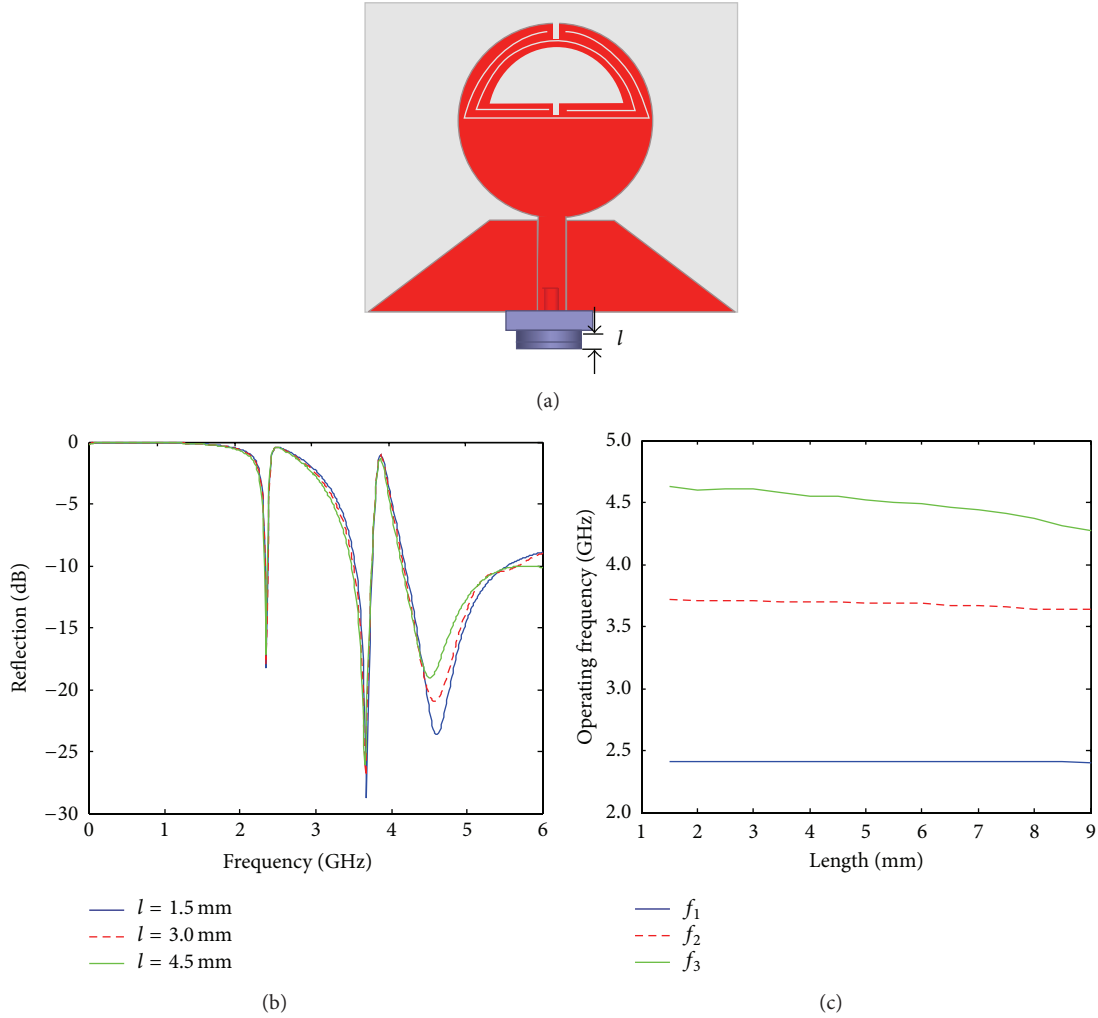


FIGURE 4: (a) One of the SLR inspired antennas with connector of length  $l$ . (b) Simulated reflection properties of the proposed antenna under different connector length. (c) The three operating frequencies as a function of the connector length.

TABLE 3: Measured peak gain total and efficiency properties for the proposed SLR inspired triple-band antennas as shown in Figure 2.

Antenna	Peak gain total for $f_1$	Peak gain total for $f_2$	Peak gain total for $f_3$	Efficiency for $f_1$	Efficiency for $f_2$	Efficiency for $f_3$
(a)	3.7	3.0	3.2	0.58	0.45	0.38
(c)	3.2	3.4	4.2	0.53	0.48	0.47
(e)	3.6	3.2	3.8	0.54	0.51	0.48
(g)	3.3	3.1	4.0	0.53	0.47	0.45

Gain unit: dBic.

four SLR inspired antennas. It can be seen that all of the four antennas at each frequency have the same gain level. However, the measured gain total looks like higher than a typical omnidirectional monopole antenna. This is mainly because of the previously mentioned moderate distortions. Moreover, at higher operating frequency, the efficiency dropped down slightly. This is because the loss at such higher frequency is larger than the condition in the lower frequency. From the above simulated and measured results, however, we can still conclude such metamaterial inspired triple-band antennas can be easily used to modern wireless communications.

Comparing to the previously well-developed metamaterial inspired monopole antennas [12], our designs have near-same return loss and radiation performances while possessing simpler implementation method.

#### 4. Conclusions

In this paper, comparing with the conventional monopole antennas, four kinds of novel metamaterial inspired miniaturized triple-band antennas consisting of a SLR as part of the radiation patch and fed with CPW and microstrip

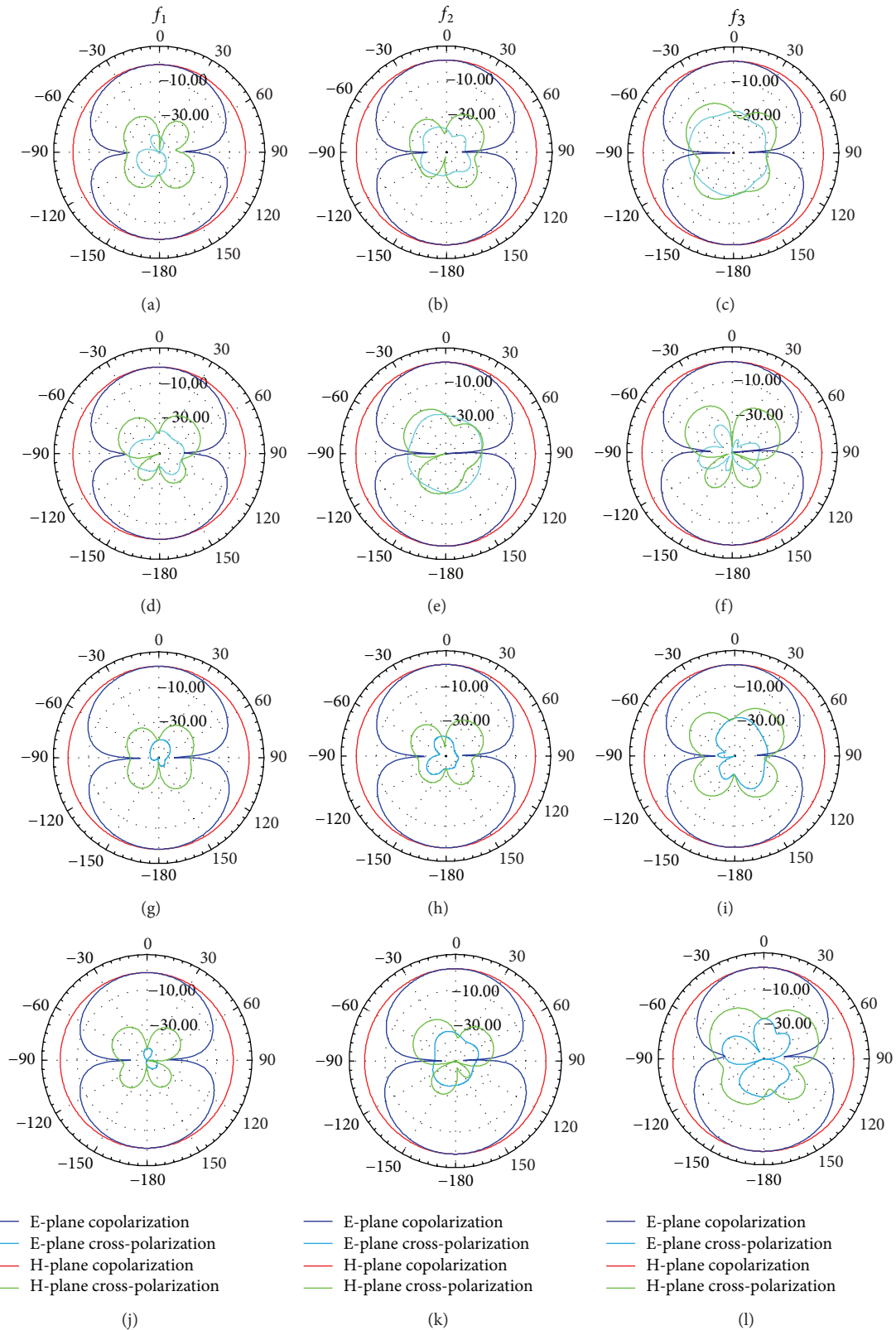


FIGURE 5: Simulated E-plane and H-plane copolarization and cross-polarization radiation patterns for the proposed four SLR inspired triple-band antennas. (a)–(c) CWP fed squared patch antennas, (d)–(f) microstrip fed squared patch antennas, (g)–(i) CWP fed circular patch antennas, and (j)–(l) microstrip fed circular patch antennas.

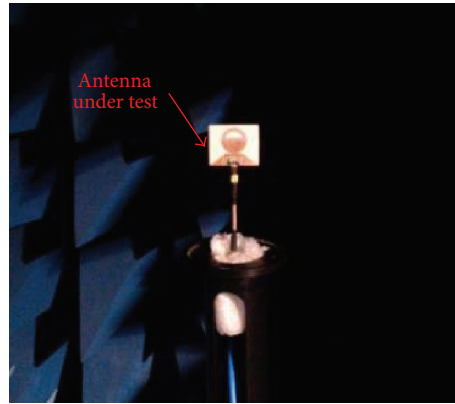


FIGURE 6: Photograph of the Satimo SG 32 near field measurement setup and the triple-band antenna under test.

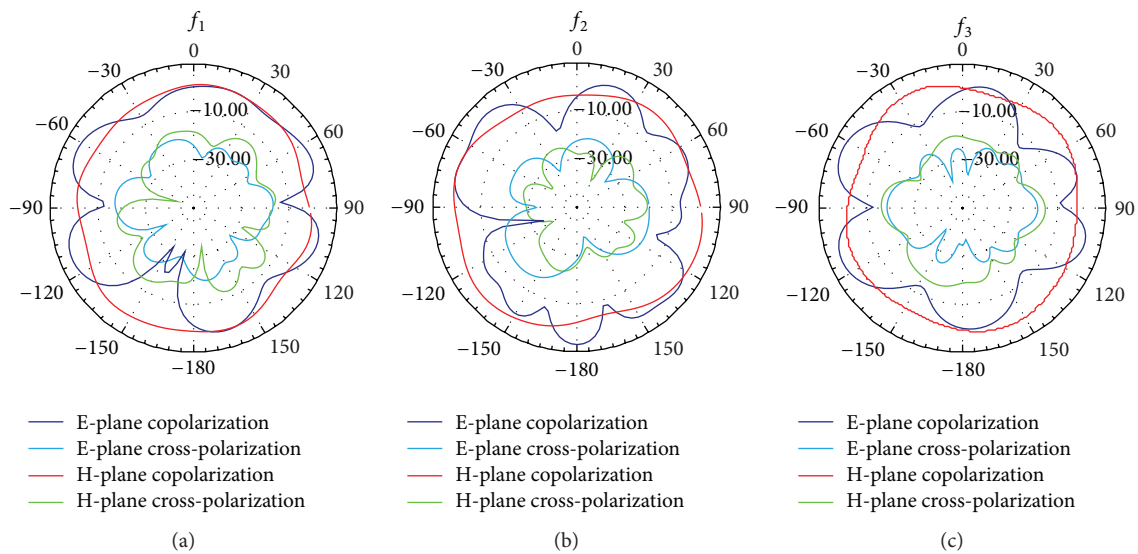


FIGURE 7: Measured E-plane and H-plane copolarization and cross-polarization radiation patterns for the selected CWP fed circular SLR inspired triple-band antennas at three operating frequencies.

transmission lines, respectively, are discussed through numerical simulations and experimental demonstrations. The proposed antennas exhibit comparable radiation pattern with the conventional monopole antennas, including very well eight-like radiation patterns and low cross-polarizations and high peak gain total and efficiency. Such antennas have potential applications for modern wireless communications and can be integrated flexibly into other CPW and/or microstrip integrated circuits.

### Conflict of Interests

The authors declare that there is no conflict of interests regarding the publication of this paper.

### Acknowledgments

This work was supported in part by the National Natural Science Foundation of China (Grant no. 61371047) and by Research Fund for the Doctoral Program of Higher Education of China (Grant no. 20110185110014). Yongjun Huang also

gratefully acknowledges the Scholarship Award for Excellent Doctoral Student granted by Ministry of Education of China (Grant no. A03003023901006).

### References

- [1] M. Niroo-Jazi and T. A. Denidni, "A new triple-band circular ring patch antenna with monopole-like radiation pattern using a hybrid technique," *IEEE Transactions on Antennas and Propagation*, vol. 59, no. 10, pp. 3512–3517, 2011.
- [2] J.-H. Yoon, Y.-C. Rhee, and W.-S. Kim, "A rectangular ring, open-ended monopole antenna with two symmetric strips for WLAN and WiMAX applications," *International Journal of Antennas and Propagation*, vol. 2013, Article ID 109450, 9 pages, 2013.
- [3] Y.-T. Wan, D. Yu, and F.-S. Zhang, "Miniature multi-band monopole antenna using spiral ring resonators for radiation pattern characteristics improvement," *Electronics Letters*, vol. 49, no. 6, pp. 382–384, 2013.
- [4] P. Wang, G.-J. Wen, Y.-J. Huang, and Y.-H. Sun, "Compact CPW-fed planar monopole antenna with distinct triple bands

- for WiFi/WiMAX applications,” *Electronics Letters*, vol. 48, no. 7, pp. 357–359, 2012.
- [5] J. Wang and X. He, “Analysis and design of a novel compact multiband printed monopole antenna,” *International Journal of Antennas and Propagation*, vol. 2013, Article ID 694819, 8 pages, 2013.
- [6] J. T. Rayno and S. K. Sharma, “Compact spirograph planar monopole antenna covering C-/X-band with invariant radiation pattern characteristics,” *IEEE Transactions on Antennas and Propagation*, vol. 60, no. 12, pp. 6002–6007, 2012.
- [7] D. R. Smith, W. J. Padilla, D. C. Vier, S. C. Nemat-Nasser, and S. Schultz, “Composite medium with simultaneously negative permeability and permittivity,” *Physical Review Letters*, vol. 84, no. 18, pp. 4184–4187, 2000.
- [8] R. W. Ziolkowski, P. Jin, and C.-C. Lin, “Metamaterial-inspired engineering of antennas,” *Proceedings of the IEEE*, vol. 99, no. 10, pp. 1720–1731, 2011.
- [9] D. Jiang, Y. Xu, R. Xu, and W. Lin, “Compact dual-band-notched UWB planar monopole antenna with modified CSRR,” *Electronics Letters*, vol. 48, no. 20, pp. 1250–1252, 2012.
- [10] L.-M. Si, W. Zhu, and H.-J. Sun, “A compact, planar, and CPW-fed metamaterial-inspired dual-band antenna,” *IEEE Antennas and Wireless Propagation Letters*, vol. 12, pp. 305–308, 2013.
- [11] L.-M. Si and X. Lv, “CPW-FED multi-band omni-directional planar microstrip antenna using composite metamaterial resonators for wireless communications,” *Progress in Electromagnetics Research*, vol. 83, pp. 133–146, 2008.
- [12] J. Zhu, M. A. Antoniades, and G. V. Eleftheriades, “A compact tri-band monopole antenna with single-cell metamaterial loading,” *IEEE Transactions on Antennas and Propagation*, vol. 58, no. 4, pp. 1031–1038, 2010.
- [13] E. Ekmekci and G. Turhan-Sayan, “Single loop resonator: dual-band magnetic metamaterial structure,” *Electronics Letters*, vol. 46, no. 5, pp. 324–325, 2010.
- [14] O. Yurduseven, A. E. Yilmaz, and G. Turhan-Sayan, “Triangular-shaped single-loop resonator: a triple-band metamaterial with MNG and ENG regions in S/C bands,” *IEEE Antennas and Wireless Propagation Letters*, vol. 10, pp. 701–704, 2011.
- [15] O. Yurduseven, A. E. Yilmaz, and G. Turhan-Sayan, “Hybrid-shaped single-loop resonator: a four-band metamaterial structure,” *Electronics Letters*, vol. 47, no. 25, pp. 1381–1382, 2011.
- [16] R. Wen, “Compact planar triple-band monopole antennas based on a single-loop resonator,” *Electronics Letters*, vol. 49, no. 15, pp. 916–918, 2013.
- [17] J. Zhong, F. Wang, G. Wen et al., “Tunable triple-band negative permeability metamaterial consisting of single-loop resonators and ferrite,” *Journal of Electromagnetic Waves and Applications*, vol. 27, no. 3, pp. 267–275, 2013.

## Research Article

# Metamaterial Inspired Microstrip Antenna Investigations Using Metascreens

Muhammad Tauseef Asim<sup>1,2</sup> and Mushtaq Ahmed<sup>1,2</sup>

<sup>1</sup>Pakistan Institute of Engineering and Applied Sciences (PIEAS), Islamabad 44000, Pakistan

<sup>2</sup>National Institute of Lasers and Optronics (NILOP), Islamabad 44000, Pakistan

Correspondence should be addressed to Muhammad Tauseef Asim; [tauseefasim@yahoo.com](mailto:tauseefasim@yahoo.com)

Received 15 October 2014; Revised 10 February 2015; Accepted 11 February 2015

Academic Editor: Hui Feng Ma

Copyright © 2015 M. Tauseef Asim and M. Ahmed. This is an open access article distributed under the Creative Commons Attribution License, which permits unrestricted use, distribution, and reproduction in any medium, provided the original work is properly cited.

A dual layer periodically patterned metamaterial inspired antenna on a low cost FR4 substrate is designed, simulated, fabricated, and tested. The eigenmode dispersion simulations are performed indicating the left handed metamaterial characteristics and are tunable with substrate permittivity. The same metamaterial unit cell structure is utilized to fabricate a metascreen. This metascreen is applied below the proposed metamaterial antenna and next used as superstrate above a simple patch to study the effects on impedance bandwidth, gain, and radiation patterns. The experimental results of these antennas are very good and closely match with the simulations. More importantly, the resonance for the proposed metamaterial antenna with metascreen occurs at the left handed (LH) eigenfrequency of the metamaterial unit cell structure. The measured  $-10$  dB bandwidths are 14.56% and 22.86% for the metamaterial antenna with single and double metascreens, respectively. The metascreens over the simple patch show adjacent dual band response. The first and second bands have measured  $-10$  dB bandwidths of 9.6% and 16.66%. The simulated peak gain and radiation efficiency are 1.83 dBi and 74%, respectively. The radiation patterns are also very good and could be useful in the UWB wireless applications.

## 1. Introduction

Patch antennas have been the most demanded candidates for research activity due to their multiple advantages like low cost, low profile, being easy to fabricate, compact size, and conformability with the monolithic microwave integrated circuits (MMIC) [1, 2]. It is the most widely used component in the wireless industry.

Metamaterials are artificially engineered homogeneous media with controllable electric and magnetic responses to give unusual and useful phenomena [3]. These materials are characterized by either dispersion relations or by constitutive electromagnetic parameters. The first formal theoretical studies on media with simultaneous double negative parameters were done by Veselago who predicted some novel phenomena inferred from these metamaterials in his famous paper [4]. After long time, Pendry et al. in 1990s demonstrated electric plasma (negative permittivity) by wire structures [5] and then

magnetic plasma (negative permeability) by ring structures [6]. The first experimental demonstration for double negative structures was performed by Smith et al. [7]. Since the practical advent of metamaterials, these have been keenly studied as a potential artificial material for a number of applications in the microwave and optical region [8–11]. One such application is the substrate material for microstrip patch antennas. Researchers have investigated extensively to improve its features like return loss, VSWR, bandwidth, gain, and directivity [12–17].

The metamaterial substrates are realized based on 3D regular periodic arrangements of split ring resonator (SRR) and rod structures [18–22]. These types of substrates are bulky and very much lossy in the microwave region which hinders their use for the wireless applications [23]. Alternatively many researchers have studied planar transmission line metamaterials for antenna applications due to their ease of fabrication, compact size, and high efficiency [24–29].

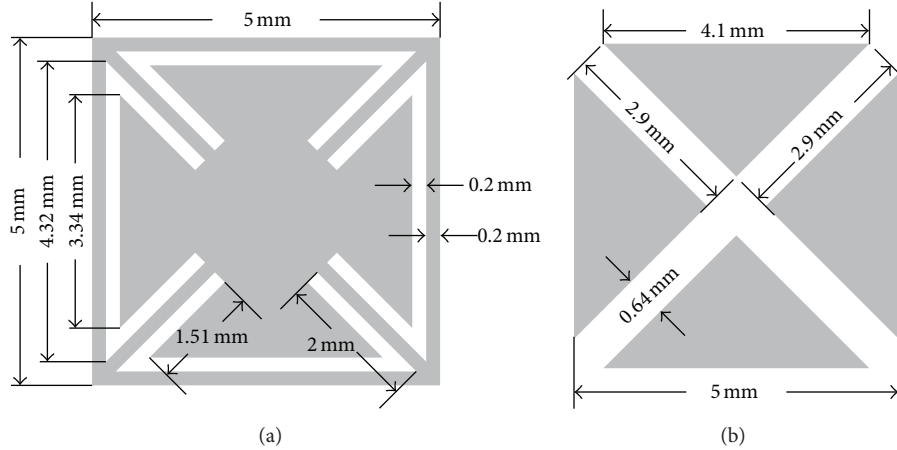


FIGURE 1: Unit cell: (a) top and (b) bottom dimensions.

There are many types of planar metamaterial based antennas [30], which are inspired from the metamaterial unit cell designs to enhance their performance. These planar metamaterial antennas can be broadly categorized as (i) dispersion engineered antennas [31–34], (ii) metamaterial unit cell loading antennas [35, 36], (iii) meta-resonator antennas [37, 38], and (iv) meta-surface loaded antennas [39–42].

Previously Li et al. [31] demonstrated a patch antenna based on the modified form of the planar metamaterial structure proposed by Matsunaga et al. [43]. These structures were proposed to avoid the use of via hole in the unit cell for the ease of fabrication purposes. These structures were designed using left handed (LH) dispersion engineering approach. Recently Xiong et al. [44] also demonstrated a patch antenna based on similar structure with modified ground pattern for enhanced performance.

The aim of our work is to design, simulate, fabricate, and investigate a novel metamaterial antenna realized by the metamaterial unit cell structure proposed by Matsunaga et al. [43]. The same metamaterial structure is further utilized to fabricate a metascreen. The size of the metascreen is kept equal to the size of antenna to miniaturize the overall design. The proposed metascreen is used in the near field of the proposed metamaterial antenna and also over a simple patch antenna to investigate its effect on impedance bandwidth, gain, and radiation patterns.

## 2. Geometrical Model

The metamaterial unit cell is a dual layer planar copper structure on FR4 substrate for which the dimensions for the top and bottom layers are shown in Figure 1. The unit cell top layer consists of a small square copper patch of  $(5 \times 5)$  mm with disconnected triangular shaped slit gaps on the edges. The bottom layer consists of similar copper patch with cross slits, having gap width of 0.64 mm. This unit cell is repeated twice in the  $xy$  plane to generate the pattern of the patch antenna. The dimensions of the bottom and top antenna

layers are shown in Figures 2(a) and 2(b), respectively. The substrate thickness is 1.51 mm.

The proposed metamaterial (MTM) antenna is parametrically analyzed in commercial FEM based simulation software HFSS to get the optimum values for different antenna dimensions. The design gives  $\text{FeedLoc} = 0.5$  mm,  $\text{FeedL} = 4.2$  mm,  $\text{FeedW} = 3$  mm,  $L = 5$  mm,  $W = 10$  mm,  $\text{SubL} = 17.2$  mm,  $\text{SubW} = 26$  mm,  $\text{SubV} = 8$  mm, and  $\text{GndGap} = 0.5$  mm. Further we designed, simulated, fabricated, and investigated the MTM antenna and the simple patch antenna with metascreens made of the same metamaterial unit cell structure. Figure 3 shows the perspective views for the MTM antenna, MTM antenna with single and double metascreens. The gap between the antenna and the metascreen is also parametrically varied to investigate the effect of  $\text{SubGap}$ .

## 3. Results and Discussions

**3.1. Dispersion Plots.** Different eigenmode dispersion plots for the same structure on different substrate materials are shown in Figure 4. The left handed material (LHM) characteristic is indicated by the negative slope of these curves. The permittivity values of the substrates Rogers, FR4, and Duroid are 10.2, 4.4, and 2.2, respectively, giving eigenfrequencies approximately around 6 GHz, 9.1 GHz, and 11.5 GHz, respectively. The curves illustrate that the eigenmode response shifts towards the higher frequency side with the decrease of substrate permittivity. So permittivity variation keeps left handed characteristics of the curve intact but only scales the frequency response to the desired frequency band giving an option for substrate based tunability. All the curves give LH characteristics between points  $X$  and  $M$ . The steepest descent makes a valley close to point  $M$ . These curve variations suggest the nonhomogeneous and anisotropic nature of the unit cell structure. The LH eigenfrequency band is very narrow confirming the band limited and dispersive nature of the metamaterial structures. The effect of substrate thickness is studied and it does not change the left handed characteristics of the curve. Interchanging the top and bottom structure in

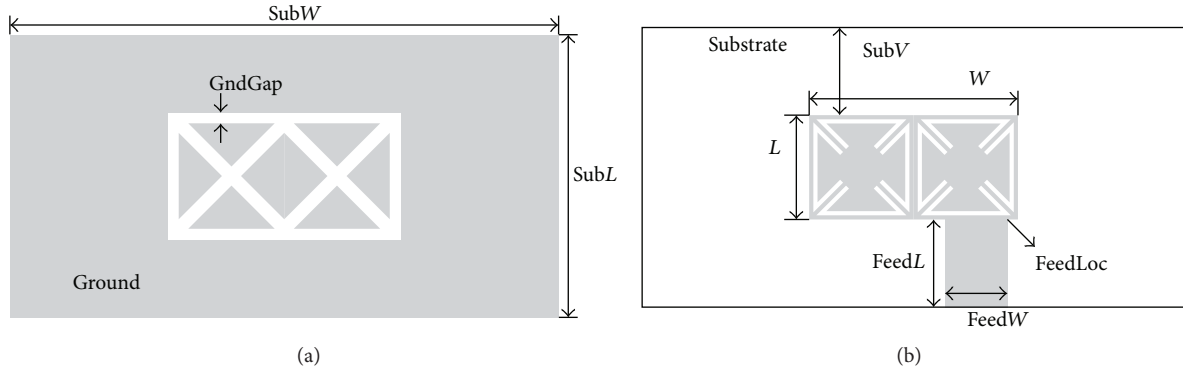


FIGURE 2: Patch antenna dimensions: (a) bottom view and (b) top view.

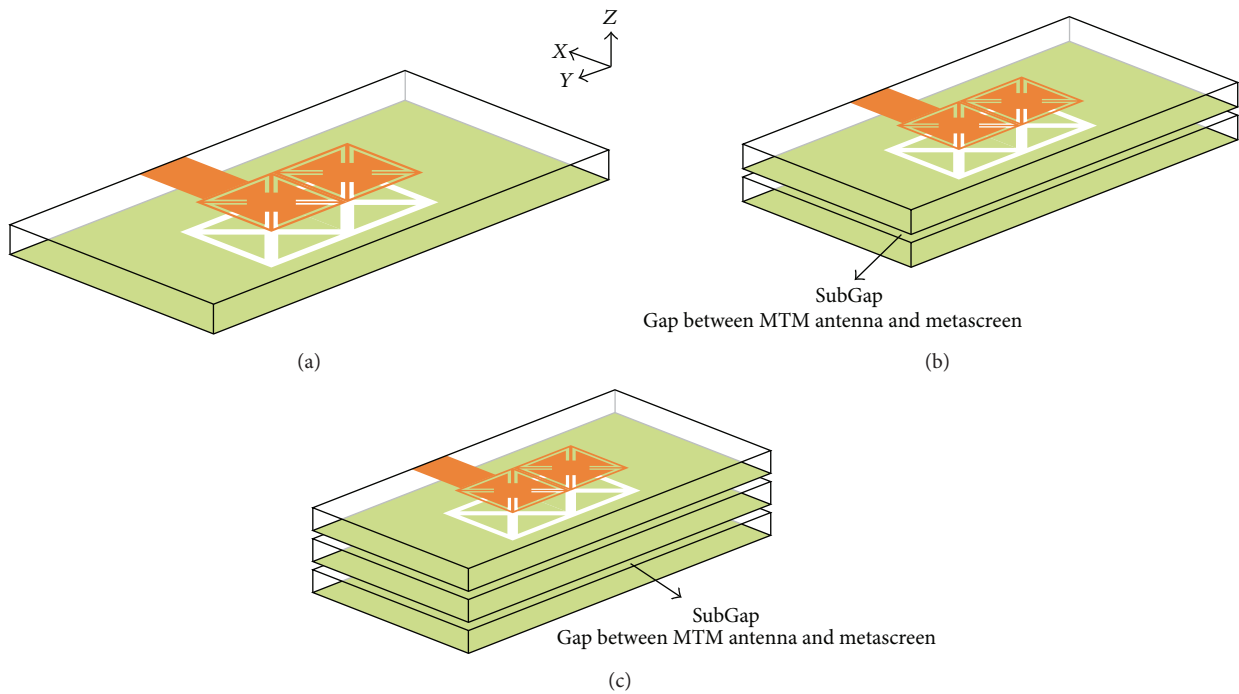


FIGURE 3: Perspective views of antennas with metascreens: (a) metamaterial (MTM) antenna, (b) MTM antenna with single metascreen, and (c) MTM antenna with double metascreen.

the unit cell also does not change the characteristics of the eigenresponse.

**3.2. Simple Patch Antenna.** A simple patch antenna with dimensions for length  $L = 5$  mm and width  $W = 10$  mm is designed, simulated, fabricated, and tested. The purpose is to compare the performance of simple patch antenna with MTM antenna and MTM antenna with metascreens, all having the same dimensions. This antenna gives resonance at 12.5 GHz with off-centered feed location at  $\text{FeedLoc} = 0.5$  mm, as shown in Figure 5(a). This is about 3 GHz away from the eigenresponse. Plots for various  $\text{FeedLoc}$  are shown in Figure 5(a). The measured  $-10$  dB bandwidth is 8.4%. The simulated peak gain and radiation efficiency are 3.9 dBi and

69%, respectively. The fabricated antenna at 13 GHz has a total size of  $(0.216\lambda_0 \times 0.433\lambda_0 \times 0.065\lambda_0)$ .

**3.3. MTM Antenna with Single and Double Metascreens.** When we simulated the proposed MTM antenna having the dimensions  $(5 \text{ mm} \times 10 \text{ mm})$  with  $\text{FeedLoc}$  at 0.5 mm, it gave a resonance at 8.85 GHz, as shown in Figure 6(a) (solid line). The response is very weak but very close to the eigenresponse at 9.1 GHz. When we made simulation with a metascreen made of the same structure and size below this metamaterial antenna, it also gave resonance very close to the eigenfrequency but stronger than the simple MTM antenna, as shown in Figure 6(a) (dash line). The weak response is due to the lossy nature of these metamaterials and this fact

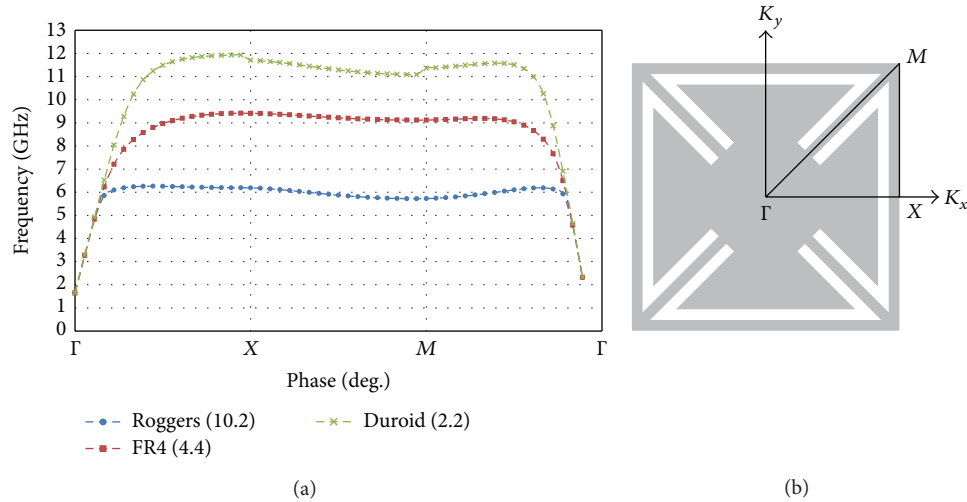


FIGURE 4: (a) Eigenfrequency dispersion plots for the metamaterial unit cell and (b) Brillouin zone showing the phase traversal path for dispersion plots in the  $xy$ -plane.

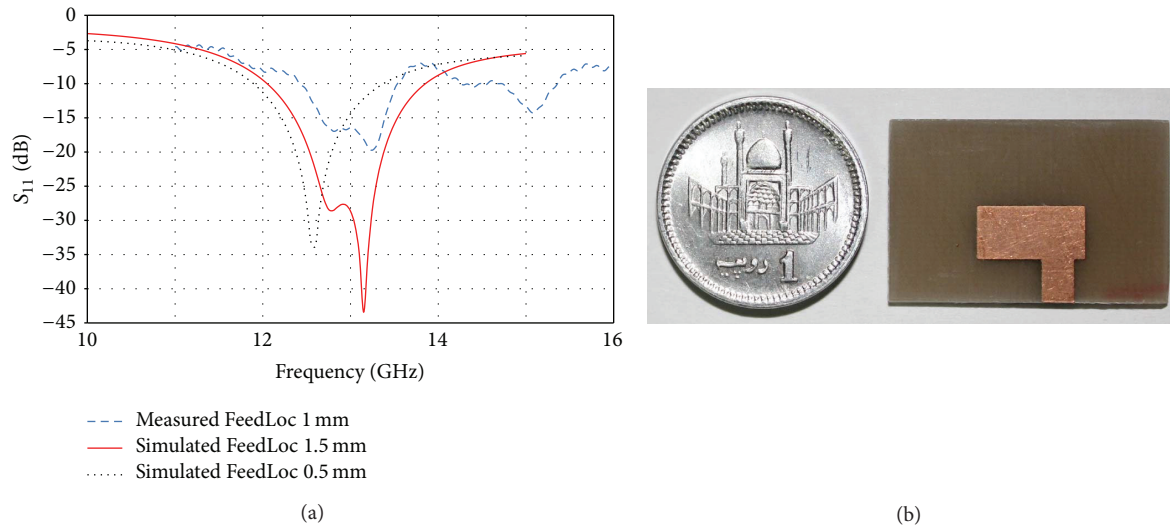


FIGURE 5: (a) Measured and simulated return loss for simple patch and (b) photograph for the fabricated simple patch (5 mm  $\times$  10 mm); FeedLoc = 1 mm.

is already reported in literature [30]. Another factor may be the loss tangent of FR4 material which is high at higher frequencies.

We fabricated the MTM antenna and metascreens. Experiments were performed by using single and then double metascreens below the metamaterial antenna. We got the measured resonance at the LH Eigenfrequency of 9.1 GHz as shown and compared in Figure 7 with simulation results. The overall curve shapes are similar with some shift seen in the resonant frequencies. The reason for this frequency shift is due to the difference in boundary conditions [30]. The dispersion plots are obtained by using periodic boundary conditions while antennas use limited unit cells with radiation boundary conditions. Another factor is the permittivity variation of commercial FR4 substrates. It decreases with frequency and this causes the resonance to move towards higher

side as depicted in Figure 7 (blue cross line). The comparison shows that the measured results for the single (solid line) and double metascreens (solid square line) under the MTM antenna closely match with each other in the frequency range from 8 GHz to 9.5 GHz. However there is another resonance that appeared near 7.6 GHz in the measured results for double metascreen which does not appear in the measured results for the single metascreen. The simulated results for the double metascreen are not shown since they follow the results for single metascreen case. The measured  $-10$  dB bandwidths at 9.1 GHz are 14.56% (simulated 22%) and 22.86% for the MTM antenna with single and double metascreens, respectively. The simulated peak gain and radiation efficiency are 0.7 dBi and 90% for single metascreen case. The fabricated MTM antenna with single metascreen at 9.1 GHz has a total size of  $(0.152\lambda_0 \times 0.303\lambda_0 \times 0.106\lambda_0)$ .

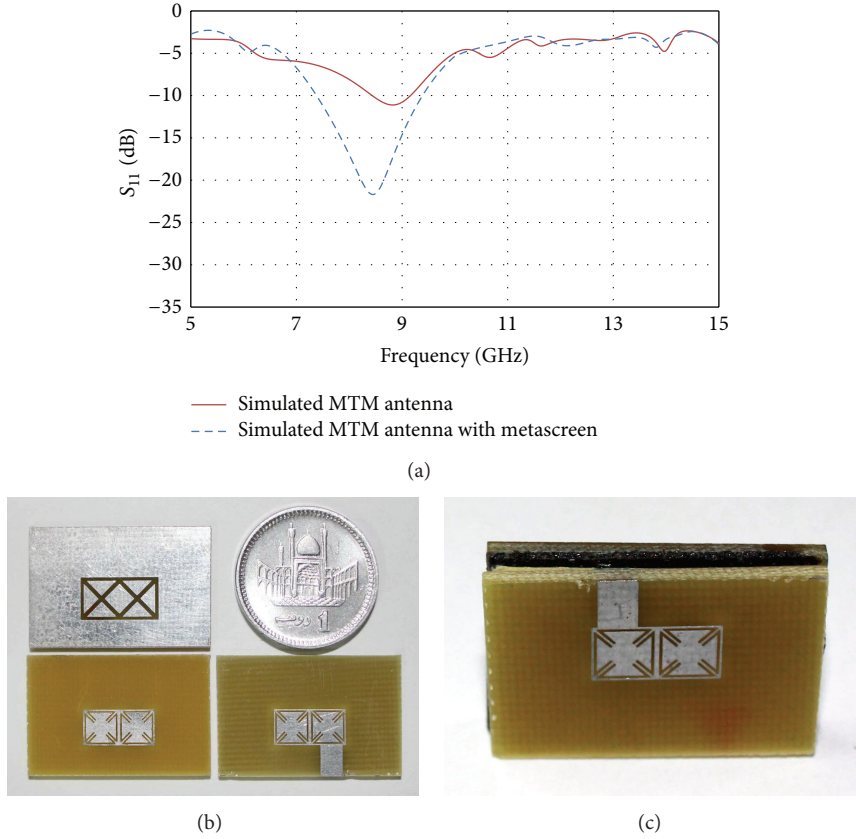


FIGURE 6: (a) Response for simulated MTM antenna and MTM antenna with single metascreen SubGap = 1.5 mm. (b) Fabricated MTM antenna, metascreen top and bottom layers. (c) Side view showing the adhesive foam tape of 1.5 mm between MTM antenna and metascreen.

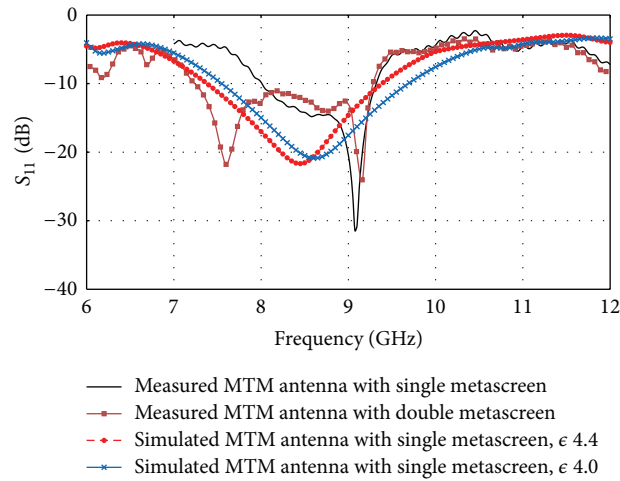


FIGURE 7: Return loss for metamaterial antenna with single and double metascreens.

3.4. *Inverted Metascreen over Simple Patch Antenna.* We performed more experiments by putting the metascreen slab inverted upside down over the simple patch antenna of the same size (5 mm by 10 mm) as shown in the perspective view of Figure 8(b). As can be seen the measured resonances shown in Figure 5(a) of the simple patch at 13 GHz and 15 GHz have been changed as shown in Figure 9 (solid line) by using

an inverted metascreen. The measured result is compared with the simulation results by varying the SubGap, that is, the gap between a simple patch and the metascreen. There are two adjacent resonances in the measured result with a small stopband of about 250 MHz. The first and second bands have measured -10 dB bandwidths of 9.6% and 16.66% (21% simulations). But these resonances are far away from

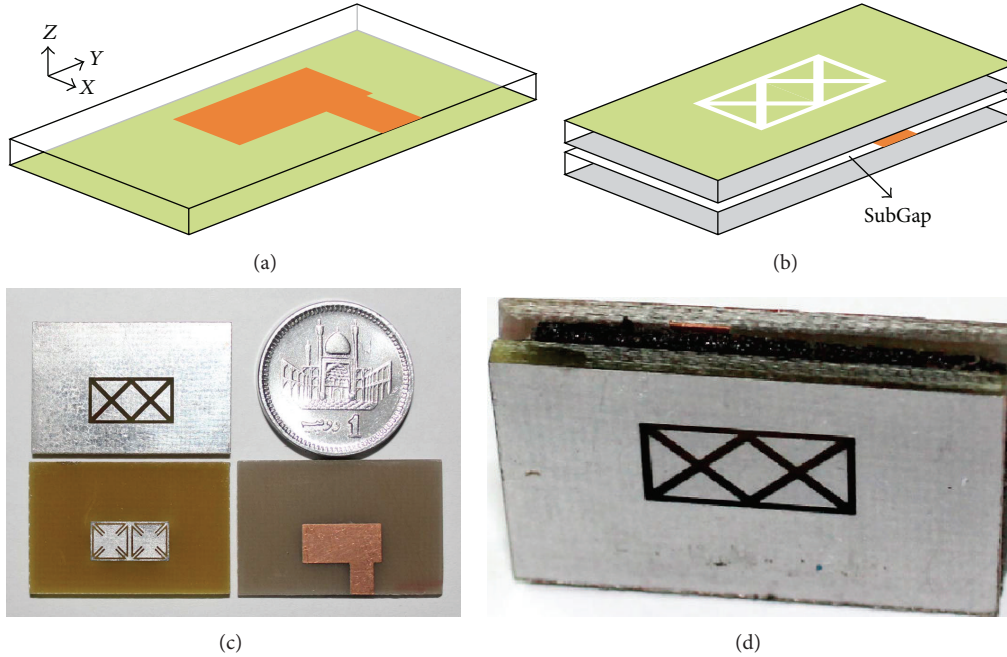


FIGURE 8: Perspective views for (a) simple patch antenna, (b) metascreen over simple patch antenna, (c) photograph for the fabricated simple patch antenna with metascreen bottom and top layers, and (d) side view.

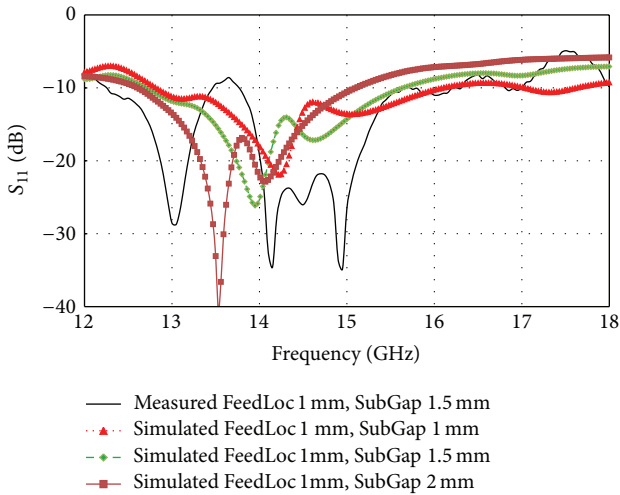


FIGURE 9: Measured and simulated return loss for inverted metascreen over simple patch antenna.

the eigenfrequency of the MTM unit cell, that is, 9.1 GHz. Nevertheless, these metascreens can be used to broaden the impedance bandwidths around the normal resonances of the simple patch antennas. The simulated peak gain and radiation efficiency are 1.83 dBi and 74%, respectively, at 13.95 GHz. The fabricated antenna with single metascreen at 13 GHz has a total size of  $(0.216\lambda_0 \times 0.433\lambda_0 \times 0.13\lambda_0)$ .

**3.5. Radiation Patterns.** The two-dimensional radiation patterns for the MTM antenna, MTM antenna with single metascreen, and simple patch with inverted metascreen are

plotted in Figures 10, 11, and 12, respectively. The simple MTM antenna radiates at 8.85 GHz which is mostly along the bore side and back side in the  $xz$  plane while it is from 0 to  $-180$  degrees in the  $yz$  plane. The single metascreen under the MTM antenna also radiates along the bore side and back side in the  $xz$  and  $yz$  planes. The radiation pattern is also broadband as can be seen from response of two frequencies within the band. The radiation pattern for the metascreen over the simple patch is directional with maximum from  $-30$  to  $-120$  degrees in the  $xz$  plane and 0 to  $-60$  degrees in the  $yz$  plane.

## 4. Conclusion

In conclusion a dual layer metamaterial inspired microstrip antenna on a low cost FR4 substrate is designed, simulated, fabricated, and tested. The metamaterial structure is dispersion engineered and its eigenfrequency is around 9.1 GHz for the FR4 material. This eigenfrequency can be tuned to higher frequencies by using other substrate materials with lower permittivity values. This structure is utilized to fabricate a metascreen. This metascreen is applied under the proposed MTM antenna and also over a simple patch antenna to study their performance parameters such as impedance bandwidths, gains, and radiation patterns. The measured  $-10$  dB bandwidths at 9.1 GHz are 14.56% (simulated 22%) and 22.86% for the MTM antenna with single and double metascreens, respectively. The simulated peak gain and radiation efficiency are 0.7 dBi and 90% for single metascreen case. The  $-10$  dB bandwidth for the simple patch with inverted metascreen is measured as 9.6% and 16.66% (21% simulations) for dual band operation. The simulated

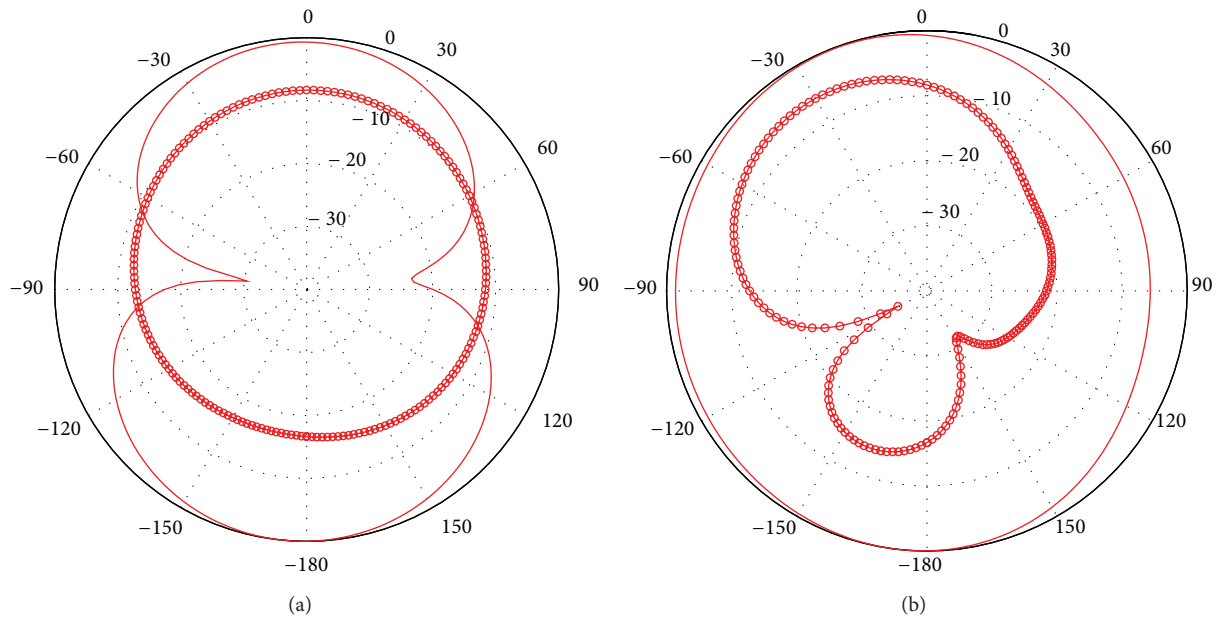


FIGURE 10: Simulated radiation patterns for MTM antenna, copolarization (solid line) and cross-polarization (solid circle line) at 8.85 GHz: (a)  $xz$  plane and (b)  $yz$  plane.

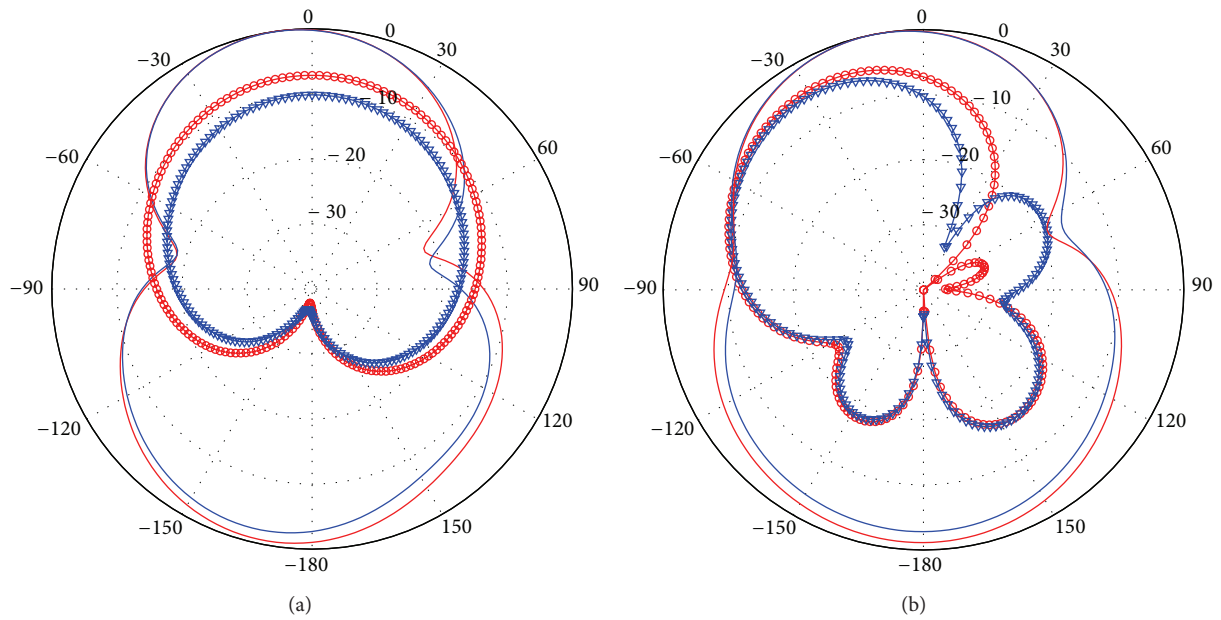


FIGURE 11: Simulated radiation patterns for MTM antenna with single metascreen, copolarization (solid red line) and cross-polarization (solid red circle line) at 8.45 GHz, copolarization (solid blue line) and cross-polarization (solid blue triangle line) at 9 GHz: (a)  $xz$  plane and (b)  $yz$  plane.

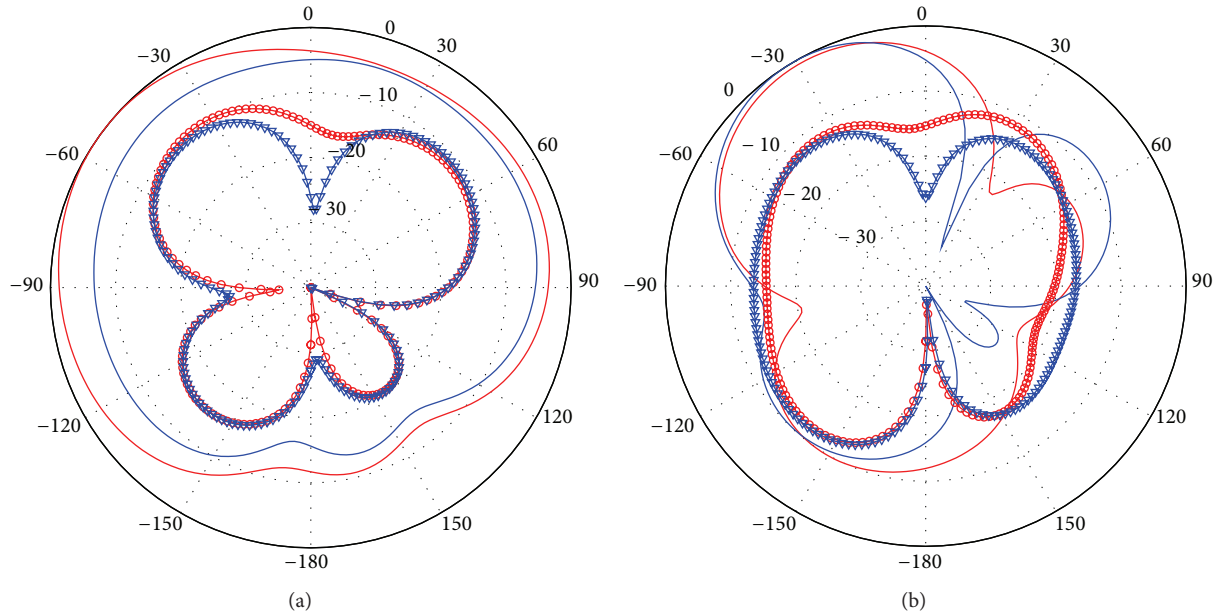


FIGURE 12: Simulated radiation patterns for simple patch with inverted metascreen, copolarization (solid red line) and cross-polarization (solid red circle line) at 13.95 GHz, copolarization (solid blue line) and cross-polarization (solid blue triangle line) at 14.64 GHz: (a)  $xz$  plane and (b)  $yz$  plane.

peak gain and radiation efficiency are 1.83 dBi and 74%, respectively. The radiation patterns are also very good and could be useful for the UWB wireless applications.

### Conflict of Interests

The authors declare that there is no conflict of interests regarding the publication of this paper.

### Acknowledgments

This work is supported by the Higher Education Commission, Pakistan, through financial Grant no. 17-5-4(Eg4-032) HEC/Sch/2007. The authors are indebted for providing the fabrication facility by the National Institute of Lasers and Optronics, Islamabad, Pakistan.

### References

- [1] C. A. Balanis, *Antenna Theory: Analysis and Design*, John Wiley & Sons, Hoboken, NJ, USA, 2005.
- [2] K.-L. Wong, *Compact and Broadband Microstrip Antennas*, Wiley, New York, NY, USA, 2002.
- [3] M. Lapine and S. Tretyakov, "Contemporary notes on metamaterials," *IET Microwaves, Antennas and Propagation*, vol. 1, no. 1, pp. 3–11, 2007.
- [4] V. G. Veselago, "The electrodynamics of substances with simultaneous negative values of  $\epsilon$  and  $\mu$ ," *Soviet Physics Uspekhi*, vol. 10, no. 4, pp. 509–514, 1968.
- [5] J. B. Pendry, A. J. Holden, W. J. Stewart, and I. Youngs, "Extremely low frequency plasmons in metallic mesostructures," *Physical Review Letters*, vol. 76, no. 25, pp. 4773–4776, 1996.
- [6] J. B. Pendry, A. J. Holden, D. J. Robbins, and W. J. Stewart, "Magnetism from conductors and enhanced nonlinear phenomena," *IEEE Transactions on Microwave Theory and Techniques*, vol. 47, no. 11, pp. 2075–2084, 1999.
- [7] D. R. Smith, W. J. Padilla, D. C. Vier, S. C. Nemat-Nasser, and S. Schultz, "Composite medium with simultaneous negative permeability and permittivity," *Physical Review Letters*, vol. 84, no. 18, pp. 4184–4187, 2000.
- [8] N. Engheta and R. W. Ziolkowski, "A positive future for double-negative metamaterials," *IEEE Transactions on Microwave Theory and Techniques*, vol. 53, no. 4, pp. 1535–1556, 2005.
- [9] A. Alù, N. Engheta, A. Erentok, and R. W. Ziolkowski, "Single-negative, double-negative, and low-index metamaterials and their electromagnetic applications," *IEEE Antennas and Propagation Magazine*, vol. 49, no. 1, pp. 23–36, 2007.
- [10] N. Fang, H. Lee, C. Sun, and X. Zhang, "Sub-diffraction-limited optical imaging with a silver superlens," *Science*, vol. 308, no. 5721, pp. 534–537, 2005.
- [11] J. B. Pendry, D. Schurig, and D. R. Smith, "Controlling electromagnetic fields," *Science*, vol. 312, no. 5781, pp. 1780–1782, 2006.
- [12] C.-C. Chen and J. L. Volakis, "Bandwidth broadening of patch antennas using nonuniform substrates," *Microwave and Optical Technology Letters*, vol. 47, no. 5, pp. 421–423, 2005.
- [13] J. Zhu and G. V. Eleftheriades, "A compact transmission-line metamaterial antenna with extended bandwidth," *IEEE Antennas and Wireless Propagation Letters*, vol. 8, pp. 295–298, 2009.
- [14] B.-I. Wu, W. Wang, J. Pacheco Jr., X. Chen, T. M. Grzegorzczuk, and J. A. Kong, "A study of using metamaterials as antenna substrate to enhance gain," *Progress in Electromagnetics Research*, vol. 51, pp. 295–328, 2005.
- [15] B.-I. Wu, W. Wang, J. Pacheco et al., "Anisotropic metamaterials as antenna substrate to enhance directivity," *Microwave and Optical Technology Letters*, vol. 48, no. 4, pp. 680–683, 2006.

- [16] Z.-B. Weng, Y.-C. Jiao, G. Zhao, and F.-S. Zhang, "Design and experiment of one dimension and two dimension metamaterial structures for directive emission," *Progress in Electromagnetics Research*, vol. 70, pp. 199–209, 2007.
- [17] H. Xu, Z. Zhao, Y. Lv, C. Du, and X. Luo, "Metamaterial superstrate and electromagnetic band-gap substrate for high directive antenna," *International Journal of Infrared and Millimeter Waves*, vol. 29, no. 5, pp. 493–498, 2008.
- [18] N. Engheta and R. W. Ziolkowski, *Metamaterials: Physics and Engineering Explorations*, John Wiley & Sons, Hoboken, NJ, USA, 2006.
- [19] A. Erentok, P. L. Luljak, and R. W. Ziolkowski, "Characterization of a volumetric metamaterial realization of an artificial magnetic conductor for antenna applications," *IEEE Transactions on Antennas and Propagation*, vol. 53, no. 1, pp. 160–172, 2005.
- [20] J. F. Woodley, M. S. Wheeler, and M. Mojahedi, "Left-handed and right-handed metamaterials composed of split ring resonators and strip wires," *Physical Review E: Statistical, Nonlinear, and Soft Matter Physics*, vol. 71, no. 6, Article ID 066605, 2005.
- [21] A. Semichaevsky and A. Akyurtlu, "Homogenization of metamaterial-loaded substrates and superstrates for antennas," *Progress in Electromagnetics Research*, vol. 71, pp. 129–147, 2007.
- [22] R. Mittra, "A critical look at metamaterials for antenna-related applications," *Journal of Communications Technology and Electronics*, vol. 52, no. 9, pp. 972–978, 2007.
- [23] G. V. Eleftheriades and K. G. Balmain, *Negative-Refractive Metamaterials: Fundamental Principles and Applications*, John Wiley & Sons, Princeton, NJ, USA, 2005.
- [24] C. Caloz and T. Itoh, *Electromagnetic Metamaterials: Transmission Line Theory and Microwave Applications*, Wiley, Hoboken, NJ, USA, 2006.
- [25] G. V. Eleftheriades, A. K. Iyer, and P. C. Kremer, "Planar negative refractive index media using periodically L-C loaded transmission lines," *IEEE Transactions on Microwave Theory and Techniques*, vol. 50, no. 12, pp. 2702–2712, 2002.
- [26] G. V. Eleftheriades, O. Siddiqui, and A. K. Iyer, "Transmission line models for negative refractive index media and associated implementations without excess resonators," *IEEE Microwave and Wireless Components Letters*, vol. 13, no. 2, pp. 51–53, 2003.
- [27] A. Sanada, C. Caloz, and T. Itoh, "Planar distributed structures with negative refractive index," *IEEE Transactions on Microwave Theory and Techniques*, vol. 52, no. 4, pp. 1252–1263, 2004.
- [28] G. V. Eleftheriades, M. A. Antoniades, and F. Qureshi, "Antenna applications of negative-refractive-index transmission-line structures," *IET Microwaves, Antennas and Propagation*, vol. 1, no. 1, pp. 12–22, 2007.
- [29] L. Qiang, H.-M. Lu, W. Zhao, J.-K. Wang, and B. Liu, "Simplified extended composite right/left-handed transmission line structure for dual-band applications," *Progress in Electromagnetics Research Letters*, vol. 15, pp. 137–144, 2010.
- [30] Y. Dong and T. Itoh, "Metamaterial-based antennas," *Proceedings of the IEEE*, vol. 100, no. 7, pp. 2271–2285, 2012.
- [31] L.-W. Li, Y.-N. Li, T. S. Yeo, J. R. Mosig, and O. J. F. Martin, "A broadband and high-gain metamaterial microstrip antenna," *Applied Physics Letters*, vol. 96, no. 16, pp. 164101–164103, 2010.
- [32] C.-J. Lee, K. M. K. H. Leong, and T. Itoh, "Composite right/left-handed transmission line based compact resonant antennas for RF module integration," *IEEE Transactions on Antennas and Propagation*, vol. 54, no. 8, pp. 2283–2291, 2006.
- [33] M. A. Antoniades and G. V. Eleftheriades, "A folded-monopole model for electrically small NRI-TL metamaterial antennas," *IEEE Antennas and Wireless Propagation Letters*, vol. 7, pp. 425–428, 2008.
- [34] T. Jang, J. Choi, and S. Lim, "Compact coplanar waveguide (CPW)-fed zeroth-order resonant antennas with extended bandwidth and high efficiency on vialess single layer," *IEEE Transactions on Antennas and Propagation*, vol. 59, no. 2, pp. 363–372, 2011.
- [35] A. Alù, F. Bilotti, N. Engheta, and L. Vegni, "Subwavelength, compact, resonant patch antennas loaded with metamaterials," *IEEE Transactions on Antennas and Propagation*, vol. 55, no. 1, pp. 13–25, 2007.
- [36] R. W. Ziolkowski and A. Erentok, "Metamaterial-based efficient electrically small antennas," *IEEE Transactions on Antennas and Propagation*, vol. 54, no. 7, pp. 2113–2130, 2006.
- [37] K. B. Alici and E. Ozbay, "Electrically small split ring resonator antennas," *Journal of Applied Physics*, vol. 101, no. 8, Article ID 083104, 2007.
- [38] Y. Dong, H. Toyao, and T. Itoh, "Design and characterization of miniaturized patch antennas loaded with complementary split-ring resonators," *IEEE Transactions on Antennas and Propagation*, vol. 60, no. 2, pp. 772–785, 2012.
- [39] Y. Zhang, J. Von Hagen, M. Younis, C. Fischer, and W. Wiesbeck, "Planar artificial magnetic conductors and patch antennas," *IEEE Transactions on Antennas and Propagation*, vol. 51, no. 10 I, pp. 2704–2712, 2003.
- [40] H. Mosallaei and K. Sarabandi, "Antenna miniaturization and bandwidth enhancement using a reactive impedance substrate," *IEEE Transactions on Antennas and Propagation*, vol. 52, no. 9, pp. 2403–2414, 2004.
- [41] E. Sáenz, R. Gonzalo, I. Ederra, J. C. Vardaxoglou, and P. de Maagt, "Resonant meta-surface superstrate for single and multifrequency dipole antenna arrays," *IEEE Transactions on Antennas and Propagation*, vol. 56, no. 4, pp. 951–960, 2008.
- [42] F. Yang and Y. Rahmat-Samii, *Electromagnetic Band Gap Structures in Antenna Engineering*, Cambridge University Press, Cambridge, UK, 2008.
- [43] N. Matsunaga, A. Sanada, and H. Kubo, "Novel two-dimensional planar negative refractive index structure," *IEICE Transactions on Electronics*, vol. 89, no. 9, pp. 1276–1282, 2006.
- [44] H. Xiong, J.-S. Hong, and Y.-H. Peng, "Impedance bandwidth and gain improvement for microstrip antenna using metamaterials," *Radioengineering*, vol. 21, no. 4, pp. 993–998, 2012.

## Research Article

# Control of the Radiation Patterns Using Homogeneous and Isotropic Impedance Metasurface

Fan Yang,<sup>1</sup> Zhong Lei Mei,<sup>1</sup> and Tie Jun Cui<sup>2</sup>

<sup>1</sup>School of Information Science and Engineering, Lanzhou University, Lanzhou 730000, China

<sup>2</sup>State Key Laboratory of Millimetre Waves, School of Information Science and Engineering, Southeast University, Nanjing 210096, China

Correspondence should be addressed to Zhong Lei Mei; [meizl@lzu.edu.cn](mailto:meizl@lzu.edu.cn) and Tie Jun Cui; [tjcui@seu.edu.cn](mailto:tjcui@seu.edu.cn)

Received 27 September 2014; Revised 10 December 2014; Accepted 10 December 2014

Academic Editor: Sanming Hu

Copyright © 2015 Fan Yang et al. This is an open access article distributed under the Creative Commons Attribution License, which permits unrestricted use, distribution, and reproduction in any medium, provided the original work is properly cited.

We propose to control the radiation patterns of a two-dimensional (2D) point source by using impedance metasurfaces. We show that the radiation patterns can be manipulated by altering the surface impedance of the metasurface. Full-wave simulation results are provided to validate the theoretical derivations. The proposed design enjoys novel properties of isotropy, homogeneity, low profile, and high selectivity of frequency, making it potentially applicable in many applications. We also point out that this design can be implemented with active metasurfaces and the surface impedance can be tuned by modulating the value of loaded elements, like resistors, inductors, and capacitors.

Recently, the concept of metasurface has been very hot. It is two-dimensional metamaterial rather than the previously proposed bulk metamaterials. Also, it enjoys the properties of low profile and low loss, making it very flexible and easy to implement in the real applications [1–5]. Metasurface can be considered as a patterned thin metallic film, whose electromagnetic behavior may be effectively described by averaged surface impedance [6]. This kind of impedance metasurface has various engineering applications [7]. In 2009, Alù proposed that the impedance surface could be used in the cloaking techniques and gave the name “mantle cloak” [8]. It is ultrathin and can be fabricated easily by printing designed metallic patterns [9]. Later, Zhu et al. successfully realized a metasurface with 360-degree reflection phase turning by controlling the surface impedance [10].

The impedance metasurface also has various applications in the field of antenna. Oliner and Hessel first put forward the comprehensive analysis of propagation of leaky waves on impedance surface [11]. Using this theory, Fong et al. suggested a two-dimensional holographic antenna [12]. This surface can scatter a known input wave and transform it into a desired output by varying the surface impedance. In 2012, the anisotropic impedance metasurface was suggested

to control the polarization of the radiated field [13]. More recently, impedance surface was also employed in the three-dimensional form [14]. And Hunt et al. extended this surface to microwave imaging by designing far-field radiation mode [15]. These designs of radiation pattern require inhomogeneous or even anisotropic surface impedance, which makes it difficult to implement compared with homogeneous and isotropic one. Here, we exploit the homogeneous and isotropic surface impedance in the control of a radiation pattern. The fact that mantle cloak enjoys many scattering modes motivates us to control the radiation pattern by magnifying a specific mode.

In this work, we propose a very simple model, in which a metasurface radiates under the excitation of a 2D point source (or a line source). With proper design of surface impedance of the metasurface, a specific pattern can be magnified and becomes dominant in the total field; hence, the model behaves like the radiation of this pattern. Moreover, the radiation pattern can be manipulated by employing different surface impedances. To demonstrate the validity of the theory, full-wave simulation results are given, including those mimicking the radiations of monopole, dipole, and quadrupole. In order to demonstrate the flexibility of our design,

the simulation for two metasurfaces is also made. These simulation results agree very well with the theoretical calculations. Throughout the paper, a time-harmonic factor  $e^{j\omega t}$  has been used.

Let us first consider a cylindrical metasurface in free space. A 2D point source (i.e., a line source) is placed near the metasurface, as shown in Figure 1(a). In this situation, the cylindrical metasurface is radiating under the excitation of the line source. The corresponding 2D geometry is illustrated in Figure 1(b), in which  $a$  represents the radius of the cylinder, and  $I$  represents the current of line source. In analyzing the problem, we set up a cylindrical coordinate system, where the axis of the cylindrical metasurface coincides with the  $z$ -axis. The coordinate center is set at the center of the metasurface and the coordinates of the line source are  $(\rho', \varphi')$ . Then the incident electric field  $E^i$  can be written as

$$\begin{aligned} E^i &= E_z^i \\ &= -\frac{\omega\mu_0 I}{4} H_0^{(2)}(k_0 |\vec{r} - \vec{r}'|) \\ &= -\frac{\omega\mu_0 I_0}{4} \\ &\quad \times \begin{cases} \sum_{n=-\infty}^{\infty} A_s H_n^{(2)}(k_0 \rho') J_n(k_0 \rho) e^{jn(\varphi - \varphi')} & \rho \leq \rho' \\ \sum_{n=-\infty}^{\infty} A_s J_n(k_0 \rho') H_n^{(2)}(k_0 \rho) e^{jn(\varphi - \varphi')} & \rho \geq \rho', \end{cases} \end{aligned} \quad (1)$$

in which  $I = A_s I_0$ ,  $k_0$  is the wave number in free space and  $J_n(\cdot)$  and  $H_n^{(2)}(\cdot)$  are cylindrical Bessel function and Hankel

function of the second kind, respectively. In our analysis, the excitation is a line source with infinite length, making the electric field parallel to the  $z$ -axis.

In the presence of the metasurface, the induced scattered field  $E_z^s$  and  $H_\varphi^s$  in the interior and exterior regions of metasurface are expressed as

$$\begin{aligned} E_z^s &= -\frac{\omega\mu_0 I_0}{4} \begin{cases} \sum_{n=-\infty}^{\infty} a_n J_n(k_0 \rho) e^{jn\varphi} & \rho \leq a \\ \sum_{n=-\infty}^{\infty} s_n H_n^{(2)}(k_0 \rho) e^{jn\varphi} & \rho \geq a, \end{cases} \quad (2) \\ H_\varphi^s &= -\frac{\omega\mu_0 I_0}{4} \cdot \frac{k_0}{j\omega\mu_0} \begin{cases} \sum_{n=-\infty}^{\infty} a_n [J_n(k_0 \rho)]' e^{jn\varphi} & \rho \leq a \\ \sum_{n=-\infty}^{\infty} s_n [H_n^{(2)}(k_0 \rho)]' e^{jn\varphi} & \rho \geq a, \end{cases} \quad (3) \end{aligned}$$

in which the common factors  $-\omega\mu_0 I_0/4$  in (1)–(3) are used in order to make the following expressions compact in form. Let us use the boundary condition [8]:

$$H_{\varphi|\rho=a^+} - H_{\varphi|\rho=a^-} = \frac{\hat{r} \times E_{z|\rho=a}}{Z_s}, \quad (4)$$

where  $Z_s$  denotes the surface impedance. It is obvious that  $Z_s = R_s + jX_s$ , in which  $R_s$  and  $X_s$  represent the resistance and reactance of surface impedance, respectively.

Using (1)–(4), we can easily derive the scattering coefficients as

$$\begin{aligned} s_n &= - \left| \frac{J_n(k_0 a)}{[J_n(k_0 a)]'} \frac{A_s H_n^{(2)}(k_0 \rho_s) J_n(k_0 a) e^{-jn\varphi_s}}{A_s H_n^{(2)}(k_0 \rho_s) [J_n(k_0 a)]' e^{-jn\varphi_s} - \frac{j\omega\mu_0}{k_0} \frac{A_s H_n^{(2)}(k_0 \rho_s) J_n(k_0 a) e^{-jn\varphi_s}}{Z_s}} \right| \\ &\quad \times \left| \frac{J_n(k_0 a)}{[J_n(k_0 a)]'} \frac{H_n^{(2)}(k_0 a)}{[H_n^{(2)}(k_0 a)]' - \frac{j\omega\mu_0}{k_0} \frac{H_n^{(2)}(k_0 a)}{Z_s}} \right|^{-1}. \end{aligned} \quad (5)$$

In order to magnify a specific pattern for radiations, the corresponding scattering coefficient is set to infinite, which can be easily achieved by setting the denominator of (5) to zero. This leads to the expression of the surface impedance as

$$Z_s = -\frac{\pi\omega\mu_0 a}{2} J_n(k_0 a) H_n^{(2)}(k_0 a), \quad (6)$$

which is used in the calculation of surface impedance for the corresponding radiation of a monopole, a dipole, a quadripole, and so forth. This is easily obtained by setting the order  $n$  in the above equation to 0, 1, 2, ..., respectively.

Using Huygens' principle, the electric field in the far-field region is calculated to determine the scattering width  $\sigma$ . Since

the problem in this work is 2D, we only need to figure out  $\sigma_{2D}$  [16], which is given as follows:

$$\begin{aligned} \sigma_{2D} &= \left( k_0 \left| \hat{r}_0 \times \oint_C [(\hat{n} \times \vec{E}_c) - \eta_0 \hat{r}_0 \times (\hat{n} \times \vec{H}_c)] \right. \right. \\ &\quad \left. \left. \times \exp(ik \vec{r}' \cdot \hat{r}_0) dl \right|^2 \right) \times \left( 4 \left| \vec{E} \right|^2 \right)^{-1}, \end{aligned} \quad (7)$$

where  $\vec{E}_c$  and  $\vec{H}_c$  are the EM field on the integration contour  $C$ ,  $\hat{r}_0$  is the unit vector of the scattering direction,  $\vec{r}'$  is the

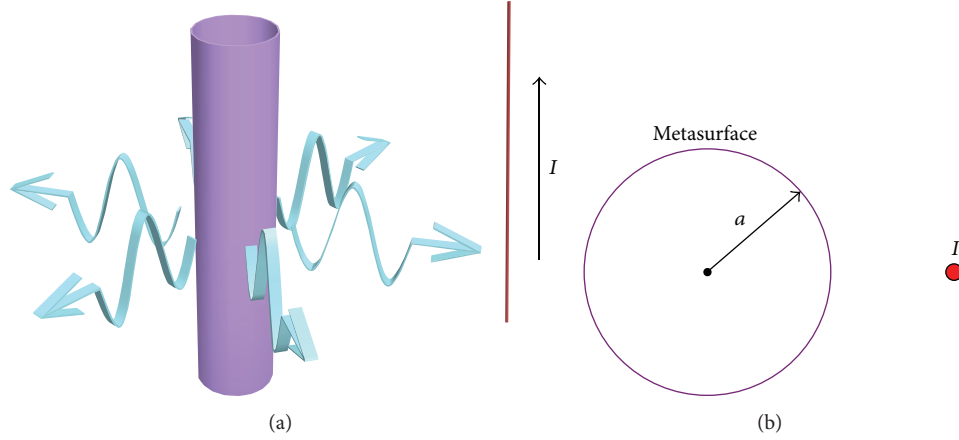


FIGURE 1: Principle of the proposed model with a cylindrical metasurface and a line source (color online). (a) The three-dimensional depiction. (b) The two-dimensional geometry of the cross section.

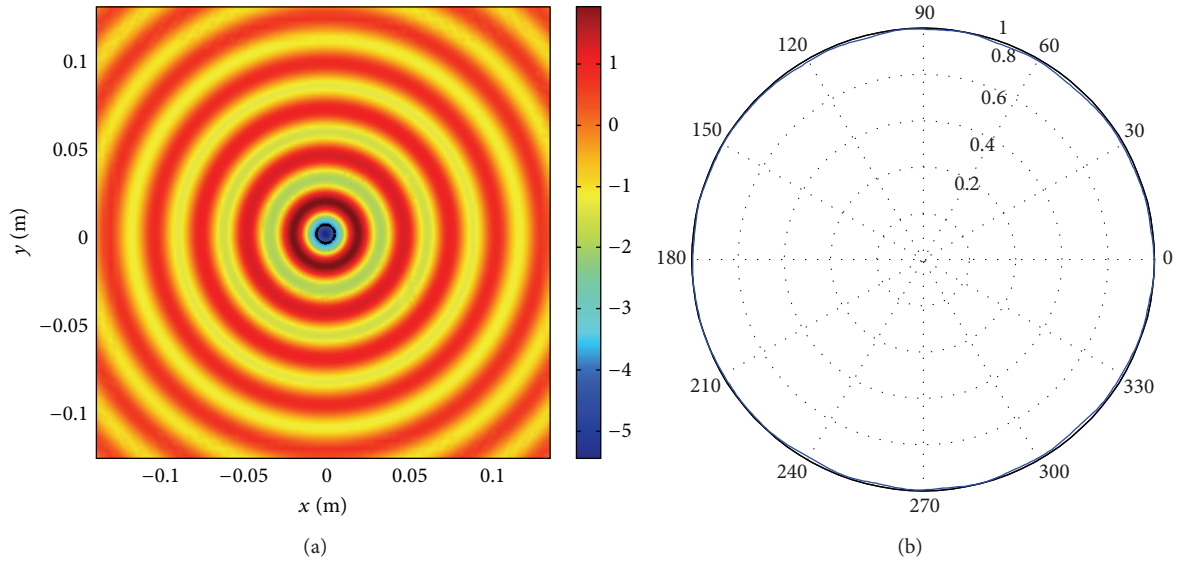


FIGURE 2: The simulation result of a monopole radiation (color online). (a) The electric field distribution in the  $x$ - $y$  plane. (b) The far-field radiation pattern with a circular shape.

position vector on the contour  $C$ , and  $\eta_0$  is the free space wave impedance. So we can calculate the radar cross section based on this equation. Note that the integration contour  $C$  can be chosen in near-field when there is no source in exterior region of this contour. To generally measure the overall scattering width versus frequency, the total scattering width is used [9, 17]:

$$\sigma_{\text{total}} = \frac{4}{k_0} \sum_{n=-\infty}^{n=\infty} |s_n|^2. \quad (8)$$

It is defined as the ratio of the energy across a closed surface that encloses the scatterer to the incident irradiance.

Next we perform full-wave simulations to verify the proposed theory, in which the working frequency is set as 10 GHz. Using (6), we first consider the case of a monopole radiation. In our simulation, the radius of the cylindrical

metasurface is set to  $\lambda_0/5$  ( $\lambda_0$  represents the wavelength in free space) and the polar coordinates of the excitation source  $(\rho_s, \varphi_s)$  are  $(\lambda_0, 0)$ . The values of  $I_0$  and  $A_s$  are both set as 1. The calculation result shows that the surface impedance for the monopole radiation is simply  $Z_s = (-307.2 + 125.3j) \Omega$ . Figure 2 demonstrates the simulation result of the monopole radiation, in which Figure 2(a) illustrates the electric field distribution in the  $x$ - $y$  plane. It is obvious that the scattered field by the metasurface looks like a monopole radiation. Moreover, it is clear that the incident field of line excitation becomes negligible when the monopole pattern is magnified.

In order to quantify our simulation result, the electric field on a centered circle with radius 0.1 m is extracted from the simulation result. Then the scattering width  $\sigma_{2D}$  is calculated using the proposed method, and the far-field radiation pattern is given in the polar diagram in Figure 2(b). Obviously, the radiation pattern is nearly a circle, which

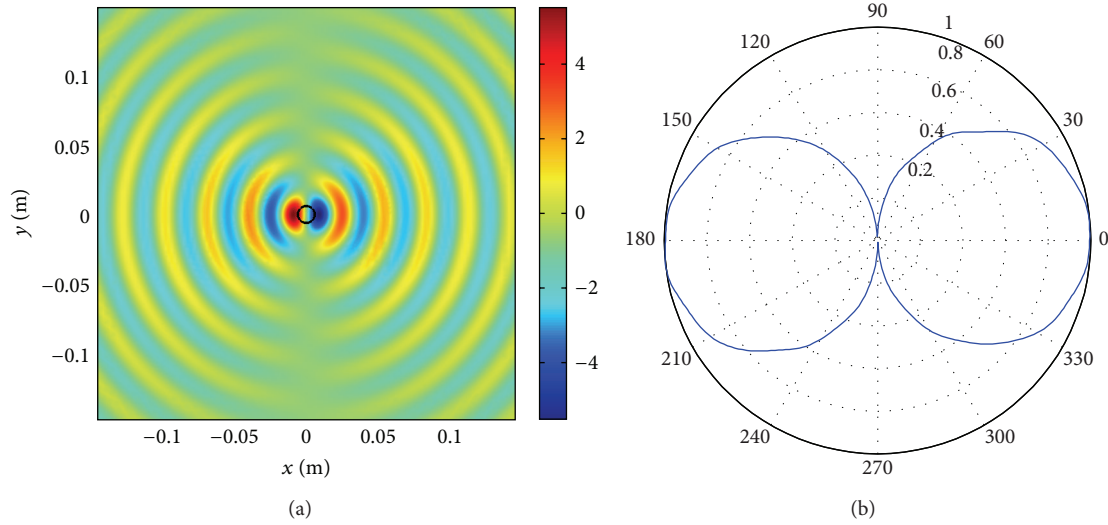


FIGURE 3: The simulation result for a dipole radiation (color online). (a) The electric field distribution in the  $x$ - $y$  plane. (b) The far-field radiation pattern with a “ $\infty$ ” shape.

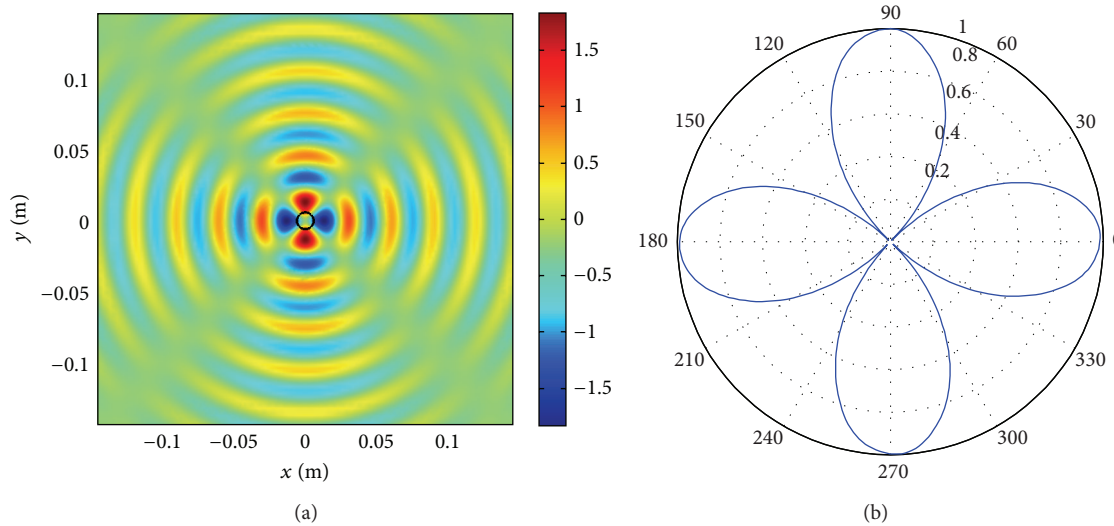


FIGURE 4: The simulation result of a quadrupole radiation (color online). (a) The electric field distribution in the  $x$ - $y$  plane. (b) The far-field radiation pattern with a petal shape.

quantitatively verifies the correctness of the theoretical analysis. Note that a little discrepancy exists in the far-field radiation pattern, which is due to some disturbance from the remaining patterns. However, these disturbances are ignorable when compared to the designed radiation pattern, making the metasurface behave like a monopole.

Then we choose  $n = 1$ , and the surface impedance of metasurface is calculated as  $Z_s = (-195.2 - 220.9j) \Omega$ , which corresponds to the case when the dipolar pattern is magnified. The performance for this metasurface is presented in Figure 3. Similarly, both the near electric field distribution and far-field radiation pattern are studied. The simulation result illustrated in Figure 3(a) shows that the radiation of this metasurface looks like a dipole, in which the excitation

source also becomes ignorable. The quantitative depiction of far-field radiation pattern is given in Figure 3(b). Note that the curve of radiation pattern is not a rigid “ $\infty$ ” shape because some other patterns have also been magnified, affecting the total radiation field. But these patterns are overwhelmed by the dominant dipole field, making the total radiation pattern behave like a dipole.

We continue to consider the case of quadrupole, and the corresponding value of surface impedance is obtained by setting  $n = 2$ , which yields  $Z_s = (-22.2 - 152.2j) \Omega$ . Figure 4 shows the simulation results of the quadrupole case, in which Figure 4(a) is the near-field distribution and Figure 4(b) gives the corresponding far-field radiation pattern. Through the change of surface impedance, the metasurface can truly

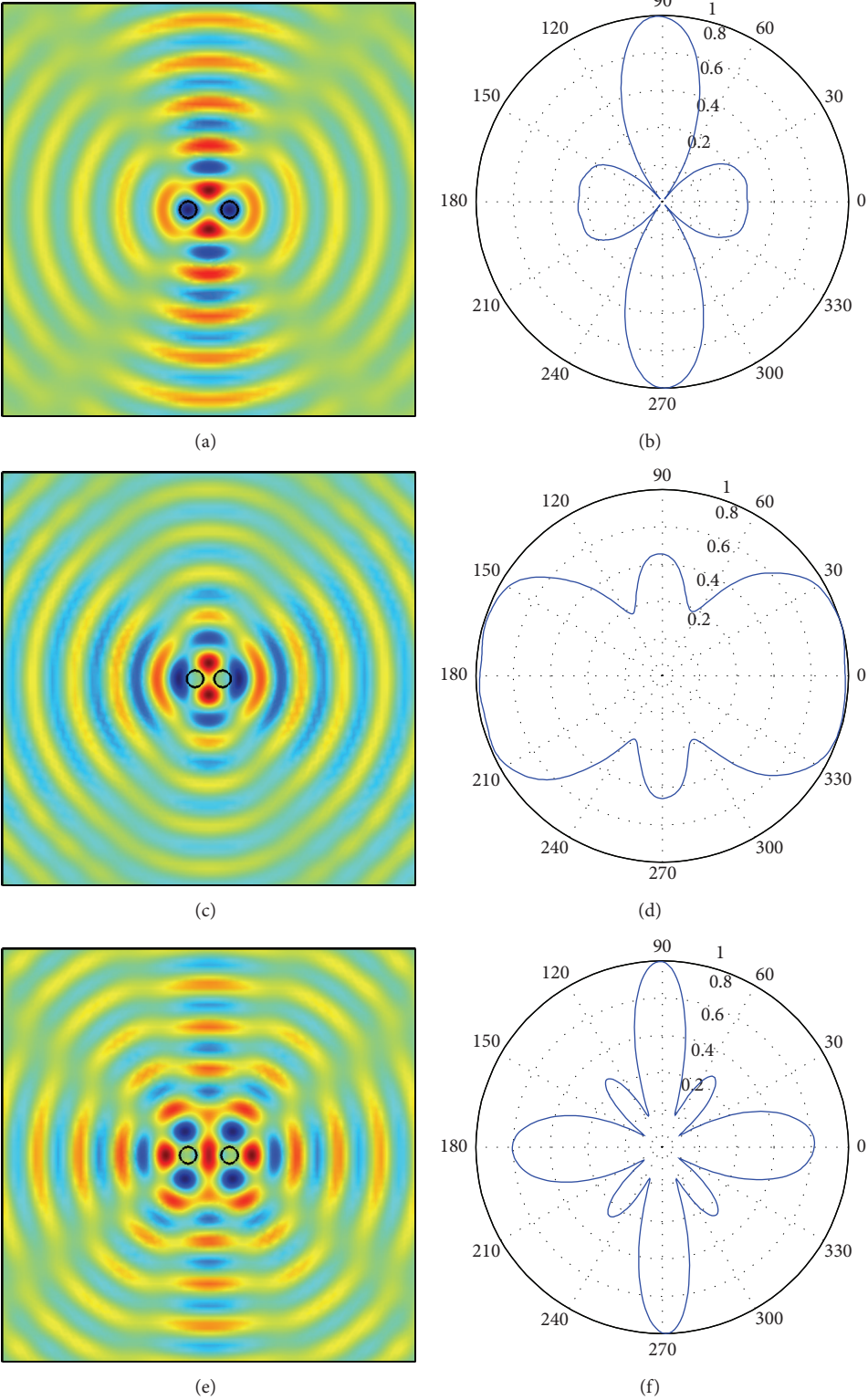


FIGURE 5: ((a), (c), and (e)) The electric field distribution in the  $x$ - $y$  plane, where mode  $n$  equals 0, 1, and 2, respectively (color online). ((b), (d), and (f)) The corresponding far-field radiation pattern of (a), (c), and (e).

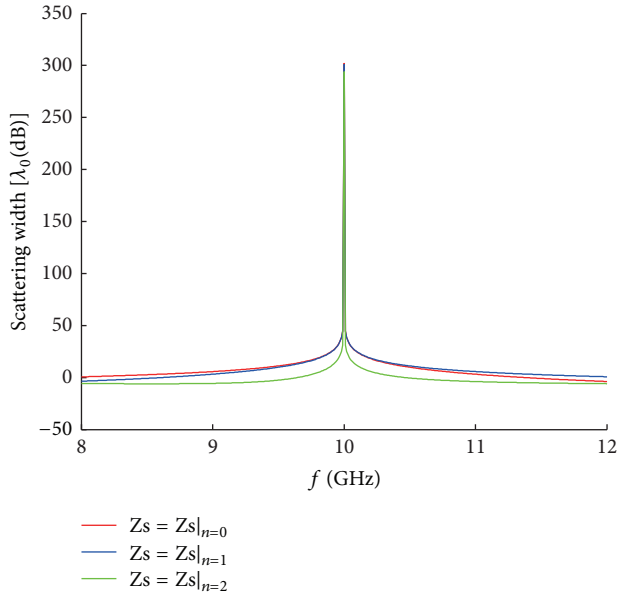


FIGURE 6: The total scattering widths versus frequency, in which different surface impedance is considered, including the corresponding monopole, the dipole, and the quadrupole cases (color online).

radiate like a quadrupole, whose far-field pattern has a typical petal shape.

Likewise, other radiation patterns, like sextupole and octupole radiations, can also be achieved by setting the order  $n$  to 3 and 4, respectively. And from the calculation results, we can easily reach the conclusion that the proposed metasurface is active due to the fact that surface resistance has a negative value.

However, the proposed metasurface can be regarded as a basic unit. And we can put several units to create many other kinds of radiation patterns. In the following part, the simulations of radiation pattern when there are two cylindrical metasurfaces with same parameters are given, in which three cases mean mode  $n$  equals 0, 1, and 2, respectively. The simulation results are shown in Figure 5. Additionally, more attainable radiation patterns can be realized by different combination of these units.

Using (8), the variations of total scattering widths versus frequency are calculated, as shown in Figure 6, including the cases of monopole, dipole, and quadrupole. This figure demonstrates that the scattering width is very sensitive to the deviation of frequency from 10 GHz. In other words, this metasurface is selective in scattering frequency, which can avoid the disturbance of other frequencies in the real applications.

Recently, active devices have been suggested to realize some negative electromagnetic parameters, which may not be attainable in nature. In our work, a negative resistor model was put forward to meet the negative conductivity requirement of an exterior cloak [18]. This model consists of a source and two resistors in order to make the input current have a negative linear relation with voltage. Also, loading of negative impedance converter (NIC) elements has been proposed as a

way to realize an active metasurface [19]. These loading elements can provide an effective negative capacitance. Based on these ideas, it can be expected that a metasurface with negative resistance can also be realized in a similar manner.

With regard to control of surface impedance, we point out that its value can be changed by modulating the parameter of some loaded elements, like resistors, inductors, or capacitors. For example, in Liu's work, the surface impedance is tuned by voltage-modulation of a varactor diode [20].

In summary, we have shown that a designed radiation pattern can be achieved by using a line source to excite a metasurface. By selecting proper surface impedance, the radiation pattern of total field can be a magnified monopole, dipole, quadrupole, and so forth. This makes it possible to build up a multipolar antenna system with the simple configuration. The most important property of the model is that its radiation pattern is controlled by simply changing the surface impedance rather than modifying the geometrical shape. And this surface impedance is homogeneous and isotropic in contrast with previous holographic impedance surface. Moreover, this model is ultrathin and selective in the radiation frequency.

## Conflict of Interests

The authors declare that there is no conflict of interests regarding the publication of this paper.

## Acknowledgments

This work was supported in part by National High Tech (863) Projects (Grants no. 2012AA030402 and 2011AA010202), in part by the 111 Project (111-2-05), and in part by the National Science Foundation of China (Grants no. 60990320 and 60990324). Zhong Lei Mei acknowledges the Open Research Funds of State Key Laboratory of Millimeter Waves (Grant no. K201409) and Fundamental Research Funds for the Central Universities (Grant nos. LZUJBKY-2013-k06, LZUJBKY-2014-43, and LZUJBKY-2014-237).

## References

- [1] N. Yu, P. Genevet, M. A. Kats et al., "Light propagation with phase discontinuities: Generalized laws of reflection and refraction," *Science*, vol. 334, no. 6054, pp. 333–337, 2011.
- [2] N. Yu, P. Genevet, F. Aieta et al., "Flat optics: controlling wavefronts with optical antenna metasurfaces," *IEEE Journal of Selected Topics in Quantum Electronics*, vol. 19, no. 3, Article ID 4700423, 2013.
- [3] C. L. Holloway, E. F. Kuester, J. A. Gordon, J. O'Hara, J. Booth, and D. R. Smith, "An overview of the theory and applications of metasurfaces: The two-dimensional equivalents of metamaterials," *IEEE Antennas and Propagation Magazine*, vol. 54, no. 2, pp. 10–35, 2012.
- [4] A. V. Kildishev, A. Boltasseva, and V. M. Shalaev, "Planar photonics with metasurfaces," *Science*, vol. 339, no. 6125, p. 1289, 2013.
- [5] N. Yu and F. Capasso, "Flat optics with designer metasurfaces," *Nature Materials*, vol. 13, no. 2, pp. 139–150, 2014.

- [6] S. Tretyakov, *Analytical Modeling in Applied Electromagnetics*, Artech House, Boston, Mass, USA, 2003.
- [7] B. A. Munk, *Frequency Selective Surface: Theory and Design*, John Wiley & Sons, New York, NY, USA, 2000.
- [8] A. Alù, "Mantle cloak: invisibility induced by a surface," *Physical Review B*, vol. 80, Article ID 245115, 2009.
- [9] P. Y. Chen and A. Alu, "Mantle cloaking using thin patterned metasurfaces," *Physical Review B*, vol. 84, Article ID 205110, 2011.
- [10] B. O. Zhu, J. M. Zhao, and Y. J. Feng, "Active impedance metasurface with full 360° reflection phase tuning," *Nature Scientific Reports*, vol. 3, article 3059, 2013.
- [11] A. Oliner and A. Hessel, "Guided waves on sinusoidally-modulated reactance surfaces," *IRE Transactions on Antennas and Propagation*, vol. 7, no. 5, pp. 201–208, 1959.
- [12] B. H. Fong, J. S. Colburn, J. J. Ottusch, J. L. Visher, and D. F. Sievenpiper, "Scalar and tensor holographic artificial impedance surfaces," *IEEE Transactions on Antennas and Propagation*, vol. 58, no. 10, pp. 3212–3221, 2010.
- [13] R. Quarfoth and D. Sievenpiper, "Broadband unit-cell design for highly anisotropic impedance surfaces," *IEEE Transactions on Antennas and Propagation*, vol. 62, no. 8, pp. 4143–4152, 2014.
- [14] D. J. Gregoire, "3-D conformal metasurfaces," *IEEE Antennas and Wireless Propagation Letters*, vol. 12, pp. 233–236, 2013.
- [15] J. Hunt, T. Driscoll, A. Mrozack et al., "Metamaterial apertures for computational imaging," *Science*, vol. 339, no. 6117, pp. 310–313, 2013.
- [16] C. Li and F. Li, "Two-dimensional electromagnetic cloaks with arbitrary geometries," *Optics Express*, vol. 16, no. 17, pp. 13414–13420, 2008.
- [17] C. F. Bohren and D. R. Huffman, *Absorption and Scattering of Light by Small Particles*, Wiley, New York, NY, USA, 1983.
- [18] F. Yang, Z. L. Mei, X. Y. Yang, T. Y. Jin, and T. J. Cui, "A negative conductivity material makes a dc invisibility cloak hide an object at a distance," *Advanced Functional Materials*, vol. 23, no. 35, pp. 4306–4310, 2013.
- [19] P. Y. Chen, C. Argyropoulos, and A. Alu, "Broadening the cloaking bandwidth with non-foster metasurfaces," *Physical Review Letters*, vol. 111, Article ID 233001, 2013.
- [20] S. Liu, H.-X. Xu, H. C. Zhang, and T. J. Cui, "Tunable ultrathin mantle cloak via varactor-diode-loaded metasurface," *Optics Express*, vol. 22, no. 11, Article ID 13403, 2014.

## Research Article

# Suppression of Specular Reflections by Metasurface with Engineered Nonuniform Distribution of Reflection Phase

Xin Mi Yang,<sup>1,2</sup> Ge Lan Jiang,<sup>1</sup> Xue Guan Liu,<sup>1</sup> and Cheng Xiang Weng<sup>3</sup>

<sup>1</sup>*School of Electronics and Information Engineering, Soochow University, Suzhou 215006, China*

<sup>2</sup>*State Key Laboratory of Millimeter Waves, Southeast University, Nanjing 210096, China*

<sup>3</sup>*Electronic Countermeasure Laboratory, Air Force Early Warning Academy, Wuhan 430019, China*

Correspondence should be addressed to Xin Mi Yang; [yangxinmi@suda.edu.cn](mailto:yangxinmi@suda.edu.cn)

Received 9 November 2014; Accepted 8 January 2015

Academic Editor: Sanming Hu

Copyright © 2015 Xin Mi Yang et al. This is an open access article distributed under the Creative Commons Attribution License, which permits unrestricted use, distribution, and reproduction in any medium, provided the original work is properly cited.

We make preliminary investigations on a new approach to reducing radar cross section (RCS) of conducting objects. This approach employs novel planar metasurfaces characterizing nonuniform distribution of reflection phase. The operation principle of this approach and the design rule of the associated metasurfaces are explained using a simplified theoretical model. We then present a design example of such metasurfaces, in which three-layer stacked square patches with variable sizes are utilized as the reflecting elements. The proposed RCS-reduction approach is verified by both numerical simulations and measurements on the example, under the assumption of normal plane wave incidence. It is observed that, in a fairly wide frequency band (from 3.6 to 5.5 GHz), the presented example is capable of suppressing the specular reflections of conducting plates significantly (by more than 7 dB) for two orthogonal incident polarizations.

## 1. Introduction

Reduction of target radar cross section (RCS) for military or civilian applications has been a subject of extensive studies in both scientific and engineering communities for decades. The existing RCS-reduction strategies can be classified into two categories. One is decreasing or even canceling the scattered energy and the other is reshaping the scattering pattern. Traditionally, the radar absorbing material (RAM) is adopted for the first category while the second category is usually achieved through shaping of target [1–4]. Recently, great efforts have been made for the sake of improving the traditional RAM technology. For instance, reduced RAM thickness has been achieved by employing artificial magnetic conductor (AMC) or reactive impedance ground as the backing panel of RAM [5–7]. It is worth mentioning that the rapidly growing research field of metamaterials has contributed a completely new strategy called invisibility cloak [8, 9], which can be grouped into the first category. The invisibility cloak is a kind of inhomogeneous wrappage that could steer the incoming electromagnetic waves smoothly

around the hidden object and return them to their original trajectory, making the object almost invisible (i.e., have no scattered field). New ideas have emerged regarding the second category of RCS-reduction techniques these years as well [10–14]. For example, it was proposed by Paquay et al. that, by combining AMC and perfect electrical conductor (PEC) cells in a chessboard-like configuration, the cancelation of reflections from these two kinds of cells would effectively reduce the specular reflections and hence the RCS of planar conducting plate [10]. In addition, some researchers have paid attention to metamaterial coatings with randomly distributed refractive indices or gradients of refractive index [11–13]. Such coatings are capable of suppressing remarkable lobes of conducting plates by creating diffuse reflections in front of these plates. In 2014, Wang et al. proposed a design of broadband and broad-angle low-scattering metasurface based on a hybrid optimization algorithm [14].

In this paper, we make further investigations on RCS-reduction schemes characterizing redistribution of scattered energy, by making use of novel metasurfaces with nonuniformly distributed reflection phase. The rest of

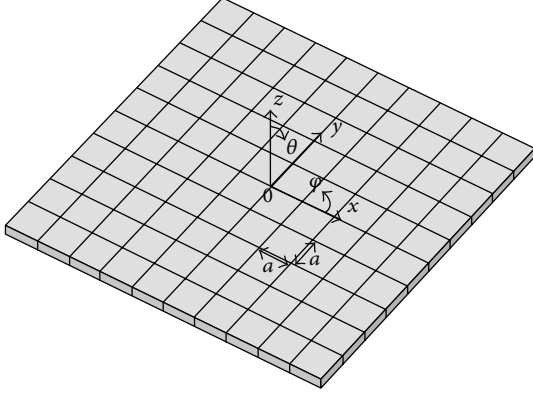


FIGURE 1: Sketch plot of a planar metasurface consists of  $N_x \times N_y$  reflecting elements in square lattice.

the paper is organized as follows. In Section 2, a theoretical model for analyzing the backscattering performance of such metasurfaces is given and a fundamental design rule of the relevant nonuniform distribution of reflection phase is promoted for RCS-reduction in the specular direction. Section 3 introduces a practical implementation scheme of such metasurfaces through an example. Finally, Section 4 presents both the simulation and measurement results of the example, which confirms that metasurfaces with properly designed nonuniform phase distribution have the potential of suppressing specular reflections of planar conducting plates under normal incidence.

## 2. Theory

Metasurface with nonuniformly distributed reflection phase, which is referred to as nonuniform surface below for brevity, is artificial composite constituted by reflecting elements each of which reflects local incident ray back into space with certain phase shift. One or several geometrical parameters of these elements vary along the surface such that the reflection phase is nonuniformly distributed with respect to incident plane waves.

It is well known that directive radiation is closely related to equiphase surface perpendicular to the radiation direction. For planar conducting plate which has uniform reflection phase, the reflected field possesses a planar equiphase surface with respect to incident plane wave and hence the reflected energy is focused in specific direction (i.e., the specular direction). If the conducting plate is covered with certain composite structure to form a nonuniform surface, the equiphase surface will be no doubt disturbed and the incident plane wave will be reflected or scattered irregularly. Moreover, it is possible that the directional reradiation in the specular direction is remarkably suppressed or even eliminated, provided that the distribution of reflection phase is appropriately chosen.

For simplicity, consider the problem geometry shown in Figure 1, where a planar nonuniform surface is divided into  $N_x \times N_y$  squares with lattice constant denoted by  $a$ . Each square represents a reflecting element which is assumed to

totally reflect its local incident beam. The origin of coordinate is situated at the center of the plane defined by the surface. An infinite  $y$ -polarized plane wave is normally incident on the nonuniform surface and is given by

$$\vec{E}_I = \dot{E}_I e^{jk_0 z} \hat{y}, \quad (1)$$

where  $k_0$  is the wave number in free space. The local reflected field at each element can be estimated using the infinitely periodic array model and is supposed to be dominated by the fundamental copolarized Floquet mode (in this model, each element is analyzed by assuming local periodicity; i.e., each element is considered in an array environment with all the elements identical). Hence, the reflected electric field at the element numbered as  $(l, s)$  ( $l = 0, 1, 2, \dots, N_x - 1$ ,  $s = 0, 1, 2, \dots, N_y - 1$ ) can be written as

$$\vec{E}_R(l, s) = \dot{E}_I e^{j\phi(l, s)} e^{-jk_0 z} \hat{y}, \quad (2)$$

where  $\phi(l, s)$  is the reflection phase of the corresponding element. By applying the second principle of equivalence, the angular spectrum of plane waves for scattered field in the half-space  $z > 0$  can be expressed by the following Fourier transform [15]:

$$\tilde{E}_{Ry}(u, v) = \int_{-\infty}^{\infty} \int_{-\infty}^{\infty} \dot{E}_{Ry}(x, y) e^{jk_0(u x + v y)} dx dy, \quad (3)$$

where  $\dot{E}_{Ry}(x, y)$  is the tangential component of the scattered electric field along the surface (i.e., the plane of  $z = 0$ ) and  $u, v$  are variables related to the spherical coordinates  $(\theta, \varphi)$  by  $u = \sin \theta \cos \varphi$  and  $v = \sin \theta \sin \varphi$ . Note that the double integral in (3) is limited in the region of metasurface, because  $\dot{E}_{Ry}(x, y)$  is assumed to be zero outside of the surface. This assumption implies that the edge diffraction is ignored. Associating  $\dot{E}_{Ry}(x, y)$  with (2), the spectral function  $\tilde{E}_{Ry}(u, v)$  is further derived as

$$\tilde{E}_{Ry}(u, v) = a^2 K S \cdot \sum_{s=0}^{N_y-1} \sum_{l=0}^{N_x-1} \dot{E}_I e^{j\phi(l, s)} e^{jk_0 a(u l + v s)}. \quad (4)$$

In the above formula,

$$K = e^{-j(k_0 a/2)[u(N_x-1) + v(N_y-1)]}, \quad (5)$$

$$S = \text{Sa}\left(\frac{k_0 u a}{2}\right) \cdot \text{Sa}\left(\frac{k_0 v a}{2}\right), \quad (6)$$

where  $\text{Sa}(x) = \sin(x)/x$ , representing sample function.

For planar PEC plate with the same overall size,  $\phi(l, s)$  should be replaced by  $\pi$  and (5) is reduced to

$$\tilde{E}_{Ry}(u, v) = -a^2 K S \cdot \sum_{s=0}^{N_y-1} \sum_{l=0}^{N_x-1} \dot{E}_I e^{jk_0 a(u l + v s)}. \quad (7)$$

Obviously, the backscattering of PEC plate in the specular direction (i.e.,  $\theta = 0$ ) would be effectively suppressed (by no less than 10 dB) as long as the nonuniform distribution of

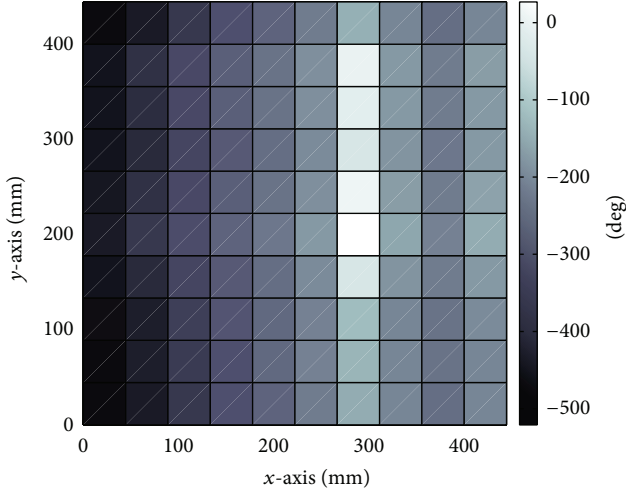


FIGURE 2: An instance of two-dimensional nonuniform distribution of reflection phase in degree, which is expected to significantly reduce the specular reflection of planar conducting plates.

reflection phase  $\phi(l, s)$  satisfies the relation expressed by the following inequation:

$$\left| \sum_{s=0}^{N_y-1} \sum_{l=0}^{N_x-1} e^{j\phi(l,s)} \right| \leq \sqrt{0.1} \cdot N_x N_y. \quad (8)$$

Such a conclusion is in accordance with the antenna array theory and similar conclusions could be drawn for the cases of off-normal incidence.

As an example, consider a planar nonuniform surface containing  $10 \times 10$  reflecting elements. It has the two-dimensional phase distribution as shown in Figure 2. This distribution is generated by randomly selecting phases in the range  $[-504 \text{ deg}, 40 \text{ deg}]$ . With such a distribution, the amplitude of the double summation in (8) is calculated to be 23.15, which is much smaller than  $N_x N_y = 100$ . According to the theoretical model presented above, the intensity of specular far-field scattering of the designed metasurface is 12.77 dB lower than that of naked conducting surface with the same overall size, when both surfaces are illuminated by  $x$ - or  $y$ -polarized normally incident plane waves. We remark that the choice of the distribution in Figure 2 is rather arbitrary. In fact, the condition indicated by (8) is very weak and there are numerous possibilities for reflection-phase distributions which meet this condition. Therefore, wideband performance is in prospect even though the phase distribution varies violently in band. This is beneficial when broadband RCS-reduction behavior is required, since the phase distribution of realistic nonuniform surface is usually frequency-dependent, as will be shown in the next section.

### 3. Implementation of Nonuniform Surface

Various radiators can be used as the reflecting elements of nonuniform surfaces. In particular, microstrip radiators such as metallic patches, dipoles, and loops are suitable for circumstances where conformality and compactness are

required [16–19]. Figure 3 demonstrates a typical reflecting element in microstrip form, which characterizes three-layer stacked square patches of variable size. The stacked-patch element occupies an  $a \times a$  square area in the  $x$ - $y$  plane and is backed with a conducting ground. The side lengths of patches on the bottom, middle, and top layers are denoted by  $d$ ,  $r_1 d$ , and  $r_2 d$ , respectively, where  $r_1$  and  $r_2$  are proportional factors with  $r_2 < r_1 < 1$ . Each of the three patches is supported by a piece of thin dielectric substrate which is also  $a \times a$  in size. The patch thickness and substrate thickness for each layer are represented by  $t_m$  and  $t_s$ , respectively. Moreover, Figure 3(b) indicates that every two neighboring layers (including the ground layer and the three patch layers) are separated by air, with the separation distances denoted by  $h_i$  ( $i = 1, 2, 3$ ).

As is well known, the microstrip patch over a ground plane response resonantly to incident plane waves, leading to sensitive reflection phase with respect to frequency variations near resonance. The resonant frequency mainly depends on the side length of patch and the reflection phase within certain frequency band can be effectively tuned by varying the side length. By stacking multiple patches, a multiresonant behavior is obtained and the tuning range of reflection phase can be expanded greatly [20, 21]. Moreover, stacking multiple patches is also helpful in enlarging the frequency band with linear response of reflection phase, which is critical in increasing the operational bandwidth of the nonuniform surface. The air separation employed under each patch layer further broadens the frequency band with sufficiently large tuning range of phase and results in a smoother and more linear phase variation versus side length  $d$ .

As an example, a parametric study has been made on the three-layer stacked-patch element with certain specifications. Each patch layer of the element under study is fabricated from F4B copper-clad laminate with copper thickness of  $t_m = 0.035$  mm, substrate thickness of  $t_s = 0.43$  mm, and dielectric constant of  $2.65 - j0.0053$ . The element size, the relative sizes of the stacked patches, and the air separations are considered fixed ( $a = 45$  mm,  $r_1 = 0.68$ ,  $r_2 = 0.5$ , and  $h_1 = h_2 = h_3 = 4$  mm) and only the side length of bottom patch  $d$  is the independently tunable variable. The parametric study is performed via numerical simulations using the commercial electromagnetic solver, CST Microwave Studio (MWS). Figure 3(c) shows the relation curve of simulated reflection phase at 4 GHz against the dimension  $d$  for the relevant stacked-patch elements. The reflection phase is associated with the fundamental copolarized Floquet mode with respect to normally incident plane waves polarized along the  $x$ - (or  $y$ -) axis, when periodic boundary conditions (PBCs) are assumed around the element in both the  $x$  and  $y$  directions. The reference plane just overlaps with the plane of top patch. It is seen from Figure 3(c) that the tuning range of reflection phase at 4 GHz is greater than  $500^\circ$ .

Figure 4 illustrates a realistic nonuniform surface formed by arranging the three-layer stacked-patch elements in  $a \times a$  square lattice. It is consistent with the model shown in Figure 1. The nonuniform distribution of reflection phase is achieved by varying the dimension  $d$  and keeping all the other parameters (i.e.,  $t_s$ ,  $t_m$ ,  $r_1$ ,  $r_2$ , and  $h_i$ ) constant in the surface. We remark that the structure in Figure 4 is quite similar to

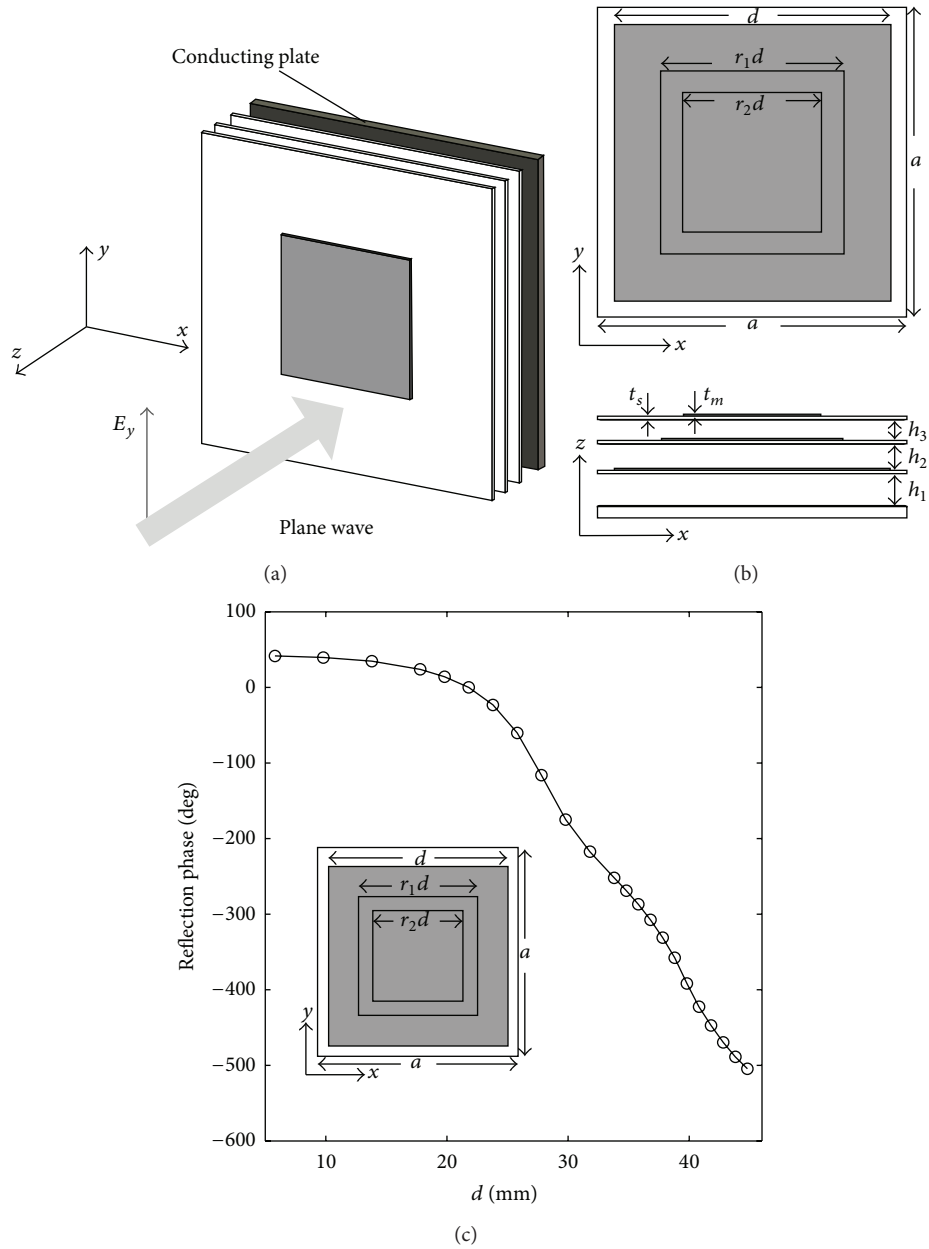


FIGURE 3: Reflecting element characterizing three-layer stacked square patches of variable size. (a) Oblique view. (b) Elevation view and side view. In the elevation view, the second and third substrate layers are omitted to show all the three patch layers clearly. (c) Typical design curve relating reflection phase at 4 GHz with the dimension  $d$  for the stacked-patch elements with certain specifications.

that of microstrip reflectarray [19]. However, the traditional reflectarray should be excited by certain feed antenna and is designed to produce directional reradiation, while the nonuniform surface proposed here has no feed antenna and is designed to destroy the directional reflection with respect to incoming plane waves.

An instance of nonuniform surface based on the stacked-patch elements has been designed and the corresponding fabricated sample is shown in Figure 5(a). This instance comprises  $10 \times 10$  elements, which are characterized by the specifications mentioned above. Hence, the total thickness

(from the top patch to the ground plane) of the instance is about 13.3 mm. The instance was designed to possess the two-dimensional phase distribution shown in Figure 2 at 4 GHz. Given this phase distribution, the dimension  $d$  of all the constituent elements for the nonuniform surface was determined using the design curve shown in Figure 3(c). The final distribution of dimension  $d$  is shown in Figure 5(b). It should be remarked that the phase distribution here avoids drastic change of patch size between neighboring elements so that the periodic array model for element evaluation mentioned above maintains enough accuracy.

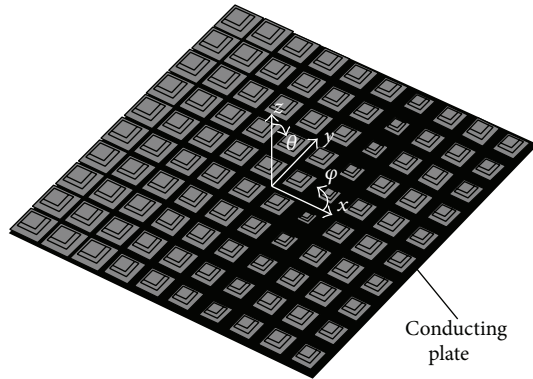
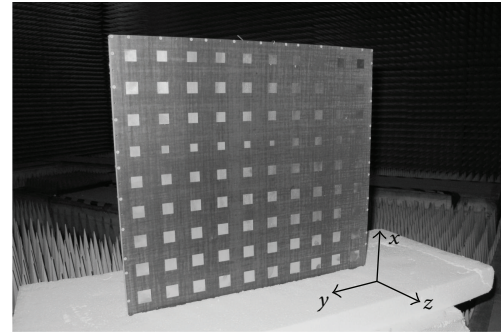


FIGURE 4: Nonuniform surface consisting of three layers of square patches with variable size above a conducting ground. All the substrate layers are set transparent so that the ground layer and the bottom and middle patch layers could be shown.

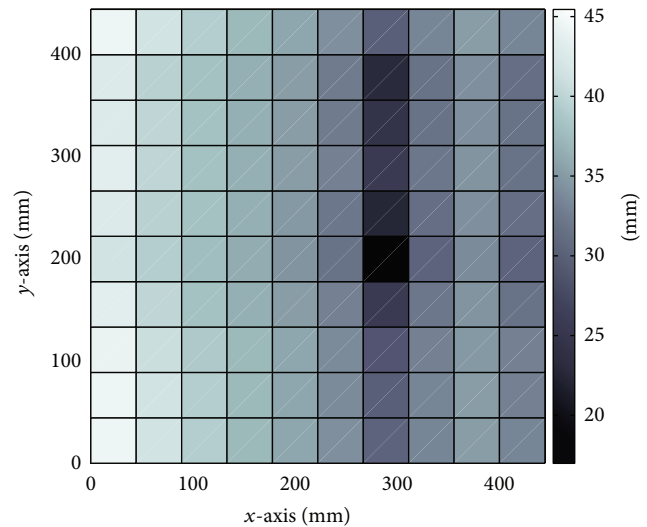
Due to the frequency-dependent phase response of the stacked-patch element, the phase distribution of the nonuniform surface changes with frequency. However, for our presented instance, the nonuniform feature of the phase distribution within a sufficiently large range remains over a fairly wide frequency band, that is, from about 3 GHz to 6 GHz. Figure 6 demonstrates the specular far-field reflectance for the instance in this band (circle). This reflectance curve, which assumes normal incidence and  $x$ - or  $y$ -polarization, is normalized to that of naked conducting surface and is calculated from the frequency-dependent phase distribution using the aforementioned theoretical model. Remarkable suppression of specular reflection throughout the band is observed from Figure 6.

#### 4. Simulation and Measurement Results

In order to verify the nondirectional reflection property of the nonuniform surface, full-wave simulations are conducted for the instance presented above, with the aid of CST MWS. Both the  $x$ - and  $y$ -polarized plane waves with normal incidence are considered in the simulations. For both polarizations, the simulated specular far-field reflectance curves, normalized to that of naked conducting surface, are also shown in Figure 6 (solid and dashed lines). As is expected, these two curves are in good consistency with the theoretical curve (circle). Figure 6 also indicates that the two simulated curves are slightly different from each other. This is because the nonuniform surface as instance has no rotational symmetry with respect to its central normal. Our theoretical model ignores this asymmetry and offers the same calculated reflectance results for both polarizations. However, such an ignorance or approximation does not prevent the model from providing us with acceptable predictions of backscattering performance of nonuniform surfaces. A further inspection on the simulated backscattering patterns of both the nonuniform surface and the naked conducting surface reveals that the suppression of specular reflections is achieved through unequally reallocating most of the scattered energy to various off-specular



(a)



(b)

FIGURE 5: (a) Photograph of a nonuniform surface sample composed of three-layer stacked-patch elements. Note that the bottom row of elements is buried in foams and can not be seen. (b) Two-dimensional distribution of dimension  $d$  for patches on the bottom layer (unit: millimeters).

directions in the  $z > 0$  half-space (i.e.,  $0 \leq \theta < 90$ ). As an example, Figure 7 compares the simulated backscattering patterns between the nonuniform surface and the naked conducting surface at 4 GHz for the  $y$ -polarized normal incidence.

Backscattering measurements have also been conducted concerning the nonuniform surface sample shown in Figure 5. The measurements consist of two stages which employ almost the same experimental setup. Figure 8 shows the experimental setup for the first stage, where a linearly polarized high-gain horn antenna is placed right in front of the nonuniform surface sample with a distance of 3 meters and the central normal of the sample surface is aligned with the symmetry axis of the horn aperture. The horn antenna is also connected to a single port of an Agilent N5230C vector network analyzer (VNA) through a flexible coaxial cable. The whole setup is situated in an anechoic chamber to minimize environmental interferences. During measurement, the VNA provides source microwave signals for the antenna and the main beam emitted from the horn antenna impinges on

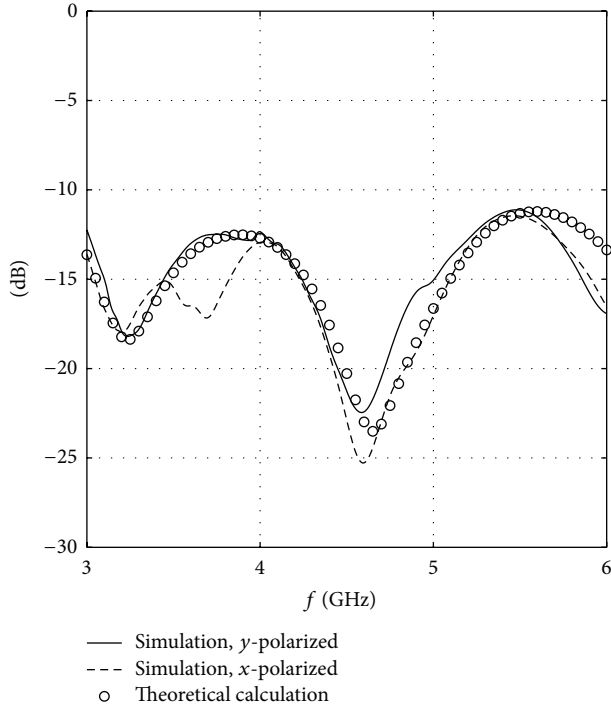


FIGURE 6: Theoretical and simulated results of the normalized specular far-field reflectance of the nonuniform surface as instance under normal incidence.

the sample surface. The back-scattered or reflected power from the sample is received by the same horn and then detected by the VNA. Note that the power reflected by the horn itself also enters the VNA in the meantime. By applying the gated-reflect-line (GRL) calibration technique provided by the time-domain analysis kit installed in the VNA, the influence of the power reflected by the horn is removed and the resultant reflection coefficient data read from the VNA is only related to the reflection from the sample. Two cases of incident beams are considered in the first stage. For the first case, the horn is arranged to allow a  $y$ -polarized incident beam with respect to the sample shown in Figure 5. By simply rotating the sample  $90^\circ$  around its central normal, the other case of incident beam with  $x$ -polarization can be achieved afterwards. The reflection coefficient data in decibels read from the VNA are recorded for both cases. As to the second stage of measurement, the nonuniform surface sample is replaced by an ordinary square metallic plate which possesses the same size as the sample. The reflection coefficient data in decibels given by the VNA at this stage is also recorded. The specular reflectance of the nonuniform surface sample normalized to that of the square metallic surface for both incident polarizations can then be obtained by subtracting the newly recorded data from those two sets of data measured at the first stage, respectively.

Figure 9 shows the experimental normalized specular reflectance of the nonuniform surface sample for both incident polarizations. It is observed that, in the presence of the sample, the directional specular reflection of the metallic

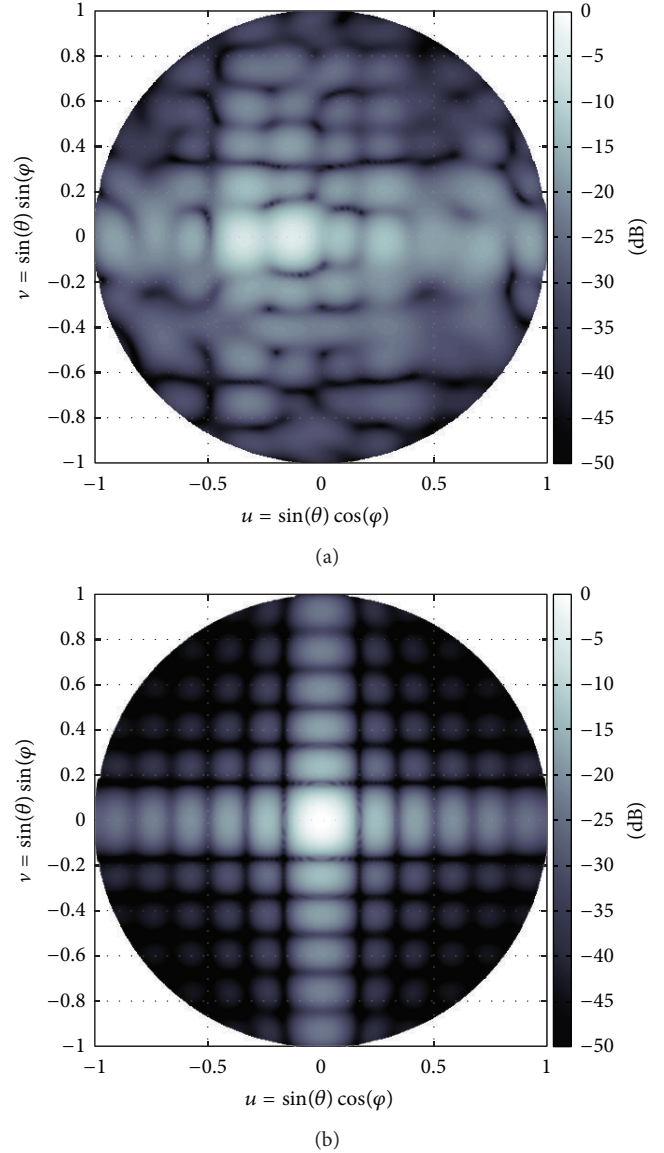


FIGURE 7: Simulated backscattering patterns under  $y$ -polarized normal incidence at 4 GHz for (a) the nonuniform surface as instance and (b) the naked conducting surface. The far-field intensity involved in this figure is the synthesized quantity  $\sqrt{|E_\theta|^2 + |E_\phi|^2}$ . Both patterns are normalized to the specular far-field intensity of the conducting surface and the values below  $-50$  dB have all been truncated.

surface in the band from 3.6 to 5.5 GHz is suppressed by more than 10 dB and 7 dB for the  $y$ - and  $x$ -polarized incident beams, respectively. Hence, the potential of the nonuniform surface to reduce RCS of conducting objects over a fairly wide frequency band is well demonstrated. The simulated reflectance is also shown in Figure 9 for comparison. We note that the measured reflectance minima appear at higher frequencies compared with their simulated counterparts. However, the measured and simulated reflectance curves are in qualitative agreement if we uniformly shift the measured curves towards lower frequency. The discrepancy between

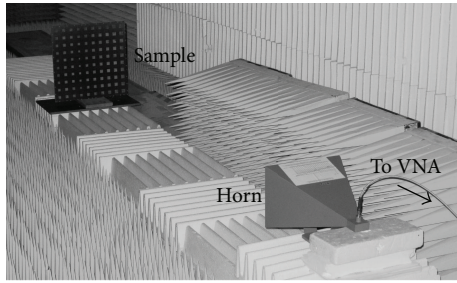


FIGURE 8: Experimental setup for measuring the specular reflectance of the nonuniform surface sample under normal incidence.

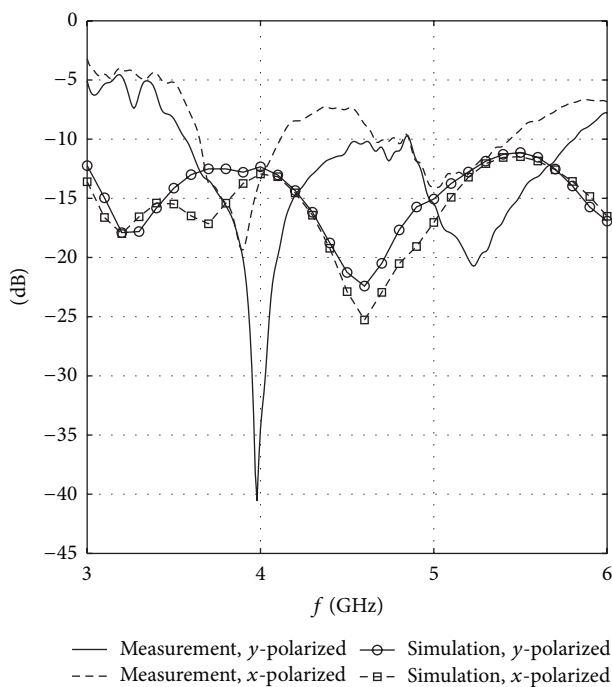


FIGURE 9: Experimental results of the normalized specular reflectance of the nonuniform surface sample with respect to both  $x$ - and  $y$ -polarized normally incident waves. The  $x$  and  $y$  directions are indicated by Figure 5(a).

the simulated and measured results is mainly attributed to the inaccuracy of the substrate permittivity, the fabrication and assembly error of the sample, and the differences between the experimental setup and the simulation configuration. In our experimental setup, the sample is in the radiating near-field (Fresnel) region of the horn antenna and the local incident rays for most of the reflecting elements are just roughly perpendicular to the element surface. In other words, the final experimental reflectance is not in a strict far-field sense and most of the reflecting elements underwent oblique incidence in the experiment. Because the first-order resonant frequency of metallic patch increases as the incidence angle grows, the effective operating band of the metasurface moved to higher frequency region in the experiment.

## 5. Conclusions

We have demonstrated that planar metasurface with nonuniformly distributed reflection phase, referred to as nonuniform surface, is capable of suppressing the specular reflections of conducting plates by scattering most incident energy in off-specular directions. A general condition under which the nonuniform surface could operate effectively has been derived using a simplified theoretical model. Based on this condition, an instance of nonuniform surface composed of three-layer stacked-patch elements has been designed. Both simulation and measurement results for the design example confirm that the nonuniform surface is an effective approach of RCS-reduction for conducting objects and has the potential of providing broadband performance.

## Conflict of Interests

The authors declare that there is no conflict of interests regarding the publication of this paper.

## Acknowledgments

This work was supported in part by the Natural Science Foundation of Jiangsu Province under Grant BK20130326, in part by the National Natural Science Foundation of China under Grant 61301076, in part by the Open Research Program of State Key Laboratory of Millimeter Waves in China under Grant K201417, and in part by the Natural Science Foundation of the Higher Education Institutions of Jiangsu Province under Grant 12KJB510030.

## References

- [1] W. W. Salisbury, "Absorbent body for electromagnetic waves," U. S. Patent 2 599 944, June 1952.
- [2] E. F. Knott, J. F. Shaeffer, and M. T. Tuley, *Radar Cross Section*, Artech House, London, UK, 1993.
- [3] Y. Z. Ruan, *Radar Cross Section and Stealth Technology*, National Defence Industry Press, Beijing, China, 1998.
- [4] J. A. Adam, "How to design an invisible aircraft," *IEEE Spectrum*, vol. 25, no. 4, pp. 26–31, 1988.
- [5] N. Engheta, "Thin absorbing screens using metamaterial surfaces," in *Proceedings of the IEEE Antennas and Propagation Society International Symposium*, vol. 2, pp. 392–395, 2002.
- [6] F. Costa and A. Monorchio, "Multiband electromagnetic wave absorber based on reactive impedance ground planes," *IET Microwaves, Antennas and Propagation*, vol. 4, no. 11, pp. 1720–1727, 2010.
- [7] F. Costa and A. Monorchio, "A frequency selective radome with wideband absorbing properties," *IEEE Transactions on Antennas and Propagation*, vol. 60, no. 6, pp. 2740–2747, 2012.
- [8] J. B. Pendry, D. Schurig, and D. R. Smith, "Controlling electromagnetic fields," *American Association for the Advancement of Science: Science*, vol. 312, no. 5781, pp. 1780–1782, 2006.
- [9] D. Schurig, J. J. Mock, B. J. Justice et al., "Metamaterial electromagnetic cloak at microwave frequencies," *Science*, vol. 314, no. 5801, pp. 977–980, 2006.
- [10] M. Paquay, J.-C. Iriarte, I. Ederra, R. Gonzalo, and P. de Maagt, "Thin AMC structure for radar cross-section reduction," *IEEE*

*Transactions on Antennas and Propagation*, vol. 55, no. 12, pp. 3630–3638, 2007.

- [11] R. Liu, C. Ji, J. J. Mock, T. J. Cui, and D. R. Smith, “Random gradient index metamaterials,” in *Proceedings of the International Workshop on Metamaterials*, pp. 248–250, 2008.
- [12] X. M. Yang, X. Y. Zhou, Q. Cheng, H. F. Ma, and T. J. Cui, “Diffuse reflections by randomly gradient index metamaterials,” *Optics Letters*, vol. 35, no. 6, pp. 808–810, 2010.
- [13] X. M. Yang, Q. Cheng, and T. J. Cui, “Research on the one-dimensional randomly gradient index coating,” in *Proceedings of the International Conference on Microwave and Millimeter Wave Technology (ICMMT ’10)*, pp. 1208–1211, Chengdu, China, May 2010.
- [14] K. Wang, J. Zhao, Q. Cheng, D. S. Dong, and T. J. Cui, “Broadband and broad-angle low-scattering metasurface based on hybrid optimization algorithm,” *Scientific Reports*, vol. 4, article 5935, 2014.
- [15] R. H. Clarke and J. Brown, *Diffraction Theory and Antennas*, Ellis Horwood, Chichester, UK, 1980.
- [16] C. S. Malagisi, “Microstrip disc element reflect array,” in *Proceedings of the Electronics and Aerospace Systems Convention (EASCON ’78)*, pp. 186–192, 1978.
- [17] J. P. Montgomery, “A microstrip reflectarray antenna element,” in *Proceedings of the Antenna Applications Symposium*, University of Illinois, Urbana, Ohio, USA, 1978.
- [18] D. M. Pozar and T. A. Metzler, “Analysis of a reflectarray antenna using microstrip patches of variable size,” *Electronics Letters*, vol. 29, no. 8, pp. 657–658, 1993.
- [19] J. Huang and J. A. Encinar, *Reflectarray Antennas*, John Wiley & Sons, Hoboken, NJ, USA, 2007.
- [20] J. A. Encinar, “Design of two-layer printed reflectarrays using patches of variable size,” *IEEE Transactions on Antennas and Propagation*, vol. 49, no. 10, pp. 1403–1410, 2001.
- [21] J. A. Encinar and J. A. Zornoza, “Broadband design of three-layer printed reflectarrays,” *IEEE Transactions on Antennas and Propagation*, vol. 51, no. 7, pp. 1662–1664, 2003.

## Research Article

# Design of a Compact and High Sensitivity Temperature Sensor Using Metamaterial

Sabah Zemouli,<sup>1</sup> Abdelhafid Chaabi,<sup>1</sup> and Houcine Sofiane Talbi<sup>2</sup>

<sup>1</sup>Laboratoire Hyperfréquence et Semiconducteur Université Constantine 1, BP 325, Route Ain El Bey, 25017 Constantine, Algeria

<sup>2</sup>Faculté de Médecine, Université de Batna, 05 avenue Chahid Boukhrouf, 05000 Batna, Algeria

Correspondence should be addressed to Sabah Zemouli; [sabahzemouli@gmail.com](mailto:sabahzemouli@gmail.com)

Received 9 October 2014; Revised 15 December 2014; Accepted 8 January 2015

Academic Editor: Yun-Gui Ma

Copyright © 2015 Sabah Zemouli et al. This is an open access article distributed under the Creative Commons Attribution License, which permits unrestricted use, distribution, and reproduction in any medium, provided the original work is properly cited.

The present paper aims at sensing the temperature. A sensor metamaterial consisting of two concentric metallic rings and a thin metallic wire deposited on the surface of BaTiO<sub>3</sub> substrate is reported. The use of BaTiO<sub>3</sub> makes the resonant frequency of the structure shift as the temperature varies and makes the sensor applicable in many fields of applications. Numerical simulations and theoretical results are presented and compared to each other; there was a good agreement between them. This sensor is smaller, easier to fabricate, and very sensitive to the changes in temperatures.

## 1. Introduction

In this decade, metamaterials (MTM) or left handed materials (LHM) have attracted much attention among researchers in the microwave communities because of their unusual properties, such as negative permittivity [1], negative permeability [2], and negative refractive index [3, 4]. These periodic materials are very useful for many fields of applications [5–7]. Recently, a great interest has been devoted to the application of metamaterials in sensing; hereafter, we have provided some researches in this concern. Ishimaru and his colleagues have studied a metamaterial based on surface plasmon resonance (SPR) sensors in GHz regime while the traditional SPR is usually operated in optical domain only [8]. Kabashin et al. in [9] have enhanced the SPR sensor's performances by using metamaterial. In [10], the authors have proposed a method of dielectric sensing using  $\epsilon$  near zero narrow waveguide channels. In [11], Ekmekci and his colleague have studied a double sided square SRR (split ring resonator) topology for multipurpose sensor operating in X band; this sensor exhibits a negative value of permeability for frequencies close to the magnetic resonance frequency of the SRR structure, whereas our suggested structure exhibits negative permittivity and negative permeability close to the magnetic resonance frequency of the structure; in addition and according to [12] circular SRR can present a higher quality factor compared to

square SRR. References [13, 14] have studied the application of a Terahertz metamaterial for chemical sensing and [15] have explained how metamaterials can offer solutions to overcome technical limitations of wireless sensors.

Metamaterials are better in sensing than the conventional resonators (e.g., spiral coils), because they are easy and rapid in detection [16–18] and they can exhibit a strong localization and enhancement of fields; that is, they can improve the sensor's selectivity and sensibility [19] due to the application of an axial time varying magnetic field parallel to the particle plane in the orthogonal direction to the splits which creates a huge electric field density localized between them and presents higher signal and higher dips in their transmission spectrum, which results in a high quality factor  $Q$  compared to the conventional RF (radio frequency) resonators. This enables us to make telemetric measurements and to observe the operating frequency relatively easier [20]. Another advantage of the gaps existence in the MTM structure is the production of an additional capacitive effect which exhibits a lower resonance frequency (hence avoid the background absorption of the structure) and results in higher shift of the operating frequency with the same applied load, leading to higher sensitivity. The use of Barium titanate dielectric that is very sensitive to the changes of temperature makes our sensor more sensitive.

The aim of this paper is to design a high sensitive and smaller electrical sensor of temperature based on metamaterial operating in GHz regime. The proposed structure consists of a combination of two concentric circular metallic rings opened in the opposite sides commonly called SRR and a thin metallic wire placed on a dielectric substrate. Because the resonant frequency of the MTM structure is very sensitive to the changes of the capacitive effects (since its fundamental resonance behavior can be modeled by an  $LC$  circuit [21]) which are basically dependent on the resonator's topology and the substrate's parameters (i.e., substrate's thickness and relative permittivity), we have proposed a structure with a varying dielectric characteristics substrate. When the temperature changes, the dielectric properties of the substrate of the MTM will change and this will affect the capacitance of the SRR and then a shift in the resonant frequency will appear; this will indicate the measured temperature.

In this work, we have designed the equivalent circuit model of the proposed structure and we have derived the relations of its coefficients of reflexion and transmission using the ABCD Matrix approach; then we have compared them to those resulting from the simulation. The results were very close. In this study the metamaterial sensor is smaller, is easier to fabricate, possesses higher sensitivity, and is useful in a wide range of applications. The mechanism behind this is the use of a varying dielectric characteristics substrate.

## 2. Design OF LHM

The MTM structure is composed of a combination of PEC (perfect electric conductor) circular SRR and thin wire placed on a dielectric substrate of 0.1 mm of thickness ( $t_d$ ); the length and width of this substrate are 2 mm and 2.5 mm, respectively. The external radius of the SRR is  $r_0 = 0.75$  mm, the width of the two rings is  $d = 0.18$  mm, the spacing between them is 0.24 mm, the split of the outer ring is 0.4 mm, the split of the inner ring is equal to 0.2 mm, and the thickness of the rings is  $t_m = 0.035$  mm; the wire has a 0.2 mm of width and 1.8 mm of length. The substrate of this model is the Barium titanate dielectric BaTiO<sub>3</sub> [22, 23] which is one of the best known and commonly used materials for electric ceramics due to its excellent dielectric, ferroelectric, and piezoelectric properties at and above room temperature. We have specially chosen this material because its relative permittivity has a big dependence with the temperature (see Figure 1) which can be tailored in a wide range of applications. Furthermore, this material is sintered at high temperatures. This allows an operation at very elevated temperatures. Figure 2 shows the proposed structure.

## 3. Simulation and Equivalent Circuit Model

The simulation of the MTM structure has been executed using the High Frequency Structure Simulator (HFSS) software. A perfect magnetic conductor (PMC) boundary condition was set along  $z$ -axis while the perfect electric conductor (PEC) boundary condition was set along  $y$ -axis. On the last two faces, we have set two ports rectangular waveguide for sensor measurements. The LHM structure was placed at the center of the waveguide.

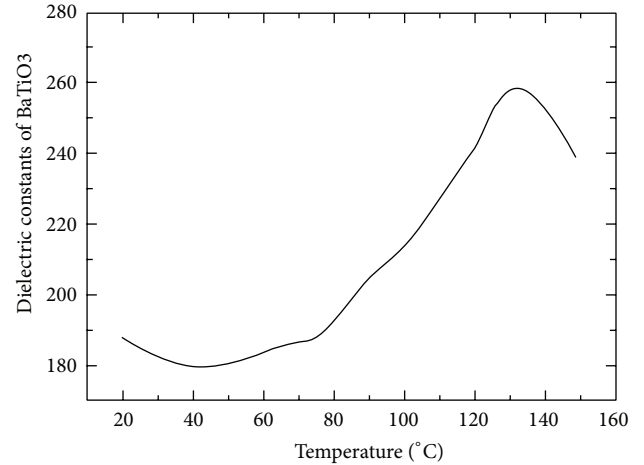


FIGURE 1: Variation of the dielectric constant of BaTiO<sub>3</sub> versus the temperature [22].

In Figure 3, we have studied the variation of the coefficient of the transmission  $S_{21}$  versus the variation of the frequency using the commercial simulator HFSS to study the shift in the resonant frequency according to the variation of the temperature of the sensor.

The effective permittivity of the LHM structure is different from the relative permittivity of the BaTiO<sub>3</sub> substrate ( $\epsilon_{\text{BaTiO}_3} \neq \epsilon_{\text{MTM structure}}$ ). We have calculated the effective permittivity  $\epsilon_{\text{eff}}$  and the effective permeability  $\mu_{\text{eff}}$  of the MTM structure using the Nicolson-Ross-Weir method [24]; the results are shown in Figure 4.

We notice that the resonant frequency of the simulated structure is 2.3 GHz with return loss of  $-20$  dB. The relative permittivity at this frequency is  $-12.19$ , whereas the relative permeability is  $-12.65$ .

**3.1. Study of the Effects of the Dielectric Substrate on the MTM Structure.** The resonant frequency of the MTM structure is inversely related to the total capacitance  $C_T$  of the sensor  $f = 1/2\pi\sqrt{L_T C_T}$  [21]; it is known that the capacitance is proportional to the dielectric constant  $C = \epsilon(l/S)$ , where  $S$  is area of a dielectric material,  $l$  is the thickness of a dielectric material, and  $\epsilon$  is dielectric material's permittivity.

When  $\epsilon$  increases, the capacitance of the sensor  $C_T$  increases which will decrease the resonant frequency. The shift in the resonant frequency resulting from the variation of the permittivity will indicate the variation in the temperature since the dielectric characteristics of the BaTiO<sub>3</sub> substrate are related to the temperature (see Figure 1).

When a time harmonic external magnetic field is applied along  $z$  axis of this structure, an electromotive force will create an induced current in the structure that will explain the inductive part of our system.

Because the LHM structure has a size much smaller than the operating wavelength, we can describe its electromagnetic characteristics by lumped circuit components capacitors and inductors. The overall structure can be represented by an  $LC$  circuit and the equivalent circuit model proposed for our

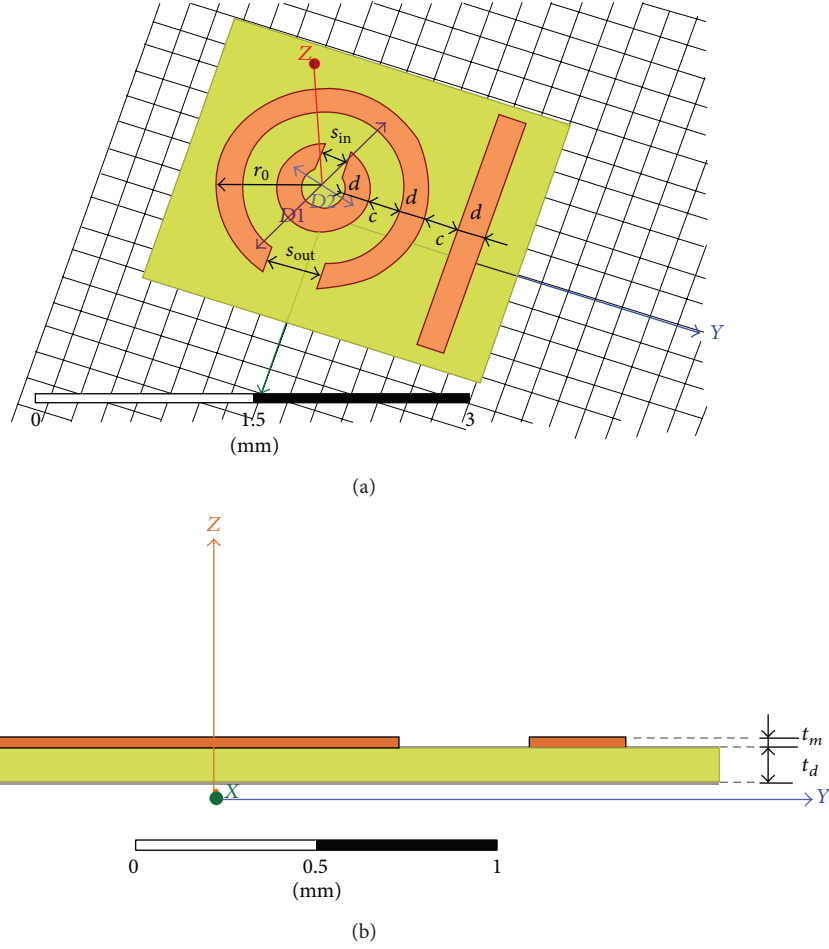


FIGURE 2: SRR  $r_0 = 0.75$  mm, width  $d = 0.18$  mm, spacing between the two rings  $c = 0.24$  mm, thickness of the SRR  $t_m = 0.035$  mm, and the split of the outer ring  $s_{out} = 0.4$  mm and of the inner ring  $s_{in} = 0.2$  mm; the wire has 0.2 mm of width and 1.8 mm of length.

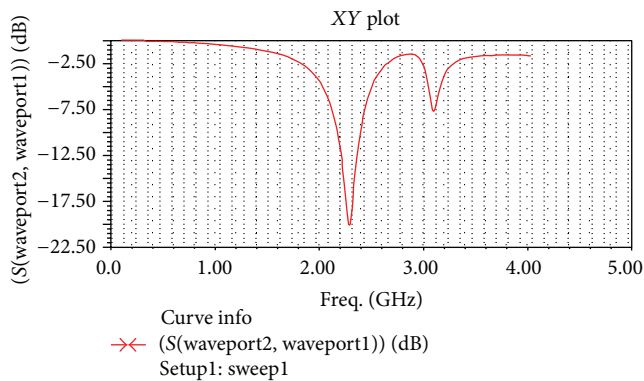


FIGURE 3: Variation of the coefficient of transmission S21 versus frequency at 40°C.

LHM structure is shown in Figure 6, where  $L$  models the total inductance of the two rings of the SRR,  $C$  is the capacitance of the split in the inner and outer ring and the capacitance of the gap between them,  $C_s$  models the coupling between the SRR and the line, and  $L_s$  models the inductance of the wire. After

calculation, we noticed  $L \gg M$ , so the mutual inductance can be neglected and the inductive currents will be neglected.

Figure 5 shows the distribution of the current around the wire and the SRR and demonstrates the previous conclusion.

In Figure 7, we have plotted the calculated S21 parameter versus the frequency using ABCD Matrix approach, which is based on the following equations:

$$A = \left. \frac{V_1}{V_2} \right|_{I_2=0}, \quad B = \left. \frac{V_1}{I_2} \right|_{V_2=0},$$

$$C = \left. \frac{I_1}{V_2} \right|_{I_2=0}, \quad D = \left. \frac{I_1}{I_2} \right|_{V_2=0},$$

$$Z_{11} = \frac{A}{C}, \quad Z_{12} = \frac{(AD - BC)}{C},$$

$$Z_{21} = \frac{1}{C}, \quad Z_{22} = \frac{D}{C},$$

$$S_{11} = \frac{[(Z_{11} - Z_0)(Z_{22} + Z_0) - Z_{12}Z_{21}]}{\Delta Z},$$

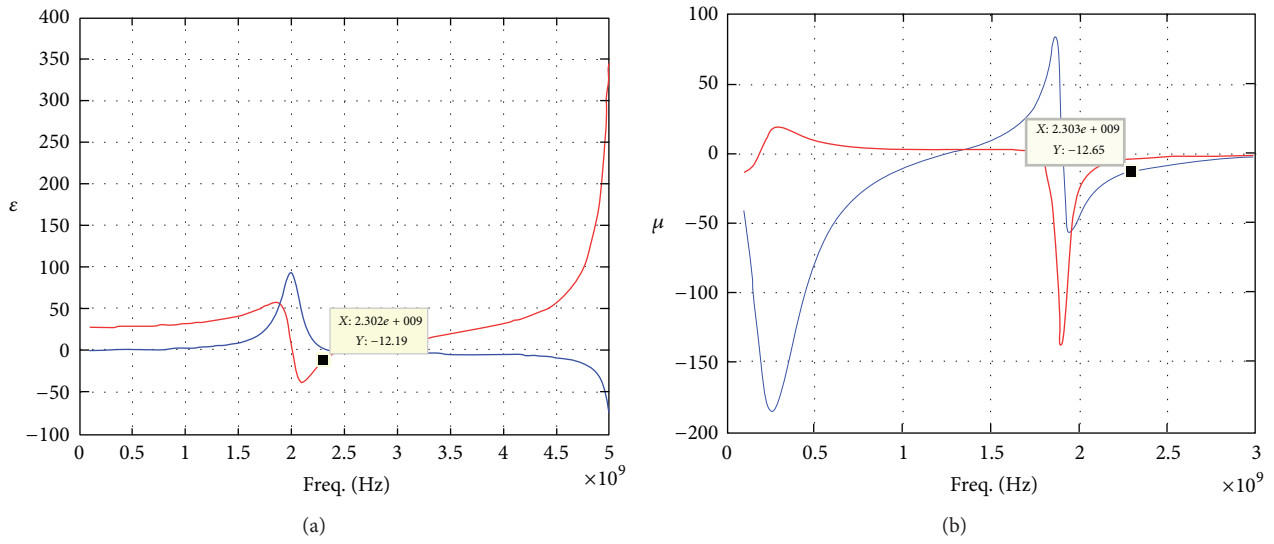


FIGURE 4: The variation of the real (red) and imaginary part (blue) of the permittivity ( $\epsilon$ ) and the variation of the real (red) and imaginary part (blue) of the permeability ( $\mu$ ) according to the frequency.

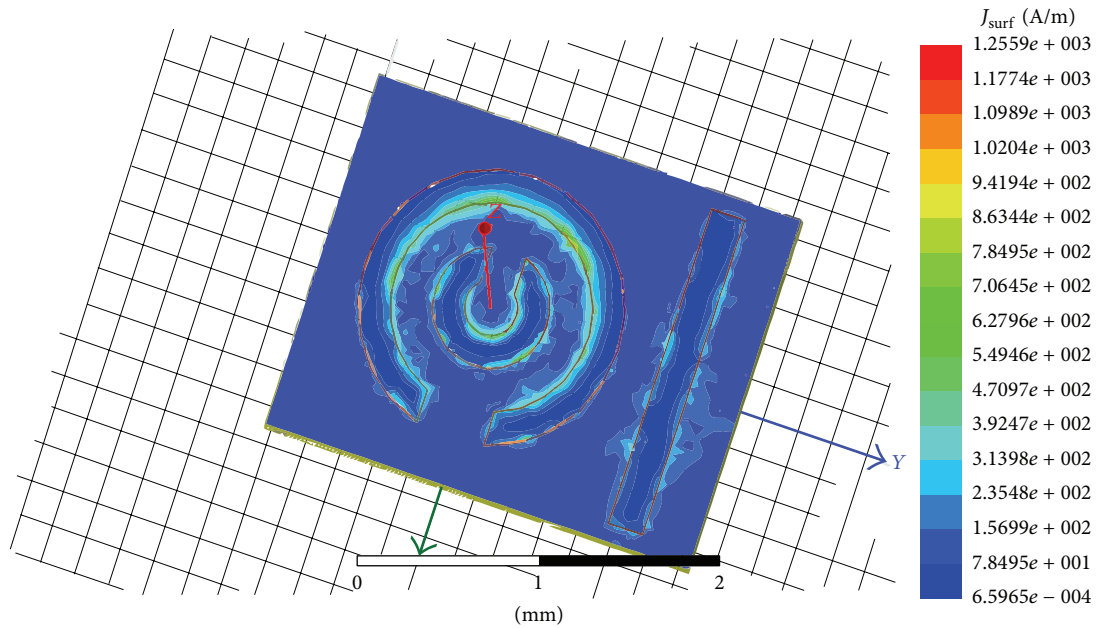


FIGURE 5: The distribution of the current around the wire and the SRR.

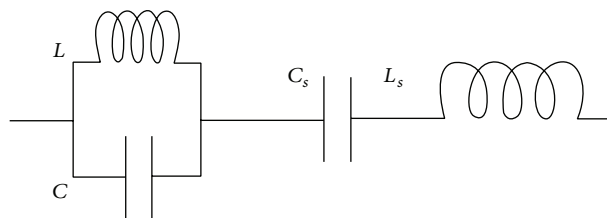


FIGURE 6: Equivalent circuit model for the LHM structure.

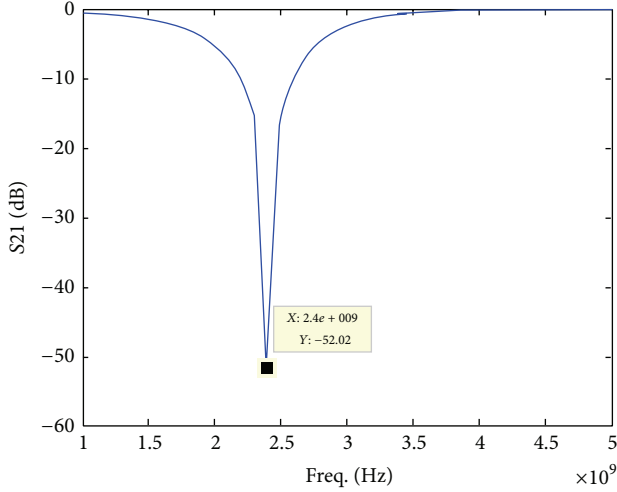


FIGURE 7: The variation of S21 versus frequency calculated using the ABCD Matrix approach from the equivalent circuit model.

$$S_{21} = \frac{[(Z_{11} + Z_0)(Z_{22} - Z_0) - Z_{12}Z_{21}]}{\Delta Z},$$

$$\Delta Z = (Z_{11} + Z_0)(Z_{22} + Z_0) - Z_{12}Z_{21}. \quad (1)$$

The ABCD Matrix for this kind of a cascade connection of two port networks is  $\begin{bmatrix} 1 & Z_T \\ 0 & 1 \end{bmatrix}$  with  $Z_T = j\omega L_s + 1/j\omega C_s + (1 - LC\omega^2)/jC\omega$ ; the parameters  $L$ ,  $C$ ,  $L_s$ , and  $C_s$  can be approximated by the following relationships [25, 26]:

$$L = 8\mu D \left[ \ln\left(\frac{D}{d}\right) + 0.9 + 0.2\frac{\omega^2}{D^2} + \frac{0.5c^2}{(\rho D)^2} + \frac{0.4s(c+d)}{D^2} - 0.5\ln\left(\frac{d+t_m}{d}\right) \right]$$

$$+ 2\mu D \left[ \ln\left(\frac{1}{\rho}\right) - 0.6 + 0.7\rho^2 + \left(0.2 + \frac{1}{12\rho^2}\right)\frac{d^2}{D^2} \right],$$

$$C = \left[0.06 + 3.5 \times 10^{-5} \times (r_{out} + r_{in})\right] + \varepsilon\varepsilon_0 \frac{dt_m}{s},$$

$$L_s = \frac{\mu l}{\pi} \left[ 2\ln\left(\frac{2.067l}{\omega}\right) + 0.36\frac{\omega}{l} + 0.25\frac{\omega^2}{l^2} \right],$$

$$C_s = \varepsilon\varepsilon_0 \frac{dt_m}{c},$$

$$\rho = \frac{d+c}{D}, \quad D = 0.5(D1 + D2). \quad (2)$$

The resonant frequency calculated is 2.4 GHz with return loss of -52 dB. We note that the calculated and the simulated results are very close.

Each time the temperature varies, it leads to a variation in the dielectric characteristics of the substrate BaTiO<sub>3</sub> of the

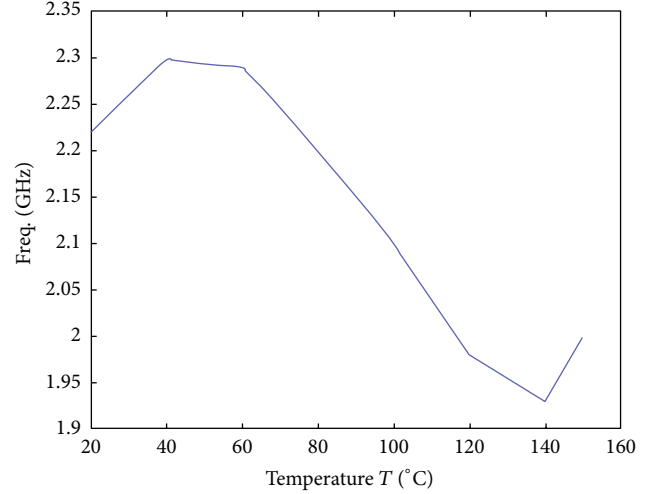


FIGURE 8: Variation of frequency versus the temperature.

LHM structure which affects its capacitance which depends inversely on the frequency of resonance of the structure.

To obtain the effects of the temperature on the S parameters and hence on the resonant frequency of the MTM structure, we have studied the variation of the dielectric characteristics of the BaTiO<sub>3</sub> that are corresponding to well-known temperatures according to the variation of the resonant frequency of the MTM structure. In the interval of temperature from 20° to 150°, we have plotted the variation of the resonance frequency in function of temperature (see Figure 8).

The minimum and maximum temperatures that can be detected by this sensor depend on the minimum and maximum temperatures that can be supported by the BaTiO<sub>3</sub> substrate.

The BaTiO<sub>3</sub> material is sintered at high temperatures, which allows an operation at wide range temperatures [27]. So, TMax has a high value and because this material has no linear variation of the temperature in function of  $\varepsilon$ , the variation of the resonance frequency will not have a linear variation in function of the temperature (when  $\varepsilon$  increases the resonant frequency of the MTM structure decreases; this is because the frequency is inversely proportional to the capacitive effect which is proportional to epsilon), but we can note that the curve is linear just in the intervals [20–40], [40–60], [60–120], and [120–140].

We have done this study in GHz regime, but the variations of the frequency are in the order of MHz; that is why in Table 1 we have presented the sensibility of this sensor in MHz.

#### 4. Conclusion

This paper presents a sensor of temperature using the meta-material. We have studied the variations of the resonant frequency according to the permittivity of structure which depend on the temperature.

We have proposed an equivalent circuit model of our LHM structure and using the software MATLAB we have

TABLE 1

The interval of temperature	$\Delta f$ [MHz]	The sensibility [MHZ]
[20°–40°]	80	4
[40°–60°]	30	1.5
[60°–80°]	90	4.5
[80°–100°]	100	5
[100°–120°]	140	7
[120°–140°]	70	3.5

calculated the coefficients of reflection and transmission; the obtained curves are in accordance with those obtained by the HFSS.

Using the two methods HFSS and Matrix ABCD, we can notice that the variation in the temperature involves a variation of the frequency of resonance and it is illustrated in a curve.

Because the BaTiO<sub>3</sub> has big dependence of the relative permittivity with the temperature, this sensor can be tailored in a wide range of applications.

Based on the promising results of this sensor, we believe that the use of the proposed sensor's topology will efficiently be used in various sensing applications including pressure and humidity and also in biological and chemical sensing for any region of wavelengths.

## Conflict of Interests

The authors declare that there is no conflict of interests regarding the publication of this paper.

## References

- [1] J. B. Pendry, A. J. Holden, W. J. Stewart, and I. Youngs, "Extremely low frequency plasmons in metallic mesostructures," *Physical Review Letters*, vol. 76, no. 25, pp. 4773–4776, 1996.
- [2] J. B. Pendry, A. J. Holden, D. J. Robbins, and W. J. Stewart, "Magnetism from conductors and enhanced nonlinear phenomena," *IEEE Transactions on Microwave Theory and Techniques*, vol. 47, no. 11, pp. 2075–2084, 1999.
- [3] D. R. Smith, W. J. Padilla, D. C. Vier, S. C. Nemat-Nasser, and S. Schultz, "Composite medium with simultaneously negative permeability and permittivity," *Physical Review Letters*, vol. 84, no. 18, pp. 4184–4187, 2000.
- [4] R. A. Shelby, D. R. Smith, and S. Schultz, "Experimental verification of a negative index of refraction," *Science*, vol. 292, no. 5514, pp. 77–79, 2001.
- [5] X. Shen, T. J. Cui, J. Zhao, H. F. Ma, W. X. Jiang, and H. Li, "Polarization-independent wide-angle triple-band metamaterial absorber," *Optics Express*, vol. 19, no. 10, pp. 9401–9407, 2011.
- [6] D. J. Barasara, J. C. Prajapati, and A. M. Dethalia, "Multifrequency fractal antenna," *International Journal of Scientific & Engineering Research*, vol. 3, no. 7, 2012.
- [7] S. Niranchanan and D. Budimir, "Novel folded SRR-loaded waveguide bandpass filters," in *IEEE Antennas and Propagation Society International Symposium*, pp. 1–4, San Diego, Calif, USA, 2008.
- [8] A. Ishimaru, S. Jaruwatanadilok, and Y. Kuga, "Generalized surface plasmon resonance sensors using metamaterials and negative index materials," *Progress in Electromagnetics Research*, vol. 51, pp. 139–152, 2005.
- [9] A. V. Kabashin, P. Evans, S. Pastkovsky et al., "Plasmonic nanorod metamaterials for biosensing," *Nature Materials*, vol. 8, no. 11, pp. 867–871, 2009.
- [10] A. Alù and N. Engheta, "Dielectric sensing in  $\epsilon$ -near-zero narrow waveguide channels," *Physical Review B—Condensed Matter and Materials Physics*, vol. 78, no. 4, Article ID 045102, 2008.
- [11] E. Ekmekci and G. Turhan-Sayan, "Multi-functional metamaterial sensor based on a broad-side coupled SRR topology with a multi-layer substrate," *Applied Physics A: Materials Science and Processing*, vol. 110, no. 1, pp. 189–197, 2013.
- [12] L. La Spada, F. Bilotti, and L. Vegni, "Metamaterial-based sensor design working in infrared frequency range," *Progress in Electromagnetics Research B*, vol. 34, pp. 205–223, 2011.
- [13] C. Drexler, T. V. Shishkanova, C. Lange et al., "Terahertz splitting metamaterials as transducers for chemical sensors based on conducting polymers: a feasibility study with sensing of acidic and basic gases using polyaniline chemosensitive layer," *Microchimica Acta*, vol. 181, no. 15–16, pp. 1857–1862, 2014.
- [14] F. Miyamaru, K. Hattori, K. Shiraga et al., *Highly Sensitive Terahertz Sensing of Glycerol-Water Mixtures with Metamaterials*, Springer Science+Business Media New York, New York, NY, USA, 2013.
- [15] C. Mandel, B. Kubina, M. Schüßler, and R. Jakoby, "Metamaterial-inspired passive chipless radio-frequency identification and wireless sensing," *Annals of Telecommunications*, vol. 68, no. 7–8, pp. 385–399, 2013.
- [16] A. C. Strikwerda, H. Tao, E. A. Kadlec et al., "Metamaterial based terahertz detector," in *Proceedings of the 36th International Conference on Infrared, Millimeter, and Terahertz Waves (IRMMW-THz '11)*, pp. 1–2, Houston, Tex, USA, October 2011.
- [17] M. Puentes, C. Weiß, M. Schüßler, and R. Jakoby, "Sensor array based on split ring resonators for analysis of organic tissues," in *Proceedings of the IEEE MTT-S International Microwave Symposium Digest (MTT '11)*, pp. 1–4, IEEE, Baltimore, Md, USA, June 2011.
- [18] H.-J. Lee, J.-H. Lee, and H.-I. Jung, "A symmetric metamaterial element-based RF biosensor for rapid and label-free detection," *Applied Physics Letters*, vol. 99, no. 16, Article ID 163703, 2011.
- [19] T. Chen, S. Li, and H. Sun, "Metamaterials application in sensing," *Sensors*, vol. 12, no. 3, pp. 2742–2765, 2012.
- [20] R. Melik, E. Unal, N. K. Perkgoz, C. Puttlitz, and H. V. Demir, "Metamaterial-based wireless RF-MEMS strain sensors," in *Proceedings of the 9th IEEE Sensors Conference (SENSORS '10)*, pp. 2173–2176, November 2010.
- [21] J. D. Baena, J. Bonache, F. Martín et al., "Equivalent-circuit models for split-ring resonators and complementary split-ring resonators coupled to planar transmission lines," *IEEE Transactions on Microwave Theory and Techniques*, vol. 53, no. 4, pp. 1451–1460, 2005.
- [22] J.-G. Hyun, S. Lee, S.-D. Cho, and K.-W. Paik, "Frequency and temperature dependence of dielectric constant of epoxy/BaTiO<sub>3</sub> composite Embedded Capacitor Films (ECFs) for organic substrate," in *Proceedings of the 55th Electronic Components and Technology Conference (ECTC '05)*, pp. 1241–1247, IEEE, June 2005.

- [23] S. Liebus, *Couches minces ferroélectriques appliquées aux dispositifs microondes accordables en fréquence [Ph.D. thesis]*, Université de Limoges, Limoges, France, 2003.
- [24] R. W. Ziolkowski, "Design, fabrication, and testing of double negative metamaterials," *IEEE Transactions on Antennas and Propagation*, vol. 51, no. 7, pp. 1516–1529, 2003.
- [25] S. S. Mohan, "The design, modeling and optimization of on-chip inductor and transformer circuits," December 1999.
- [26] M. F. Wu, F. Y. Meng, Q. Wu, J. Wu, and L. W. Li, "A compact equivalent circuit model for the SRR structure in metamaterials," in *Proceedings of the Asia-Pacific Conference Proceedings; Microwave Conference Proceedings (APMC '05)*, vol. 1, December 2005.
- [27] F. Jona and G. Shirane, *Ferroelectric Crystals*, Dover, New York, NY, USA, 1993.

## Research Article

# Modified Luneburg Lens Based on Metamaterials

**Haibing Chen, Qiang Cheng, Aihua Huang, Junyan Dai, Huiying Lu, Jie Zhao, Huifeng Ma, Weixiang Jiang, and Tiejun Cui**

*State Key Laboratory of Millimeter Waves, Department of Radio Engineering, Southeast University, Nanjing 210096, China*

Correspondence should be addressed to Haibing Chen; [chhbyxyy@126.com](mailto:chhbyxyy@126.com)

Received 7 October 2014; Revised 22 January 2015; Accepted 29 January 2015

Academic Editor: Giuseppe Castaldi

Copyright © 2015 Haibing Chen et al. This is an open access article distributed under the Creative Commons Attribution License, which permits unrestricted use, distribution, and reproduction in any medium, provided the original work is properly cited.

We present the design, fabrication, and experimental characterization of a modified two-dimensional Luneburg lens based on bulk metamaterials. The lens is composed by a number of concentric layers. By varying the geometric dimensions of unit cells in each layer, the gradient refractive index profile required for the modified Luneburg lens can be achieved. The cylindrical waves generated from a point source at the focus point of the lens could be transformed into plane waves as desired in the microwave frequency. The proposed modified Luneburg lens can realize wide-angle beam scanning when the source moves along the circumferential direction inside the lens. Numerical and experimental results validate the performance of the modified Luneburg lens.

## 1. Introduction

In the past a few years, the emergence of metamaterials have aroused great interests due to their fascinating properties and potential applications in microwave and optical engineering, like the superlens, invisible cloak, and other transformation devices [1–3]. Metamaterials are usually composed of periodic resonant or nonresonant structures, and the effective properties can be inherited from the design variations of the unit cells. Such artificial materials provide us a powerful tool for manipulation of electromagnetic waves on the subwavelength scale, which makes the capture and control of electromagnetic near fields in designed structures become possible.

In particular, the gradient refractive index (GRIN) metamaterials play important roles in the design of new concept devices, whose index profile can be varied gradually according to the designs. By arranging the same type of metamaterial element with different geometries, the spatial gradient of the refraction index can be finally introduced. The GRIN metamaterials can provide larger refraction index contrast than the natural materials, and they can also be tuned by electric or optical means, which makes them more attractive in practical applications.

One typical application of GRIN metamaterials is the microwave lens, which can transform the cylindrical or spherical waves into planar waves. Compared to the traditional dielectric lens, the GRIN metamaterial lens offers more freedom for designers to elaborate their work as stated above. Up to now, a number of GRIN metamaterial lenses have been demonstrated, such as Maxwell fisheye lenses, Eaton lenses, Wood lenses, and Luneburg lenses [3–8]. Owing to the compact size, reduced weight, and convenience of fabrication, the GRIN metamaterial lens has a number of advantages compared to the traditional lens [9–14].

In this paper, we have designed and fabricated a modified 2D-Luneburg lens based on the GRIN metamaterials [15–17]. Different from the traditional Luneburg lens, the current lens can be excited internally, making it more flexible in practical applications [18]. The modified Luneburg lens can realize wide-angle scanning when the excitation probe moves along the circumferential direction inside the lens. By periodically placing I-shaped units with varied dimensions in the radial direction, we can get the desired refractive index profile. A probe antenna has been inserted within the sample as the excitation. The near-field electric distributions have been measured and plotted. Excellent plane waves could be observed outside the modified Luneburg lens, which shows good performance of the designed sample.

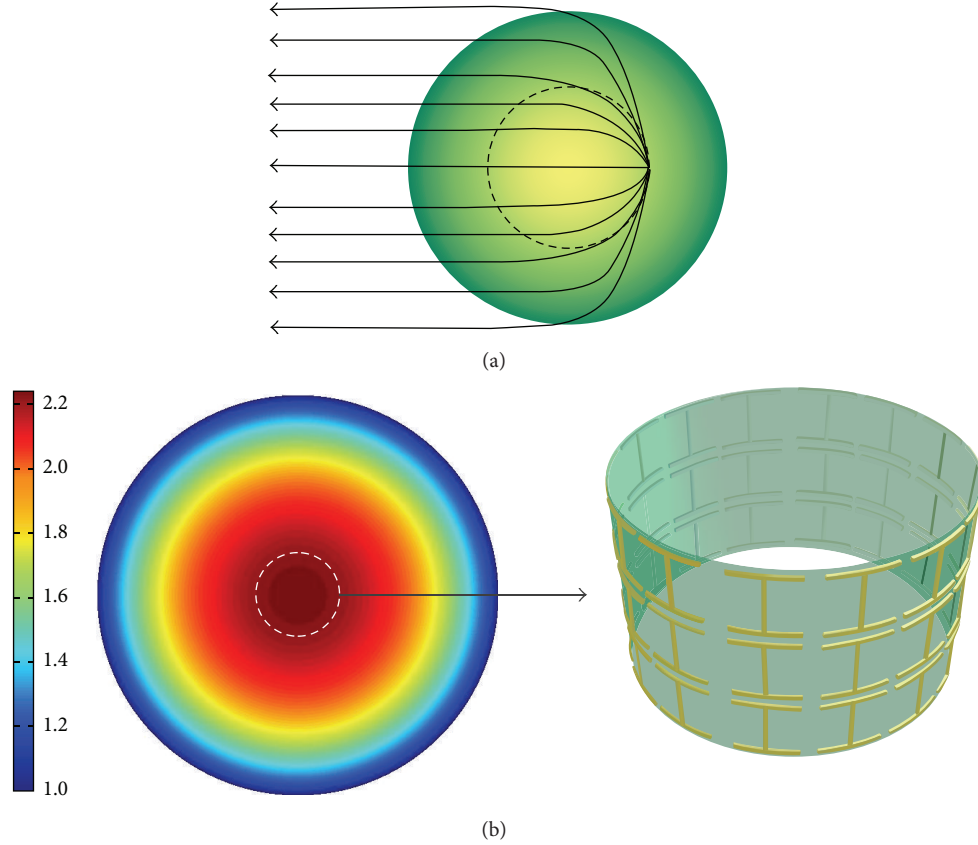


FIGURE 1: (a) Ray trajectories through the modified Luneburg lens, where the source is located inside the lens. (b) Refraction index profile for the modified Luneburg lens; the inset shows one of the concentric layers of the designed lens.

## 2. Design and Simulation

For a two-dimensional modified Luneburg lens as shown in Figure 1, the radially inhomogeneous refraction index profile satisfies

$$n(r) = \frac{(a^2 + f^2 - r^2)^{1/2}}{f} \quad (0 \leq r \leq a), \quad (1)$$

where  $a$  is the radius of the lens and  $f$  is the distance from the lens center to the focus. The medium outside the lens is free space with the relative refraction index  $n(a) = 1$ , in order to keep impedance match at the lens boundary. Figure 1(a) shows the ray trajectories through the modified Luneburg lens. The rays from the internal source are transmitted through the lens to produce a parallel beam on the other side of the lens. Here we choose  $f < a$  to ensure that the focus is located inside the lens. When  $f = a/2$ , the refraction index profile inside the lens can be found in Figure 1(b), ranging from 1 to 2.236.

The unit cell of the modified Luneburg lens is shown in Figure 2, which is actually a nonresonant I-shaped metallic structure upon a dielectric substrate [19]. Electric response could be exhibited for the I-shaped unit under the illumination of external electric field, resulting in the variation of the effective permittivity according to effective medium theory [20]. Here, the reason we choose I-shaped structure

as our unit cell is that it has few parameters to tune. Actually, other nonresonant structures having electric response can be our unit cell under rational design. In our design, the two horizontal bars are kept to have the same length to the vertical bar in each unit. Therefore it is quite easy to achieve different permittivity distributions as required by simply tuning the length of the bar. Due to the periodicity of the composing unit, it is hard to realize a modified Luneburg lens with continuous refraction index as required by (1). To make an approximation, the discretization method can be utilized to realize the desired modified Luneburg lens. Here we divide the whole lens into fifteen concentric layers. All the units in the same layer have the equal geometric dimensions, as shown in Figure 1(b). FR4 is chosen as the substrate with the relative permittivity 4.3 and the thickness 0.2 mm. The periodicity of each unit is set to be 3.333 mm. All the geometrical dimensions of the I-shaped unit have been shown in Figure 2(a) except the length of the vertical bar at different layers, which should be carefully optimized to meet the requirement of the refraction index profile at 10 GHz.

In order to show the relationship between the geometry dimensions and the constitutive parameters of the I-shaped unit, numerical simulations have been made to get the corresponding refraction index at  $f = 10$  GHz following the standard retrieval procedure [21]. The length  $w$  in Figure 2 is chosen to change gradually to tune the refraction index as

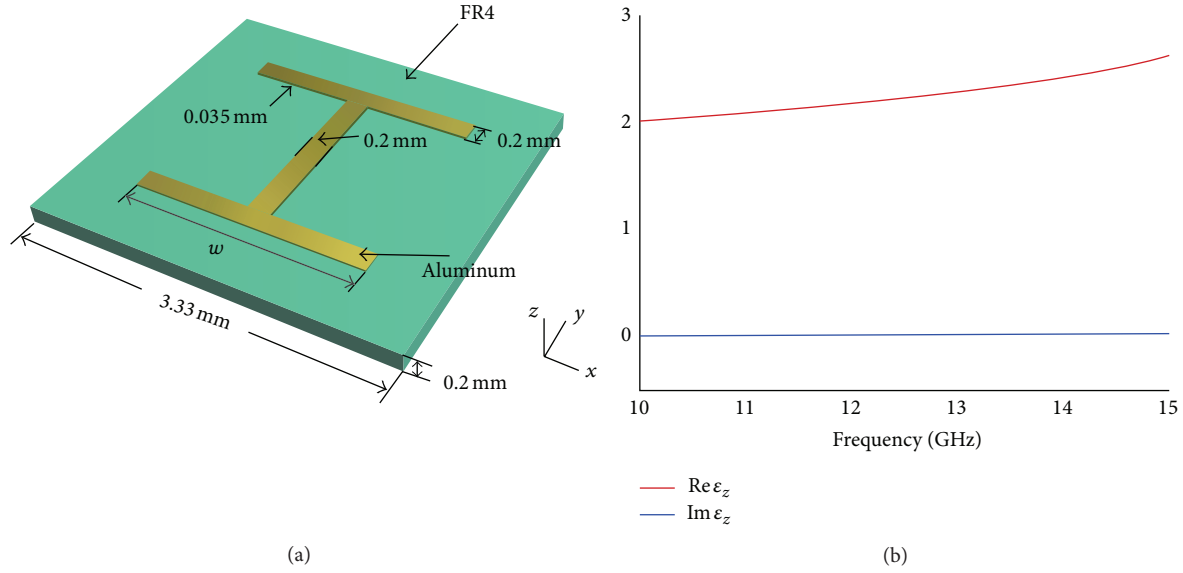


FIGURE 2: The unit cell of the modified Luneburg lens. (a) The perspective view. (b) The effective  $\epsilon_z$  of the unit.

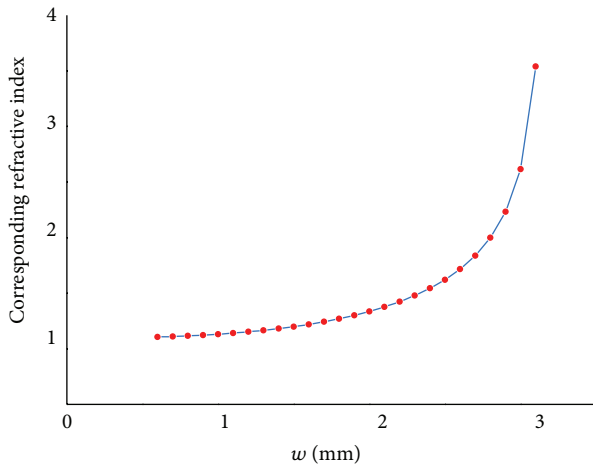


FIGURE 3: The relationship between the parameter  $w$  (shown in Figure 2(a)) and the corresponding effective refractive index.

required by the modified Luneburg lens. The width of the bars is fixed to be 0.2 mm. From Figure 3, the effective refraction index increases gradually with the growth of  $w$ , ranging from 1 to 3.5.

Like the traditional 2D Luneburg lenses, the modified one can also realize beam shaping and beam scanning, which can transform cylindrical waves into plane waves in various directions. To demonstrate the performance of the proposed lens, full wave numerical simulations have been made by using the software package COMSOL. A 2D point source has been inserted into the lens as the excitation, as depicted by the cross in Figure 4. The radius of the lens is set to be 50 mm. The electric field inside and outside the lens has been illustrated in Figure 4, where the lens with continuous and discrete refraction index profile has been taken into considerations. By comparing Figures 4(a) and 4(b), it is

clear that unavoidable scattering has emerged due to the discretization in the practical realization for its impedance mismatch. However, the beam shaping phenomenon is still quite obvious. Under ideal conditions, there should be almost no energy loss when electromagnetic waves run through the lens, since the imaginary part of the effective dielectric constant is approximately zero as shown in Figure 2(b). However, loss indeed exists because of the productive deviation and tiny impedance mismatch to the air part. By moving the source along the circumference, it is possible to realize beam scanning toward different directions, as shown in Figure 4(c), which is critically important for radar detections.

### 3. Fabrication and Measurement

To verify the performance of the designed Luneburg lens, we have fabricated the sample (see Figure 5), which is constituted by 15 concentric layers with the gap between adjacent layers 3.333 mm. The I-shaped unit is etched on the copper cladding of the FR4 substrate. All the layers have been inserted into a Styrofoam board to keep the sample stable in the experiment. Each layer has 3 units in the vertical direction with the height 10 mm, as required by the scanning waveguide mentioned later.

A two-dimensional microwave scanning apparatus has been used in the experiment to obtain the near field distributions of the fabricated sample, which is actually a planar waveguide whose dominant mode is TEM mode [20]. Two motors are placed below the bottom metallic plate, which can scan the area of 200 mm \* 200 mm under the control of the computer. Both the excitation and detection probes have been connected to the vector network analyzer (Agilent N5230C), and the measured data will be sent back to the computer for recording and processing. In this experiment, the electric field within a 2D plane (1 mm higher above the sample) has been measured with the scanning of detection probe. The gap

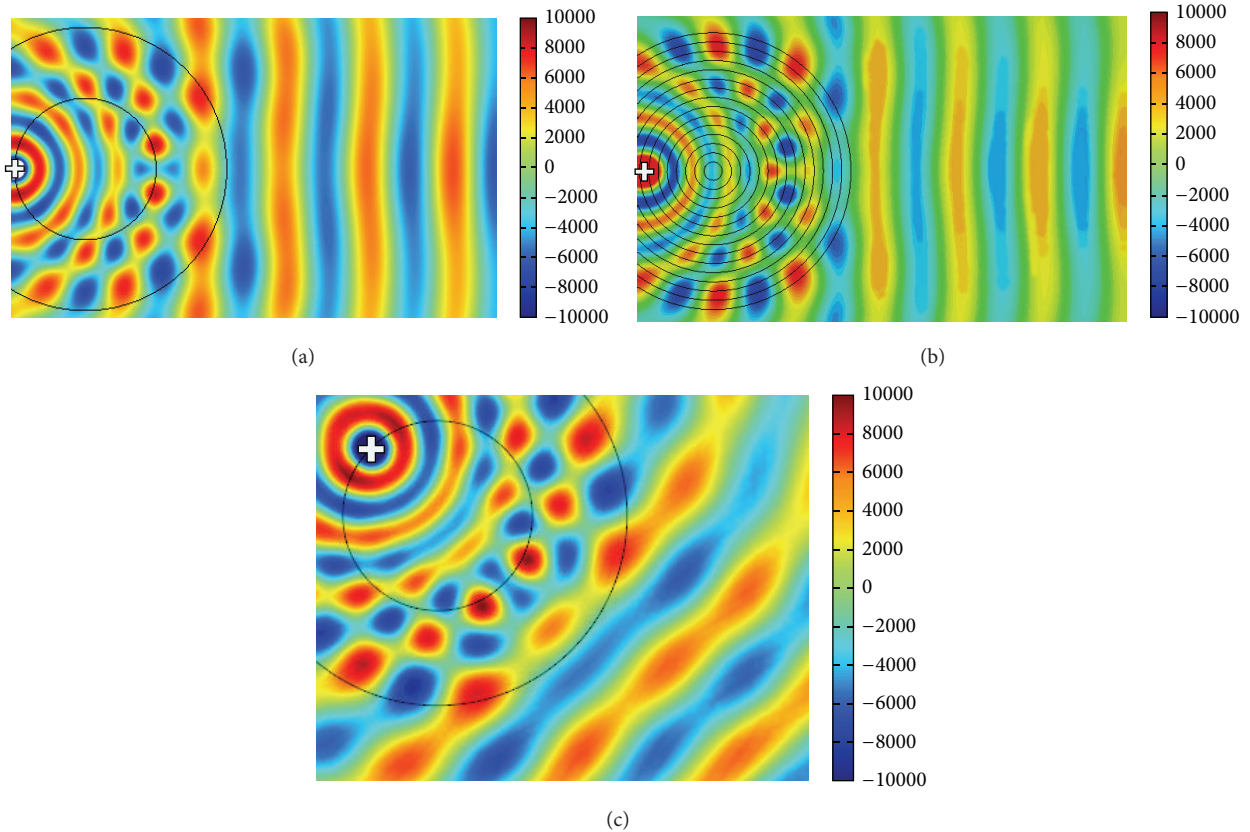


FIGURE 4: Simulated electric field distributions for a point source embedded within the modified Luneburg lens at 10 GHz. (a) The lens has the ideal refractive index distributions as shown in (1). (b) The refractive index distributions of the lens are discretized. (c) Beam scanning for a point source moving along the circumferential direction.

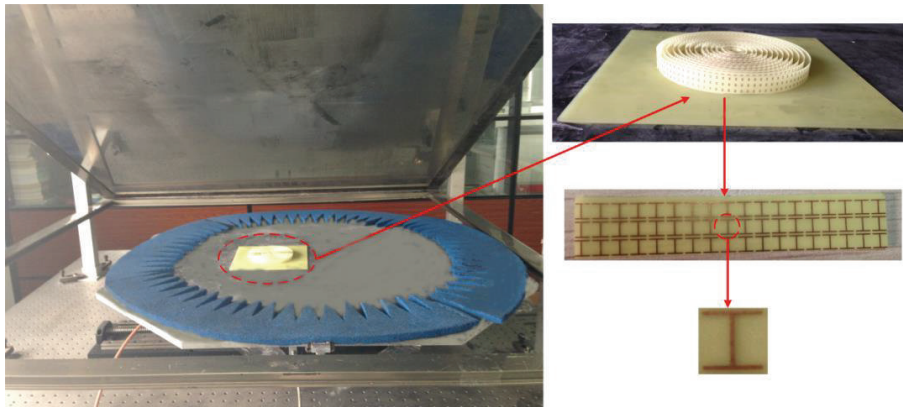


FIGURE 5: The experimental setup of the modified Luneburg lens, where the inset shows the details of the sample.

between the bottom and the upper plate is 12 mm to avoid the emergence of higher order modes for the planar waveguide. The excitation probe lies between the seventh and eighth layer of the sample to generate the cylindrical waves. Microwave absorption materials are placed at the edge of bottom plate to reduce the unwanted wave reflections.

The electric field distribution around the sample is measured and plotted, as shown in Figures 6(a) and 6(b), where the location of the sample is marked by the red dashed lines.

It can be observed that cylindrical waves propagate on the left side of the sample and plane waves propagate on the right side of the sample. We choose 10.5 GHz as our observed frequency point rather than the designed frequency point 10 GHz, because it has frequency deviation owing to the fabrication error. There is also tiny impedance mismatch at the boundary of the fabricated sample, since the effective refractive index for the outmost layer is 1.141, which is slightly higher than that of air, leading to the unwanted scattering.

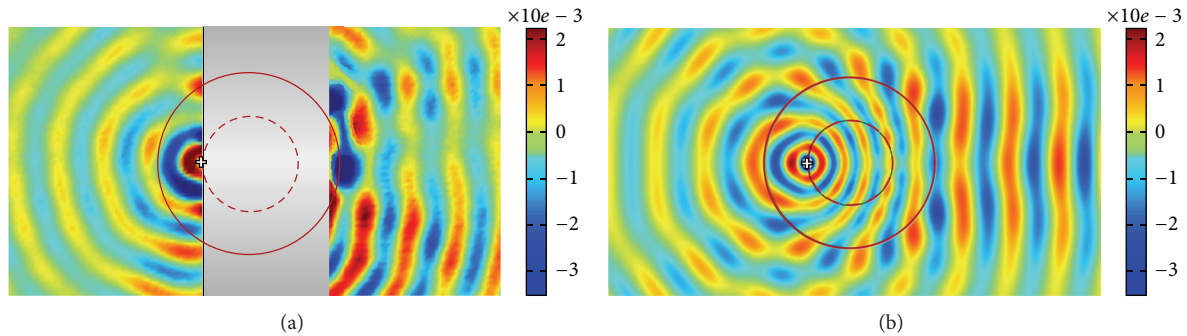


FIGURE 6: Electric field distributions for a point source embedded within the fabricated lens at the frequency of 10.5 GHz, which is indicated by the cross. (a) Measured. (b) Simulated.

The grey region represents the region where we cannot plot due to the limitation of the testing platform. Comparing the simulation result with the measurement result at the frequency of 10.5 GHz, we can find that they agree well, showing great potentials for microwave and optical applications in the future.

#### 4. Conclusion

In this paper, a modified 2D-Luneberg lens has been designed, fabricated, and experimentally characterized based on the I-shaped units. Gradient index distributions have been realized by adjusting the dimensions of the basic unit based on the effective medium theory. Experimental results show that cylindrical waves can be transformed into plane waves, which is consistent with the theoretical predictions.

#### Conflict of Interests

The authors declare that there is no conflict of interests regarding the publication of this paper.

#### Acknowledgments

This work was supported by National Science Foundation of China (61138001 and 61171026), National High Tech (863) Projects (2011AA010202 and 2012AA030402), 111 Project (111-2-05), and the Natural Science Foundation of Jiangsu Province (BK2012019).

#### References

- [1] J. B. Pendry, D. Schurig, and D. R. Smith, "Controlling electromagnetic fields," *Science*, vol. 312, no. 5781, pp. 1780–1782, 2006.
- [2] D. Schurig, J. J. Mock, B. J. Justice et al., "Metamaterial electromagnetic cloak at microwave frequencies," *Science*, vol. 314, no. 5801, pp. 977–980, 2006.
- [3] U. Leonhardt, "Optical conformal mapping," *Science*, vol. 312, no. 5781, pp. 1777–1780, 2006.
- [4] T. Zentgraf, Y. M. Liu, M. H. Mikkelsen, J. Valentine, and X. Zhang, "Plasmonic Luneburg and Eaton lenses," *Nature Nanotechnology*, vol. 6, no. 3, pp. 151–155, 2011.
- [5] A. Di Falco, S. C. Kehr, and U. Leonhardt, "Luneburg lens in silicon photonics," *Optics Express*, vol. 19, no. 6, pp. 5156–5157, 2011.
- [6] X. D. Wu and J.-J. Laurin, "Fan-beam millimeter-wave antenna design based on the cylindrical Luneburg lens," *IEEE Transactions on Antennas and Propagation*, vol. 55, no. 8, pp. 2147–2156, 2007.
- [7] L. H. Gabrielli and M. Lipson, "Integrated Luneburg lens via ultra-strong index gradient on silicon," *Optics Express*, vol. 19, no. 21, pp. 20122–20127, 2011.
- [8] J. Hunt, T. Tyler, S. Dhar et al., "Planar, flattened Luneburg lens at infrared wavelengths," *Optics Express*, vol. 20, no. 2, pp. 1706–1713, 2012.
- [9] W. X. Jiang, H. F. Ma, Q. Cheng, and T. J. Cui, "Virtual conversion from metal object to dielectric object using metamaterials," *Optics Express*, vol. 18, no. 11, pp. 11276–11281, 2010.
- [10] A. Dhoubi, S. N. Burokur, A. de Lustrac, and A. Priou, "X-band metamaterial-based Luneburg lens antenna," in *Proceedings of the IEEE Antennas and Propagation Society International Symposium (APSURSI '13)*, pp. 1292–1293, IEEE, July 2013.
- [11] Q. Cheng, H. F. Ma, and T. J. Cui, "Broadband planar Luneburg lens based on complementary metamaterials," *Applied Physics Letters*, vol. 95, no. 18, Article ID 181901, 2009.
- [12] J. B. Pendry, "Negative refraction makes a perfect lens," *Physical Review Letters*, vol. 85, no. 18, pp. 3966–3969, 2000.
- [13] H. F. Ma, X. Chen, H. S. Xu, X. M. Yang, W. X. Jiang, and T. J. Cui, "Experiments on high-performance beam-scanning antennas made of gradient-index metamaterials," *Applied Physics Letters*, vol. 95, no. 9, Article ID 094107, 2009.
- [14] H. F. Ma and T. J. Cui, "Three-dimensional broadband and broad-angle transformation-optics lens," *Nature Communications*, vol. 1, no. 8, article 124, 2010.
- [15] T. Koschny, M. Kafesaki, E. N. Economou, and C. M. Soukoulis, "Effective medium theory of left-handed materials," *Physical Review Letters*, vol. 93, no. 10, Article ID 107402, 2004.
- [16] Y. Wu, Y. Lai, and Z.-Q. Zhang, "Effective medium theory for elastic metamaterials in two dimensions," *Physical Review B—Condensed Matter and Materials Physics*, vol. 76, no. 20, Article ID 205313, 2007.
- [17] D. Headland, W. Withayachumnankul, M. Webb, and D. Abbott, "Beam deflection lens at terahertz frequencies using a hole lattice metamaterial," in *Proceedings of the 38th International Conference on Infrared, Millimeter, and Terahertz Waves (IRMMW-THz '13)*, vol. 10, pp. 1–2, IEEE, Mainz, Germany, September 2013.

- [18] A. S. Gutman, "Modified Luneberg lens," *Journal of Applied Physics*, vol. 25, no. 7, pp. 855–859, 1954.
- [19] M. Choi, S. H. Lee, Y. Kim et al., "A terahertz metamaterial with unnaturally high refractive index," *Nature*, vol. 470, no. 7334, pp. 369–373, 2011.
- [20] W. X. Jiang, T. J. Cui, G. X. Yu, X. Q. Lin, Q. Cheng, and J. Y. Chin, "Arbitrarily elliptical-cylindrical invisible cloaking," *Journal of Physics D: Applied Physics*, vol. 41, no. 8, Article ID 085504, 2008.
- [21] D. R. Smith, D. C. Vier, T. Koschny, and C. M. Soukoulis, "Electromagnetic parameter retrieval from inhomogeneous metamaterials," *Physical Review E—Statistical, Nonlinear, and Soft Matter Physics*, vol. 71, no. 3, Article ID 036617, 2005.

## Research Article

# Compact Two-Section Half-Wave Balun Based on Planar Artificial Transmission Lines

Changjun Liu,<sup>1</sup> Zhenyu Yin,<sup>1</sup> Yilan Yang,<sup>1</sup> and Wen Huang<sup>2</sup>

<sup>1</sup>*School of Electronics and Information Engineering, Sichuan University, Chengdu 610064, China*

<sup>2</sup>*School of Optoelectronics Engineering, Chongqing University of Posts and Telecommunications, Chongqing 40065, China*

Correspondence should be addressed to Changjun Liu; [cjliu@ieee.org](mailto:cjliu@ieee.org)

Received 23 September 2014; Accepted 26 November 2014

Academic Editor: Sanming Hu

Copyright © 2015 Changjun Liu et al. This is an open access article distributed under the Creative Commons Attribution License, which permits unrestricted use, distribution, and reproduction in any medium, provided the original work is properly cited.

Artificial transmission lines are realized by a series of meandered-line inductors, parallel-plate capacitors, and interdigital capacitors, which belong to metamaterial transmission lines. An ameliorated artificial transmission line is proposed to realize a low characteristic impedance transmission line. A two-section half-wave balun at 900 MHz is designed, fabricated, and measured in this paper. The compact balun is based on conventional and ameliorated planar artificial transmission lines instead of microstrip transmission lines. The main advantage of the proposed balun is its size reduction, which occupies only about 10% of a conventional one. Measured results match well with theory and simulation. The balun features excellent amplitude and phase balance in microwave power combining and a reasonable bandwidth of the return loss as well.

## 1. Introduction

A balun is a device to act as a transformer to match an unbalanced circuit to a balanced one, or vice versa, which was first proposed by Marchand in 1944. Owing to the output balanced amplitude characteristic with its phase difference of 180 degrees, it is a key component in balanced circuit topologies, such as balanced antennas and balanced mixers. Various balun configurations have been reported for applications in microwave circuits, such as coupled-line baluns, composite right/left-handed (CRLH) transmission line baluns, Wilkinson power divider baluns, three-line baluns, microstrip taper baluns, and lumped baluns [1–5].

Recently, with the rapid development of modern communication systems, the increasing demands for miniaturized components have been imposed on microwave circuits, as the size reduction in radio frequency (RF) circuit is an important part of the miniaturization and cost reduction of wireless communication systems. The balun as an important passive component was required to be designed to reach the requirement.

In this paper, we proposed a compact two-section half-wave balun at 900 MHz, which was designed with artificial

transmission lines. In recent years, artificial transmission lines [6] have been proposed, and some microwave components with artificial transmission lines have been realized, such as branch-line couplers [7], power dividers [8], and antennas [9, 10]. We proposed modified artificial transmission lines to realize the transmission lines with low characteristic impedance. The proposed design method adopts seven transmission line sections composed of the artificial transmission lines to replace the conventional transmission lines so as to miniaturize the circuit size of the balun as far as possible. The proposed balun demonstrates a very compact dimension of  $28.9 \text{ mm} \times 26.8 \text{ mm}$ , which is about 10% of the area of a conventional balun of this same topology without folded lines. The overall dimension of the proposed realization is approximately  $0.13\lambda_g \times 0.12\lambda_g$ .

## 2. Theoretical Analysis of $N$ -Section Half-Wave Balun

The realization of a three-port balun is based on the forms of a symmetrical four-port network as shown in Figure 1, in which one specified port is terminated with a short or open circuit,

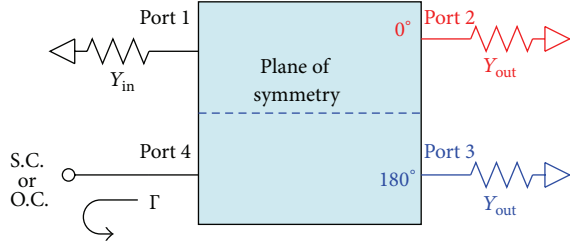
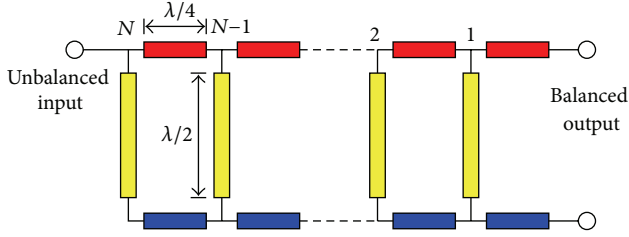


FIGURE 1: Balun topology as a symmetric four-port network.

FIGURE 2:  $N$ -section half-wave balun.

such as a coupled-line Marchand balun or an  $N$ -section half-wave balun.

In this approach, the open- or short-circuit terminal is replaced by a load  $Y_{in}$  to form a fully symmetrical network.  $\Gamma$  is the reflection coefficient of port 4. For synthesizing this kind of three-port balun, the following relationships are required [11].

For the short-circuit case where  $\Gamma = -1$ ,

$$Y_{\text{even}} + Y_{\text{odd}} = 2Y_{\text{in}}. \quad (1)$$

For the open-circuit case where  $\Gamma = 1$ ,

$$\frac{1}{Y_{\text{even}}} + \frac{1}{Y_{\text{odd}}} = \frac{2}{Y_{\text{in}}}. \quad (2)$$

An  $N$ -section half-wave balun [12, 13], which consists of several half-wavelength transmission lines connected in parallel by quarter-wavelength sections as illustrated in Figure 2, can be synthesized directly. It is noted that an  $N$ -section half-wave balun is realized with a port of open-termination with the theory of symmetrical four-port network. The quarter-wavelength series lines can be used for impedance transformation, while the half-wavelength branches achieve phase shift of 180 degrees required for balun operation and compensate each other for broadband performance. Actually, it is an inherently narrow band design since the half-wave transmission line holds only at the center frequency. This kind of balun is designed by properly choosing the line impedance of the half-wave and quarter-wave line to achieve impedance matching and thereby to obtain the best performance.

For simplicity, we focus on analyzing the two-section balun in detail, whose structure is illustrated in Figure 3. The even-mode circuit is shown in Figure 4(a) even-mode, while the odd-mode circuit is shown in Figure 4(b) odd-mode.

Figure 4(a) is naturally a transmission stop network at the operating frequency due to the short circuit formed by the quarter-wavelength open-ended transmission line.

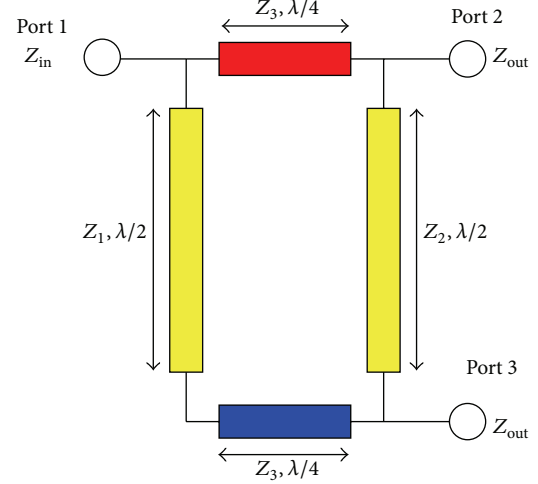


FIGURE 3: Topology of the optimized two-section half-wave balun.

In Figure 4(b), the circuit is equivalent to a quarter-wavelength transmission line for power transmission. The input impedances of the even- and odd-mode circuits are a short circuit for even excitation and an impedance transformer for odd excitation, respectively. Considering the condition of the two-section half-wave balun working at its operating frequency, we have  $Z_{\text{even}} = 0$  and  $Z_{\text{odd}} = Z_3^2/Z_{\text{out}}$ . Then, the relation of  $Z_3$ ,  $Z_{\text{in}}$ , and  $Z_{\text{out}}$  obtained from (2) is

$$Z_3^2 = 2Z_{\text{in}}Z_{\text{out}}. \quad (3)$$

To design a balun at 900 MHz, the final optimized impedances are  $Z_1 = 23.5 \Omega$ ,  $Z_2 = 32.8 \Omega$ , and  $Z_3 = 59.7 \Omega$ . Then by (3) we obtain  $Z_{\text{in}} = 35.6 \Omega$ . Meanwhile, an impedance transformer of quarter-wave line is inserted at the input port for matching with the standard port impedance  $50 \Omega$ , of which the characteristic impedance is  $42.2 \Omega$ .

### 3. Implementations of Artificial Transmission Lines

**3.1. Theory of Conventional Artificial Transmission Lines.** The concept of conventional artificial transmission lines [6] was proposed by Wang et al., which were composed of microstrip structures of interdigital capacitors, meandered-line inductors, and parallel-plate capacitors. The layout and equivalent circuit of a unit of conventional artificial transmission line are shown in Figure 5, respectively. The design and methodology of such kind of conventional artificial transmission lines have been presented in detail in [6].

A unit of artificial transmission line can be equivalent to the circuit of Figure 5(b) and its characteristic impedance  $Z_{\text{ATL}}$  and guided wavenumber  $\beta_{g,\text{ATL}}$  of each unit of artificial transmission line are determined by

$$Z_{\text{ATL}} = \sqrt{\frac{L_{\text{tot}}}{C_{\text{tot}}}}, \quad (4)$$

$$\beta_{g,\text{ATL}} = \omega \sqrt{L_{\text{tot}} \cdot C_{\text{tot}}},$$

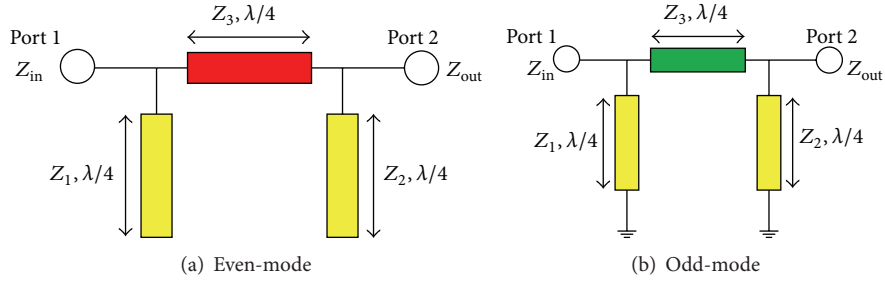


FIGURE 4: Even- and odd-mode analysis of two-section half-wave balun.

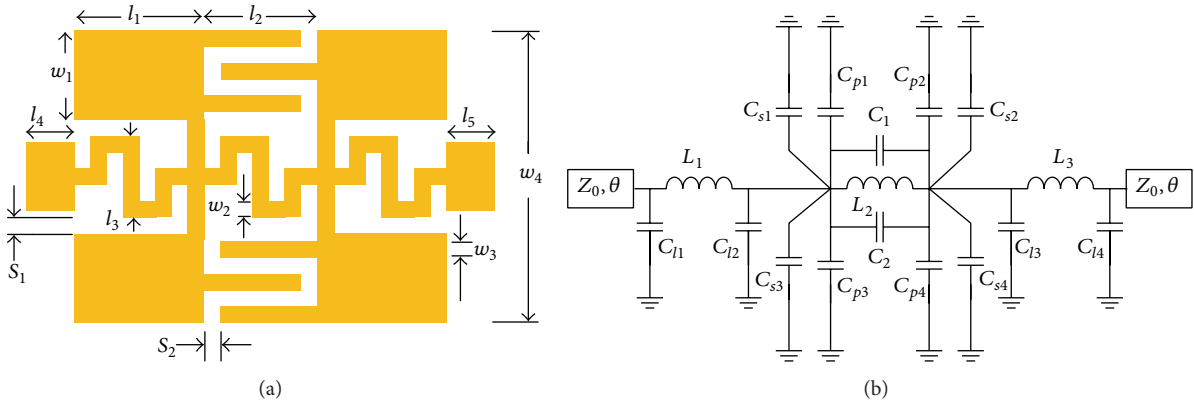


FIGURE 5: A unit of artificial transmission line and its equivalent circuit.

where  $L_{tot}$  and  $C_{tot}$  are equivalent total inductance and capacitance for a unit of artificial transmission line, respectively, and  $\omega$  is the working angle frequency.

As compared with conventional structures of microstrip transmission lines, the required physical dimensions of artificial transmission lines are substantially reduced especially at low frequencies, whereas their electrical properties remain the same. Therefore, the artificial transmission lines have found more and more applications to miniaturizing microwave components and devices.

The design of two-section half-wave balun is performed by full-wave EM simulation software IE3D. The lines of  $Z_3 = 59.7 \Omega$  with 90-degree phase shift are realized by conventional artificial transmission lines. The total capacitance and inductance can be calculated out, which are 4.65 pF and 16.58 nH. Finally, the optimized specific parameters of artificial transmission line of  $Z_3$  are shown in Table 1. Besides, all parameters are defined by the notations in Figure 5(a).

The input impedance matching microstrip line with characteristic impedance  $Z_{trans} = 42.2 \Omega$  is not realized by a structure of conventional symmetric artificial transmission line but by modified artificial transmission lines as shown in Figure 6 to further reduce the total size of the balun. As a result, the optimized specific parameters of artificial transmission lines of  $Z_{trans}$  are shown in Table 2 with the notations marked in Figure 6.

3.2. Realization of Low Characteristic Impedance Line. The conventional artificial transmission lines mentioned above

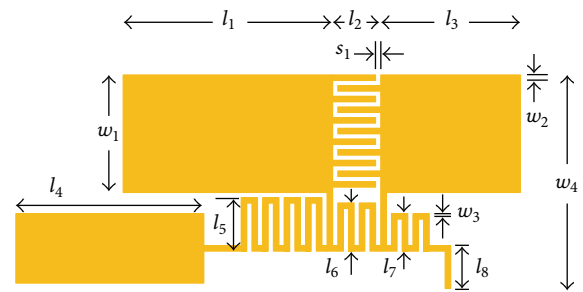
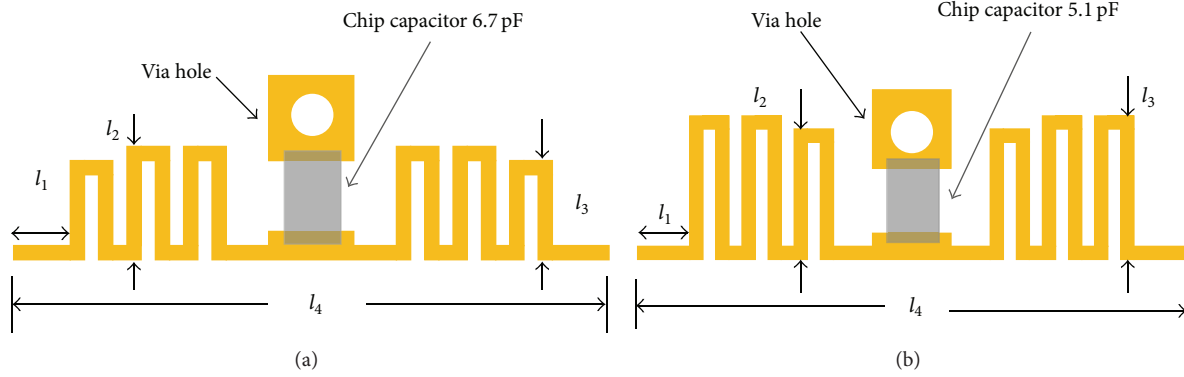


FIGURE 6: Modified asymmetric artificial transmission line.

are usually suitable for lines with characteristic impedance between 30 and 100  $\Omega$ . If the characteristic impedance is too low or too high, the conventional artificial transmission line meets its limitation in the dimensions of corresponding inductors or capacitors with either too high capacitance or inductance. Therefore, in order to design low characteristic impedance line, the artificial transmission line can be ameliorated by applying chip capacitors in place of distributed parallel-plate microstrip capacitors.

The ameliorated artificial transmission lines can be applied to low characteristic impedance lines which are hardly realized by conventional artificial transmission lines, such as the line with characteristic impedance of  $Z_1 = 23.5 \Omega$  or  $Z_2 = 32.8 \Omega$ . In this ameliorated structure, chip capacitors are applied to substitute the parallel-plate capacitors. As shown in Figure 7, there are neither microstrip

FIGURE 7: Ameliorated artificial transmission line of characteristic impedances 23.5  $\Omega$  and 32.8  $\Omega$ .TABLE 1: Dimensions of artificial transmission lines of  $Z_3$  (unit: mm).

Impedance	$l_1$	$l_2$	$l_3$	$l_4$	$l_5$	$w_1$	$w_2$	$w_3$	$w_4$	$s_1$	$s_2$
$Z_3$	4.4	1.8	4.4	0	5	4.3	0.2	0.3	11.6	0.3	0.2

TABLE 2: Dimensions of artificial transmission lines of  $Z_{\text{trans}}$  (unit: mm).

Impedance	$l_1$	$l_2$	$l_3$	$l_4$	$l_5$	$l_6$	$l_7$	$l_8$	$w_1$	$w_2$	$w_3$	$w_4$	$s_1$
$Z_{\text{trans}}$	11.8	1.8	7.6	12.2	1.7	1.5	1.1	4.6	5.8	0.2	0.2	12.1	0.2

interdigital capacitors nor parallel-plate capacitors to realize the ameliorated artificial transmission lines. Two chip capacitors of 6.7 pF and 5.1 pF are applied to realize lines with characteristic impedances of 23.5  $\Omega$  and 32.8  $\Omega$  and electrical length of  $1/4$ . The capacitances of chip capacitors are also approximately calculated, in fact, which equals the value taken away from the parasitic capacitance of meandered-line inductors from the calculated total capacitance. Chip capacitors and via holes just metalized on the edges with radius 0.3 mm replace the corresponding microstrip parallel-plate capacitors. Furthermore, the detailed parameters of ameliorated artificial transmission lines of  $Z_1$ ,  $Z_2$  with 90-degree phase shift are shown in Table 3 with the notations signed in Figure 7.

We realize transmission lines of the characteristic impedances  $Z_1 = 23.5 \Omega$  and  $Z_2 = 32.8 \Omega$  with the ameliorated artificial transmission lines and fabricate a balun with them. The ameliorated artificial transmission lines are applied to realize the transmission lines with low characteristic impedance.

#### 4. Simulation and Measurements

To verify the performance of the proposed two-section half-wave balun based on artificial transmission lines, the balun in Section 2 at 0.9 GHz was designed, simulated, and fabricated on F4B-2 substrate with thickness of 1 mm, dielectric constant of 2.65, and loss tangent of 0.001. In the balun, the transmission lines with characteristic impedances of  $Z_1 = 23.5 \Omega$  and  $Z_2 = 32.8 \Omega$  are achieved by adopting the ameliorated artificial transmission lines with chip capacitors (size code: 0603) and the  $Z_3 = 59.7 \Omega$  by conventional

TABLE 3: Dimensions of ameliorated artificial transmission lines of  $Z_1$ ,  $Z_2$  (unit: mm).

Impedance	$l_1$	$l_2$	$l_3$	$l_4$
$Z_1$	0.4	1.3	1.2	7
$Z_2$	0.3	1.8	1.9	7

artificial transmission lines and the  $Z_{\text{trans}} = 42.2 \Omega$  by the modified asymmetric artificial transmission line. The layout and photo of the fabricated balun are shown in Figure 8 with a total size of  $0.13\lambda_g \times 0.12\lambda_g$ , where  $\lambda_g$  is the guided wavelength on the substrate at 0.9 GHz. We have marked the seven sections of artificial transmission lines with different background in Figure 8(a). Figure 8(b) shows the fabricated balun, which is 28.9 mm  $\times$  26.8 mm. The proposed balun is about 11% of a balun realized by conventional microstrip lines.

Figures 9 and 10 illustrate the simulated and measured frequency responses of the proposed balun. The simulations have been completed by IE3D, while the measurements are performed with a PNA8362B vector network analyzer. The measured  $-10$  dB bandwidth of voltage reflection at its input port is from 0.82 GHz to 1 GHz, which presents a relative bandwidth of about 20%. The measured results show that the return loss at the input port at 0.9 GHz is 23 dB, and the insertion losses of the output ports 2 and 3 at 0.9 GHz are both 3.7 dB. The difference between the simulated and measured  $|S_{11}|$  is due to ignored effect of cable and connector in simulations. The measured output amplitude imbalance calculated by  $(|S_{21}| - |S_{31}|)$  and phase imbalance calculated by  $(\text{Phase}(S_{21}) - \text{Phase}(S_{31}))$  between the two output ports are

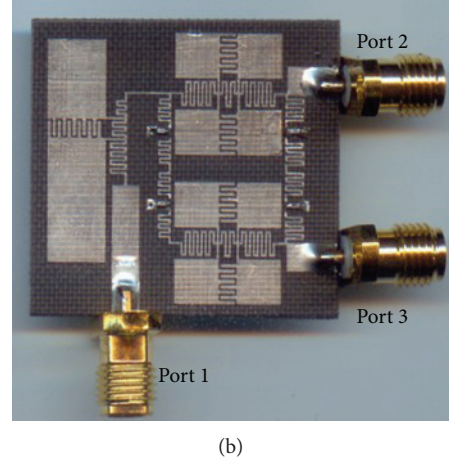
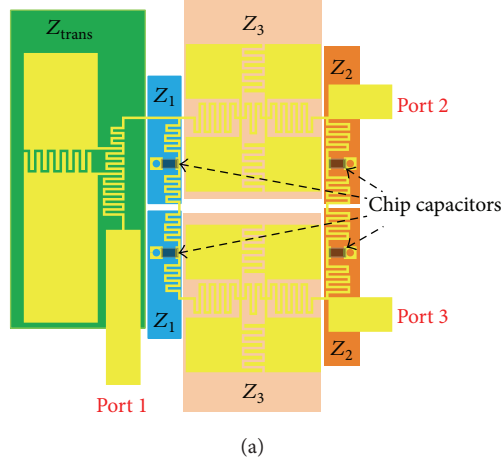


FIGURE 8: Layout and photo of the proposed two-section half-wave balun.

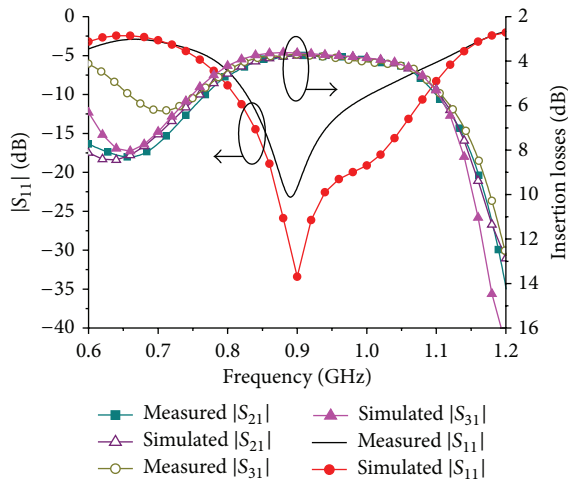


FIGURE 9: Measured and simulated return losses and insertion losses.

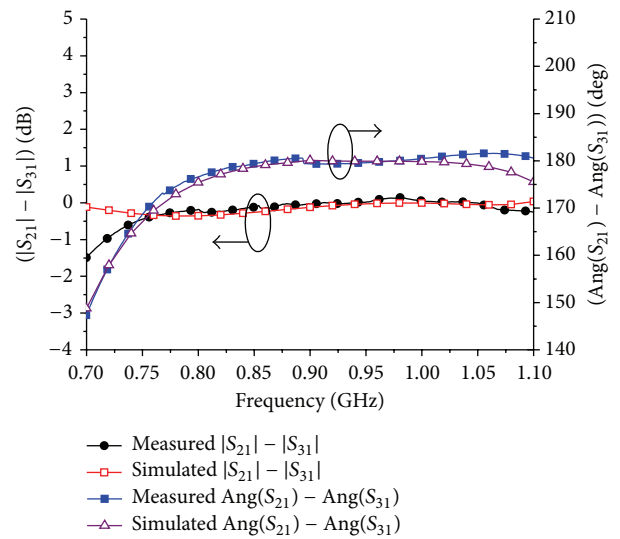


FIGURE 10: Measured and simulated phase differences and magnitude differences of output ports.

illustrated in Figure 10. In the 10 dB return loss bandwidth, the phase imbalance is within 2 degrees, and the amplitude imbalance is within 0.3 dB. Figure 10 demonstrates that the equal amplitude and 180-degree phase shift are well matched (within 0.3 dB and 2 degrees) over the frequency band of 180 MHz from 0.82 GHz to 1 GHz.

The superiority of the proposed design is clearly verified. Not only is the proposed balun compact but it also features excellent in-band amplitude and phase balance and a comparable 10 dB return loss bandwidth. The proposed design is suitable for low frequency applications, in which it demonstrates a significant size reduction. There are two limitations of the proposed balun in system applications. One is the insertion loss mainly due to its complicated structure. The total insertion loss is 0.6 dB in the proposed balun. The other is the power capacitance due to thin microstrip lines. The proposed design will find applications in low and medium power systems.

### 5. Conclusions

A novel two-section half-wave balun has been designed, fabricated, and measured in this paper, which is realized by utilizing seven sections of artificial transmission lines. The design method and procedure are presented in detail. Ameliorated asymmetric artificial transmission lines are proposed to realize transmission lines with low characteristic impedance. A balun at 900 MHz has been implemented and shows excellent frequency responses from measured results. The balun is compact at low frequency band, which is only about 10% of a conventional microstrip balun of the same configuration. The proposed balun is attractive for practical applications of microwave system in L and/or P band.

### Conflict of Interests

The authors declare that there is no conflict of interests regarding the publication of this paper.

## Acknowledgments

This work was supported in part by the 973 Program 2013CB328902, NSFC 61401054, and Technological Research Program of Chongqing Municipal Education Commission (KJ1400417).

## References

- [1] B. Sewiolo, M. Hartmann, B. Waldmann, and R. Weigel, "An ultra-wideband coupled-line balun using patterned ground shielding structures," in *Proceedings of the IEEE Radio and Wireless Symposium (RWS '08)*, pp. 459–462, January 2008.
- [2] C. Liu and W. Menzel, "Broadband via-free microstrip balun using metamaterial transmission lines," *IEEE Microwave and Wireless Components Letters*, vol. 18, no. 7, pp. 437–439, 2008.
- [3] M. A. Antoniadis and G. V. Eleftheriades, "A broadband Wilkinson balun using microstrip metamaterial lines," *IEEE Antennas and Wireless Propagation Letters*, vol. 4, no. 1, pp. 209–212, 2005.
- [4] H.-M. Lee and C.-M. Tsai, "Exact synthesis of broadband three-line baluns," *IEEE Transactions on Microwave Theory and Techniques*, vol. 57, no. 1, pp. 140–148, 2009.
- [5] V. González-Posadas, C. Martín-Pascual, J. L. Jiménez-Martín, and D. Segovia-Vargas, "Lumped-element balun for UHF UWB printed balanced antennas," *IEEE Transactions on Antennas and Propagation*, vol. 56, no. 7, pp. 2102–2107, 2008.
- [6] C.-W. Wang, T.-G. Ma, and C.-F. Yang, "A new planar artificial transmission line and its applications to a Miniaturized Butler Matrix," *IEEE Transactions on Microwave Theory and Techniques*, vol. 55, no. 12, pp. 2792–2801, 2007.
- [7] C.-W. Wang, M. Tzyh-Ghuang, and C.-F. Yang, "Miniaturized branch-line coupler with harmonic suppression for RFID applications using artificial transmission lines," in *Proceedings of the IEEE MTT-S International Microwave Symposium (IMS '07)*, pp. 29–32, Honolulu, Hawaii, USA, June 2007.
- [8] W. Huang, C. Liu, L. Yan, and K. Huang, "A miniaturized dual-band power divider with harmonic suppression for gsm applications," *Journal of Electromagnetic Waves and Applications*, vol. 24, no. 1, pp. 81–91, 2010.
- [9] R.-C. Hua, C.-W. Wang, and T.-G. Ma, "A planar quasi-Yagi antenna with a new microstrip-to-CPS balun by artificial transmission lines," in *Proceedings of the IEEE Antennas and Propagation Society International Symposium*, pp. 2305–2308, Honolulu, Hawaii, USA, June 2007.
- [10] G. I. Sajin and I. A. Mocanu, "Metamaterial CRLH antennas on silicon substrate for millimeter-wave integrated circuits," *International Journal of Antennas and Propagation*, vol. 2012, Article ID 593498, 9 pages, 2012.
- [11] K. S. Ang, Y. C. Leong, and C. H. Lee, "Analysis and design of miniaturized lumped-distributed impedance-transforming baluns," *IEEE Transactions on Microwave Theory and Techniques*, vol. 51, no. 3, pp. 1009–1017, 2003.
- [12] Y. C. Leong, K. S. Ang, and C. H. Lee, "A derivation of a class of 3-port baluns from symmetrical 4-port networks," in *Proceedings of the IEEE MSS-S International Microwave Symposium Digest*, vol. 2, pp. 1165–1168, Seattle, Wash, USA, June 2002.
- [13] R. Sturdivant, "Balun designs for wireless, mixers, amplifiers and antennas," *Applied Microwave & Wireless*, vol. 5, no. 3, pp. 34–44, 1993.